NAGOYA UNIVERSITY

Numerical investigation of momentum and scalar transport in turbulent unconfined coaxial swirling jet

by

Pravin Ananta KADU

A thesis submitted in partial fulfillment for the degree of
Doctor of Philosophy

in the
Graduate School of Engineering
Department of Mechanical Science and Engineering

December 2019

I dedicate this thesis to my father, mother and brother whose encouragement and support over many years make me enable to get such success and honor.

I also dedicate this thesis to my sweet and loving wife.

Contents

Chapter 1

Introduction

1.1 Background

Swirling flows are widely used in many engineering applications, such as industrial burners (Dinesh & Kirkpatrick (2009); Stopper *et al.* (2010)), combustion engines (Dembinski & Angstrom (2012); Wei *et al.* (2013)), and heat exchangers (Kurtbaş *et al.* (2007); Eiamsa-ard *et al.* (2014)). As far as the industrial burners are concerned, it is desired to have the reduced length of combustion flame as well as to increase the efficiency by reusing the unburned products of combustion and the high heat energy existing in the burned products of combustion. The jets with swirling motion fulfill these characteristics by enhancing the mixing between fuel and oxidant jets, and recirculating the burned/unburned products of combustion in order to ignite the incoming mixture, which make the swirling jets an essential constituent of burners and thus gain the attention of many researchers.

The burners can be of two different configurations: (a) the single swirling jet, and (b) coaxial jet with swirl imparted to one of two jets. The former configuration is mainly associated with the premixed combustion in which the fuel and oxidant are mixed prior to their injection in combustion chamber, and later configuration is associated with the non-premixed combustion in which the fuel and oxidant are injected directly in combustion chamber through separate jets, i.e., without being premixed. To illustrate these configurations, the examples of industrial burners are shown in Figure 1.1. In Siemens G30 DLE Burner, the fuel and air are premixed, and the mixture is injected into the combustion chamber through the swirlers. On the other hand, the Sydney Swirl Burner consists of

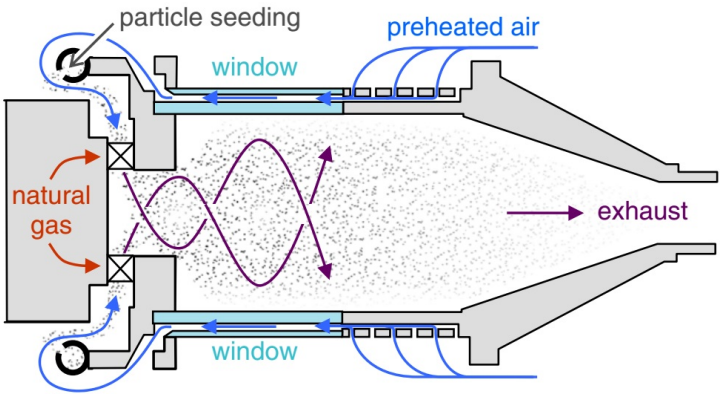

(a)

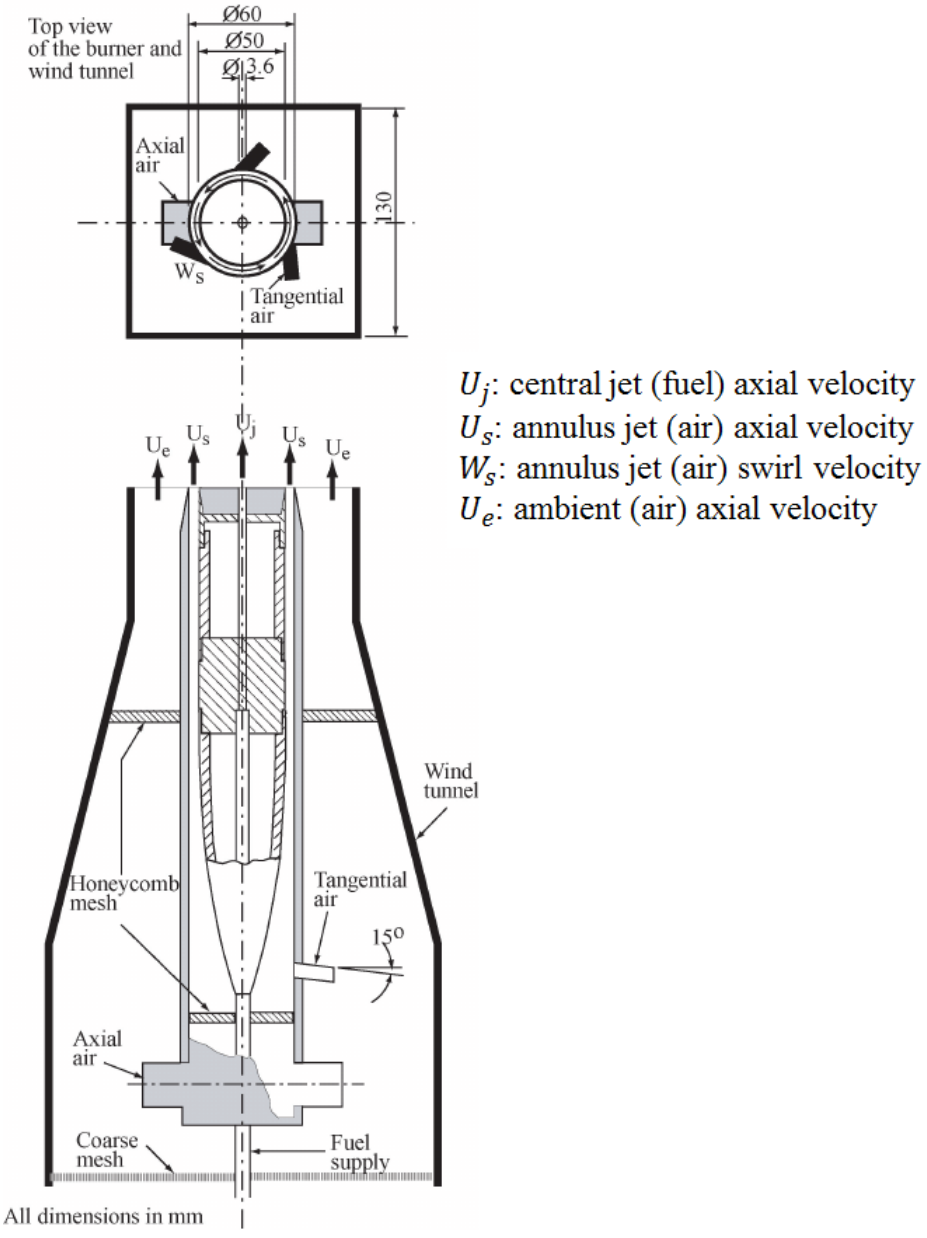

(b)

FIGURE 1.1: Schematic of different burners. (a) Siemens G30 DLE Burner. Adapted from Stopper *et al.* (2010). (b) Sydney Swirl Burner. Adapted from Dinesh & Kirkpatrick (2009).

coaxial jet with the swirl in the outer air jet (a secondary ambient air jet is also injected).

The single swirling jet has been studied by numerous researchers: Harvey (1962); Cassidy & Falvey (1970); Narain (1977); Leschziner & Rodi (1984); Komori & Ueda (1985); Mehta *et al.* (1991); Billant *et al.* (1998); Gallaire *et al.* (2004); Lu *et al.* (2005); Örlü & Alfredsson (2008); Shiri (2010); Stopper *et al.* (2010); Oberleithner *et al.* (2011); Markovich *et al.* (2014); Wan *et al.* (2015); Sieber *et al.* (2017); Clees *et al.* (2018); Moise & Mathew (2019); to name a few. Although the coaxial swirling jet has gained the attention of some researchers: Ribeiro & Whitelaw (1980); Roback & Johnson (1983); Ben-Yeoshua (1993); Champagne & Kromat (2000); Huang & Tsai (2001); Dinesh & Kirkpatrick (2009); Santhosh *et al.* (2014); Rajamanickam & Basu (2018), it has been not studied extensively and hence focused in this thesis.

1.1.1 Swirling jet

To achieve the optimal mixing characteristics for coaxial jet, one must focus on reducing the spans of the potential cores of jets and increasing jet growth. This can be achieved by changing the velocity ratio between two jets for a given set of jet diameters (Champagne & Wygnanski (1971); Rehab *et al.* (1997); Buresti *et al.* (1998); Abboud & Smith (2014); Li *et al.* (2017)). However, it has been observed that potential cores are still extended over a considerable downstream length, even when the outer jet (OJ) velocity exceeds the inner jet (IJ) velocity by a factor of two. The introduction of swirl into one of the jets can help to overcome this drawback, as demonstrated by Ribeiro & Whitelaw (1980); Ben-Yeoshua (1993); Champagne & Kromat (2000). They illustrated that in the presence of the swirl, a radial static pressure gradient is set up as it is proportional to the mean squared azimuthal velocity divided by the radial distance ($\partial\overline{p}/\partial r \propto \overline{V_\theta}^2/r$ yielded from the approximation of equation for mean radial momentum. Here $\overline{p}$ and $\overline{V_\theta}$ are the mean static pressure and mean azimuthal velocity, respectively). This results in the pressure deficit at the centerline. The fact of decay in azimuthal velocity in the downstream region creates an adverse (positive) pressure gradient in the axial direction. The outcome of this process is the decay of centerline streamwise velocity and the increased rate of spread of the jet.

Furthermore, if the swirling strength exceeds a certain threshold value, the recirculation, a property of the vortex breakdown (VB), appears at the central

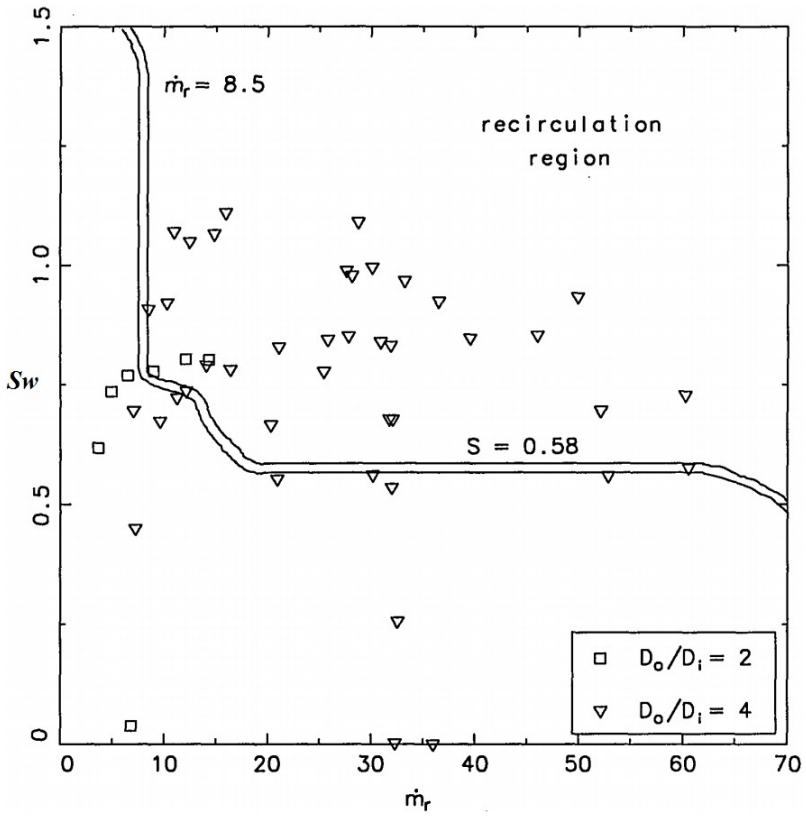

FIGURE 1.2: State of the flow. Adapted from Ben-Yeoshua (1993). The swirl number $Sw = (\int_0^{R_o} \overline{U}\,\overline{V_\theta}\,r^2\,dr)/(R_o \int_0^{R_o}(\overline{U}^2 - \overline{V_\theta}^2/2)\,r\,dr)$. Here, R_o and D_o are outer radius and diameter of OJ, respectively, D_i is the diameter of IJ and $\overline{U}$ is the mean streamwise velocity. The mass flow rate ratio $\dot{m}_r = \dot{m}_{OJ}/\dot{m}_{IJ}$. The dividing strip in the plot separates the areas of absence and presence of recirculation or VB.

region (Ben-Yeoshua (1993); Champagne & Kromat (2000)). The swirl number Sw (the ratio of the axial flux of momentum in the azimuthal direction to that in the axial direction) and $\dot{m}_r$ (the ratio of the mass flow rate through OJ to that through the IJ) dictate the occurrence of recirculation. Ben-Yeoshua (1993) performed numerous experiments to demonstrate this (see Figure 1.2). It was observed that the recirculation occurs when $Sw > 0.78$ for around $\dot{m}_r \approx 8.5$, and then Sw limit decreases to 0.58 for $\dot{m}_r > 18.0$.

1.1.2 Vortex breakdown

The distinct types of VB reported for the configuration of coaxial swirling jet (Dinesh & Kirkpatrick (2009); Santhosh *et al.* (2013, 2014)) are namely, (a) bubble, and (b) conical. These two types of VB have also been reported for the configuration of a single swirling jet (Billant *et al.* (1998)). As the name

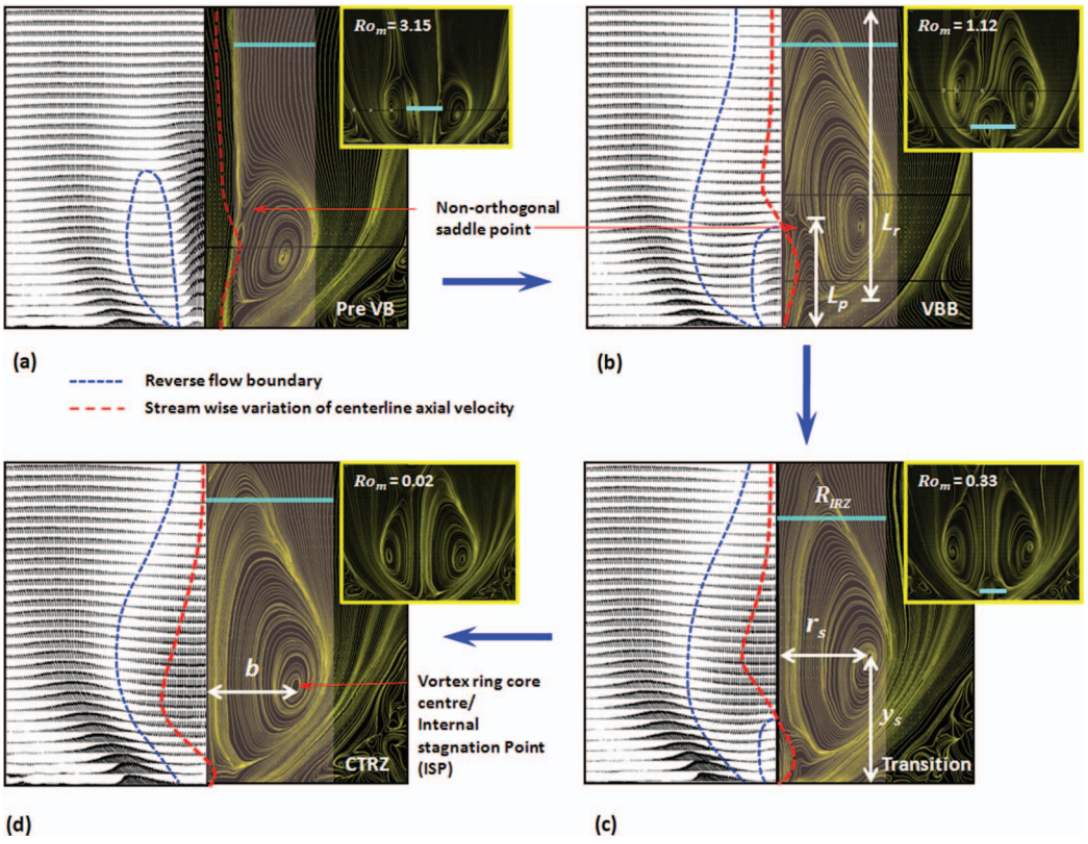

FIGURE 1.3: Effect of modified Rossby number on coaxial swirling jet investigated by Santhosh *et al.* (2013). (a) Pre-VB state. (b) VBB. (c) Transition state. (d) CTRZ.

suggests, the bubble type of VB or simply the vortex breakdown bubble (VBB) is characterized by axisymmetric bubble-shaped structure, whereas the conical type is of axisymmetric conical-shaped structure with the recirculation at the central region. Santhosh *et al.* (2013) demonstrated the transformation from pre-VB to various structures (see Figure 1.3). They used a modified Rossby number along with the swirl number for this study. Here, modified Rossby number is taken as $Ro_m = |\Delta U| / V_{\theta,avg}$, where numerator is the velocity deficit between two coaxial jet (i.e., $|\Delta U| = |U_{IJ} - U_{OJ}|$, where U_{IJ} and U_{OJ} are the bulk velocities of IJ and OJ, respectively) and denominator is the mass flow averaged azimuthal velocity at the nozzle exit (i.e., $V_{\theta,avg} = \int 2\pi r \overline{V_\theta} dr / A$, where A is the cross-sectional area of nozzle). The swirl number is taken as $S = (\int_0^{R_o} \rho \overline{U}\, \overline{V_\theta}\, r^2\, dr) / (R_o \int_0^{R_o} \rho \overline{U}^2\, r\, dr)$, where $\overline{U}$ is the mean streamwise velocity. They varied the Ro_m substantially $(3.15 - 0.02)$ with a slight change in S $(0.592 - 0.801)$. It was observed that for $Ro_m \gg 1$, two vortex rings are appeared in the annular region between two jets and is called as the pre-VB state. By decreasing Ro_m to ≈ 1, the structures evolve into the VBB partially penetrated by IJ. With further decrement in Ro_m, the penetrated part slackens, and the structure is called as the central toroidal

recirculation zone (CTRZ) or simply a toroidal recirculation bubble. In their other study (Santhosh *et al.* (2014)), it was observed that by keeping approximately same Ro_m (i.e., $Ro_m \approx 1$ for partially penetrated VBB and $Ro_m \to 0$ for CTRZ) and by increasing S, the corresponding structures evolved into the conical breakdown. However, further substantial increment in S transformed the conical breakdown back to the VBB.

1.2 Motivation

Although some efforts have been made by researchers in the past to study the influence of swirl on the coaxial jet, some issues are yet to be addressed:

- Mehta *et al.* (1991) demonstrated this experimentally for the single swirling jet configuration. It was shown that the introduction of swirl elevates all the six independent components of Reynolds stresses. The increase in the radial spread of the Reynolds stresses was also observed indicating the growth of the mixing layer. Similar observations were also made by Ribeiro & Whitelaw (1980) for the configuration of coaxial swirling jet. This feature of increase in the Reynolds stresses along with their spread is vital for the mixing enhancement. However, the reasons for this change in Reynolds stresses, and hence the turbulent kinetic energy (TKE) in coaxial swirling jet have not been thoroughly explored yet.

- Passive scalars have been widely used to demonstrate mixing in various jet flows in the past. The mean and root-mean-squared (RMS) fluctuations and turbulent fluxes of passive scalars all provide information about mixing. Roback & Johnson (1983) attempted to analyze the effects of swirl on these statistics by introducing passive scalars through IJ only and found that the spreading rate of scalars increases with an increase in swirling strength. Dinesh *et al.* (2010) made similar observations based on the mean and RMS fluctuation distributions of IJ scalars. However, in the past studies, the injection of passive scalars through only one of the two jets of coaxial swirling jet limited the investigations aiming the mixing features in swirling jets, especially due to the VBB. The simultaneous injection of passive scalars through both the jets of coaxial jet would provide more insight into mixing characteristics.

- Over the years, various techniques of modal decomposition have been developed to better understand the physically important structures or modes in the swirling jets. Some studies (Oberleithner *et al.* (2011); Markovich *et al.* (2014); Wan *et al.* (2015); Sieber *et al.* (2017); Clees *et al.* (2018)) have focused on the visualization of coherent structures using these techniques for the configuration of single swirling jet only, but that for the coaxial swirling jet is scarcely investigated (Rajamanickam & Basu (2018)).

This thesis focuses on the above topics and attempts to enhance the knowledge in the field of coaxial swirling jet.

1.3 Outline of thesis

In order to acquire an in-depth knowledge of the effects of swirl, computational fluid dynamics tool is used for this work. The outline of this thesis is as follows:

- In Chapter 2, the numerical details are explained. It includes the generation of an adequate inflow boundary condition as the swirling jet results in the non-standard profiles at the nozzle exit.
- In Chapter 3, the flow development is illustrated along with the code validation. The change in Reynolds stresses and the TKE due to the swirl is focused in this chapter.
- Chapter 4 concentrates on the investigation of mixing characteristics by injecting passive scalars through both the jets.
- In Chapter 5, modal decomposition is carried out to investigate the coherent structures present in the flow for a case of strong swirl.
- Chapter 6 summarizes the conclusions of this study.

The parts of this thesis (Chapters 2, 3, and 4) are based on the works of Kadu *et al.* (2019*a*,*b*).

Chapter 2

Numerical method and flow conditions

In this chapter, the numerical methodology and flow conditions used for the investigation are explained. The §2.1 presents the governing equations along with their solution methodology. The method to obtain the inlet boundary condition, which is a critical part of simulation of swirling flows, is detailed in §2.2. It is followed by remaining boundary conditions in §2.3. The simulation details are then presented in §2.4.

2.1 Governing equations and numerical methodology

The direct numerical simulations (DNS) is employed to compute the transient flow fields by solving the 3D Navier-Stokes and continuity equations with the assumption of an incompressible Newtonian flow. The dimensionless equations, which are formed using IJ bulk velocity U_{IJ} and IJ diameter D, are defined as follows:

$$\frac{\partial u_i}{\partial x_i} = 0, \tag{2.1a}$$

$$\frac{\partial u_i}{\partial t} + u_j \frac{\partial u_i}{\partial x_j} = -\frac{\partial p}{\partial x_i} + \frac{1}{Re_D} \frac{\partial^2 u_i}{\partial x_j \partial x_j}, \tag{2.1b}$$

where the IJ Reynolds number Re_D is defined as $Re_D = U_{IJ}D/\nu$ and ν is the kinematic viscosity.

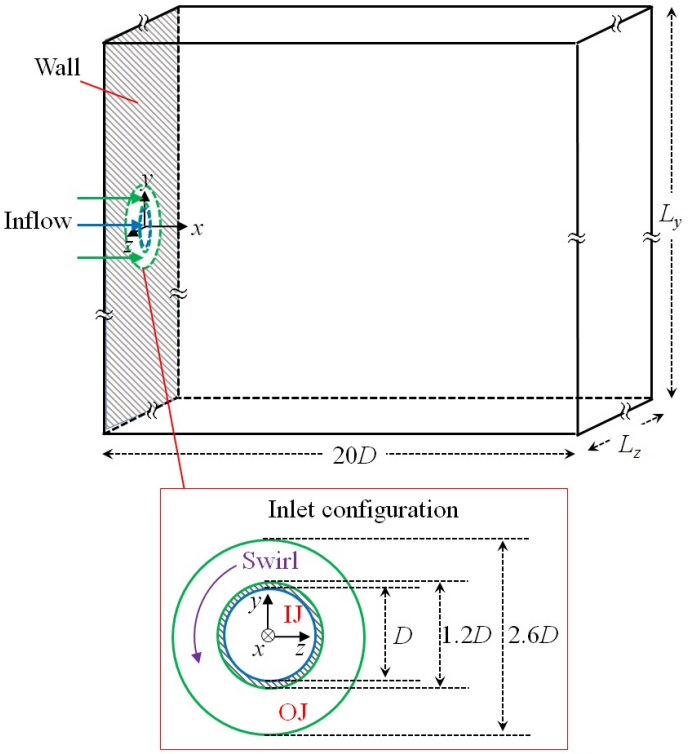

FIGURE 2.1: Schematic of the computational domain and inlet configuration. An annular wall with a thickness of $0.1D$ is present between the IJ and OJ. The cross-stream domain size ($L_y \times L_z$) is larger in the swirling cases compared to the non-swirling case, as mentioned in §2.4.

A schematic of the computational domain and the inlet configuration is presented in Figure 2.1. Note that the inlet configuration is taken as per the experimental setup available in the laboratory, and the numerical results are verified with the experimental results in §3.2. The coordinate system is centered on the center of the inlet plane and the x axis coincides with the jet axis. The governing equations are solved using the fractional-step method (Kim & Moin (1985)). The pressure Poisson equation is solved using the conjugate gradient method (Nocedal & Wright (2006)). Time integration is performed using a second-order Runge-Kutta method. A conventional staggered grid system is implemented using equally-spaced, structured-Cartesian grid points. The conservative scheme (Morinishi *et al.* (1998)) and central difference scheme are employed for spatial discretization of the convection and viscous terms, respectively. The discretization provides fourth-order accuracy in the x direction and second-order accuracy in the y and z directions. The coordinate transformation is performed to present the results in a cylindrical coordinate system.

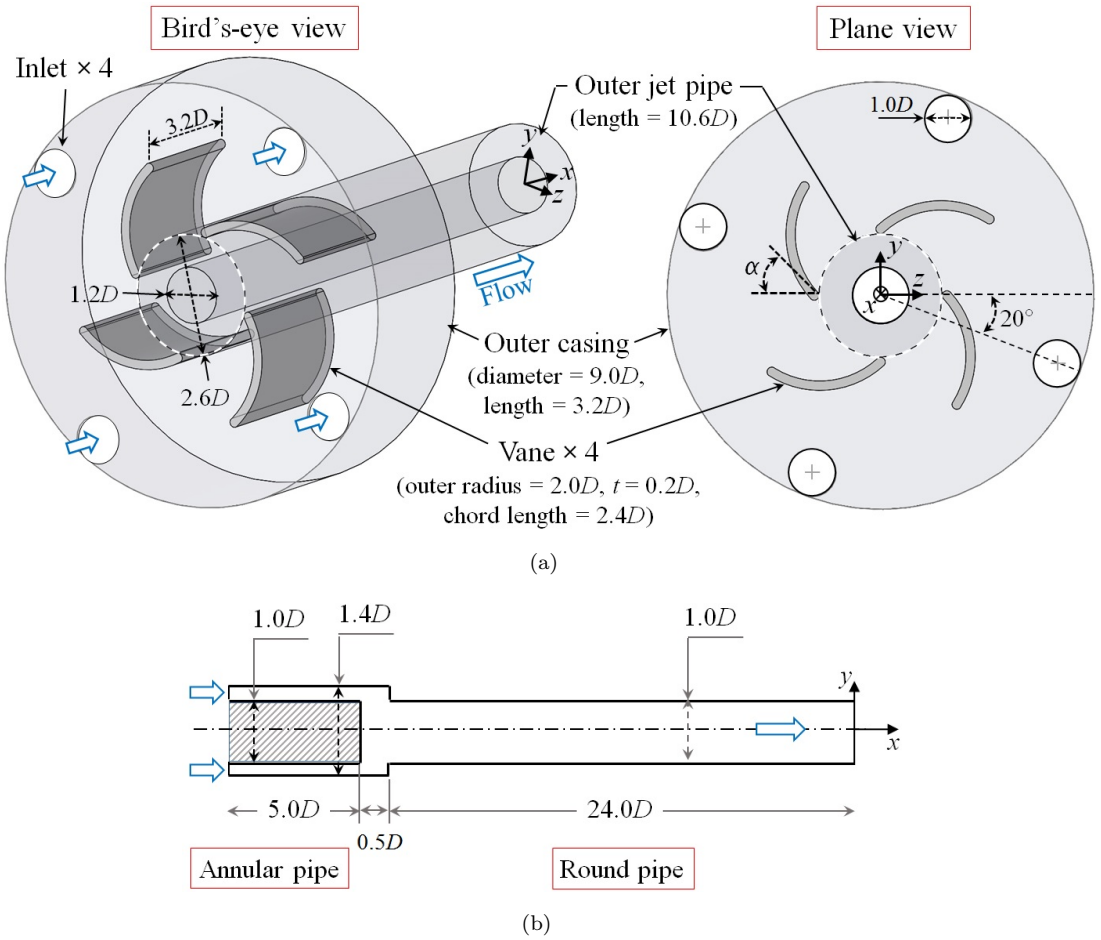

FIGURE 2.2: Nozzle configuration. Dimensions are mentioned in terms of IJ diameter D. (a) OJ nozzle: bird's eye view and plane view. Vanes are removed for the non-swirling case. Swirling cases with vane angles, $\alpha = 90°$ and $80°$ are considered. (b) IJ nozzle (representative geometry): cross-sectional view.

2.2 Inlet boundary condition

The method of swirl generation influences the profiles of the mean velocity components, which affects vortex behavior (Xia *et al.* (1997); Lucca-Negro & O'doherty (2001)). To obtain the desired mean inflow conditions and statistically correct turbulent fluctuations, precursor simulations (Tabor & Baba-Ahmadi (2010)) were performed for the jet nozzles prior to the main simulations. The strategy includes the mapping of instantaneous velocity components at the nozzle exit onto the main simulation inlet.

SolidWorks 2017 software is used to create the geometries. Figure 2.2 presents the nozzle configuration for OJ and IJ. The inner and outer diameters of the OJ pipe are $1.2D$ and $2.6D$, respectively. The swirl in the OJ is generated using four vanes mounted over the OJ pipe with a span of 90°. The swirling

strength is controlled by the vane angle α. Two cases with different vane angles $\alpha = 80°$ and $90°$, and a case with the absence of vanes are considered. The case of $\alpha = 90°$ is considered to obtain the highest possible swirling strength for the present configuration, whereas the case of $\alpha = 80°$ is taken to obtain the intermediate swirling strength. The vanes are enclosed by a casing with four inlets. Note that the configuration of OJ nozzle is same as that in the experimental setup. The mesh is generated using the Pointwise Version 18.0 R4 software. The cell count of OJ nozzle is around 4.39 million and the cells are of prism type. For the IJ, an annular pipe of length $5.5D$ is positioned upstream of the $24.0D$ long inner round pipe to generate turbulence. The cell count of IJ nozzle is 3.13 million and the cells are also of prism type. The Reynolds number for the IJ, Re_D, is 2200. Re_D is limited to such a low magnitude based on the requirement of the grid resolution required for DNS and the available computational resources. The ratio of the total flow rate through OJ to that through the IJ, Q_{OJ}/Q_{IJ}, is 10.64, and the resulting bulk velocity ratio, U_{OJ}/U_{IJ}, is 2.00. Note that Q_{OJ}/Q_{IJ} $(= \dot{m}_r)$ is chosen as equal to 10.64 because it is well beyond the limit where the recirculation can occur (see Figure 1.2). These precursor simulations for the nozzles were performed using the open-source software OpenFOAM Version 2.4.0. Large eddy simulation (LES) with the dynamic Smagorinsky model is used here due to the limitation of the computational resources. The second-order implicit scheme is used for the time derivative and Gauss linear scheme (second-order Gaussian finite volume integration) is used for the spatial discretization (Greenshields (2015)). The solver used is the *pimpleFoam* which is based on the PIMPLE (merged PISO-SIMPLE: pressure implicit with splitting of operator and semi-implicit method for pressure-linked equations) algorithm.

Figure 2.3(a) presents the radial profiles of the mean streamwise velocity $(\overline{U})$ and mean azimuthal velocity $(\overline{V_\theta})$ at the nozzle exits for the three cases considered in this study. The streamwise velocity of IJ has a peak at approximately 1.5 times the IJ bulk velocity. The distribution of the OJ streamwise velocity is slightly modified by the presence of vanes. Naturally, the azimuthal velocity is observed to be affected by vanes and its peak in the case with $\alpha = 90°$ is more than twice that in the case with $\alpha = 80°$. The swirl number Sw is used to quantify swirling strength (Rajaratnam (1976); Ribeiro & Whitelaw (1980); Ben-Yeoshua

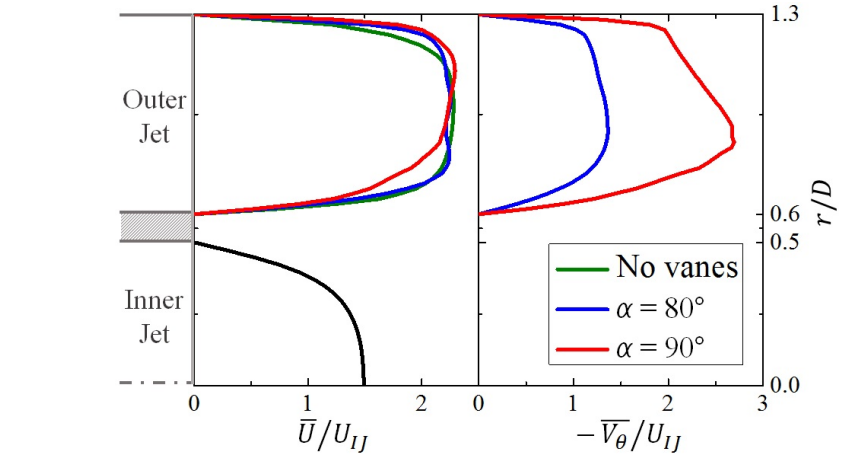

(a)

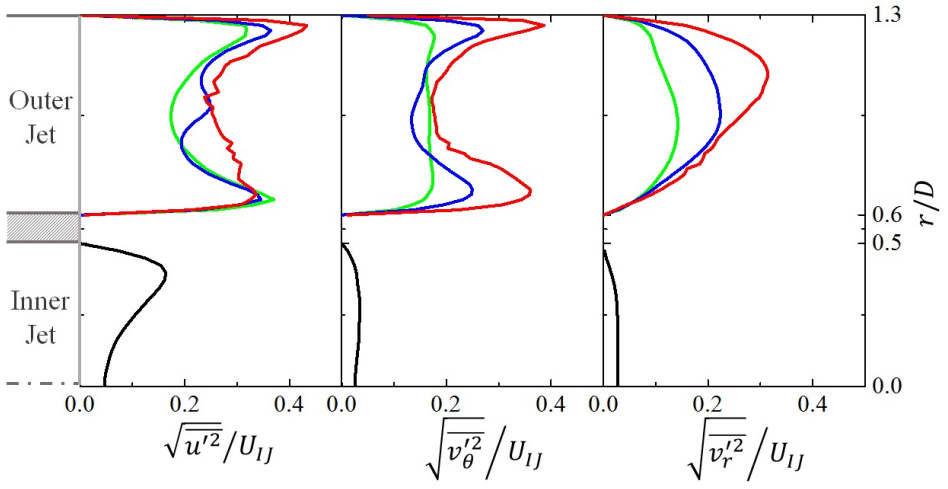

(b)

FIGURE 2.3: Results at the nozzle exit ($x = 0.0D$). (a) Radial distribution of the mean velocity components. (b) Radial distribution of the turbulence intensities.

(1993)) and is calculated as

$$Sw = \frac{\int_0^{R_o} \overline{U}\,\overline{V_\theta}\,r^2\,dr}{R_o \int_0^{R_o} (\overline{U}^2 - \overline{V_\theta}^2/2)\,r\,dr}. \tag{2.2}$$

Here, R_o is the outer radius of the OJ. The numerator in the formula above is the streamwise flux of the azimuthal momentum and the denominator is the streamwise flux of the streamwise momentum. Note that the term $-\overline{V_\theta}^2/2$ in the denominator represents an approximation of the static pressure obtained from the radial component of the momentum equation (refer to Rajaratnam (1976) for this formulation). The value of the swirl number for the case with $\alpha = 80°$ is 0.5 and

that for the case with $\alpha = 90°$ is 1.8. Note that the case with $Sw = 0.5$ lies in the region of no recirculation of Figure 1.2 (the criterion of Ben-Yeoshua (1993)), whereas the case with $Sw = 1.8$ lies in the region of occurrence of recirculation. The case with no vanes yields a value of $Sw = 0$ based on negligible azimuthal momentum. The nozzle exit streamwise ($\sqrt{\overline{u'^2}}/U_{IJ}$), azimuthal ($\sqrt{\overline{v_\theta'^2}}/U_{IJ}$), and radial ($\sqrt{\overline{v_r'^2}}/U_{IJ}$) turbulence intensities are reported in Figure 2.3(b). Here, u', v_θ' and v_r' are the streamwise, azimuthal and radial velocity fluctuations, respectively. The IJ exhibits the typical distribution of velocity fluctuations as seen for the internal flow. The turbulence level in the OJ is observed to be higher as compared to IJ which may have occurred because of the insufficient length of OJ nozzle pipe to dampen the turbulence fluctuations. Also, note that the turbulence intensities presented here are based on U_{IJ} and would be $\leq 20\%$ if calculated based on U_{OJ}. Furthermore, the fluctuations are increased considerably with the increase in swirl number.

The precursor and main simulations can be linked through the libraries of instantaneous velocity components at the jet exits by maintaining consistent time steps for both simulations. Considering memory limitations and computational costs, these libraries consist of instantaneous data for only $40,000$ time steps and are used repeatedly. However, the total time represented by the libraries is sufficiently large and is equal to $162.0D/U_{IJ}$ for the non-swirling case and $76.8D/U_{IJ}$ for the swirling cases. These instantaneous velocity components are mapped onto the staggered grid for DNS using mixed linear weighted / cell-face interpolation (*cellPointFace* interpolation scheme of OpenFOAM) because the grids are of different types. Note that based on the use of fourth-order accurate discretization in the x-direction and fully conserved schemes, the libraries contain data for three x-directional cross-sections separated by the spatial grid size Δ_X of DNS.

2.3 Outflow, cross-stream, and wall boundary conditions

The convective outflow boundary condition (Dai *et al.* (1994)) is used for the outlet plane as follows:

$$\frac{\partial \Theta}{\partial t} + U_c \frac{\partial \Theta}{\partial x} = \frac{1}{Re_D} \frac{\partial^2 \Theta}{\partial x_j \partial x_j}, \tag{2.3}$$

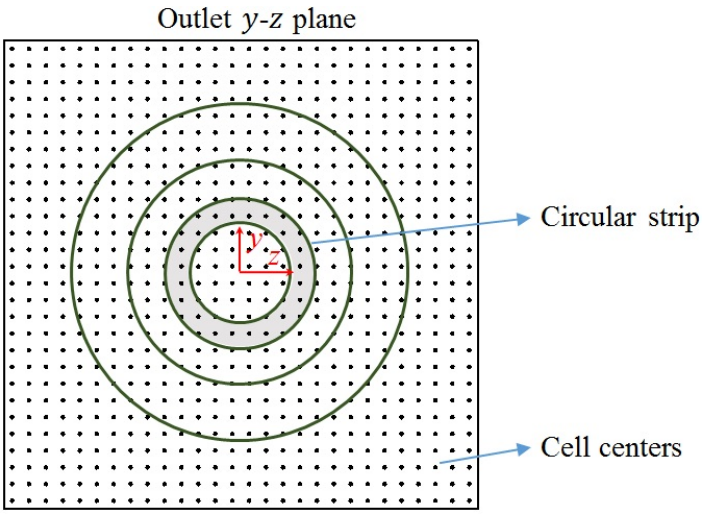

FIGURE 2.4: Representative diagram for the outflow boundary condition.

where Θ refers to the velocity components. The convective velocity U_c is computed over the circular strips (see Figure 2.4) at each time-step to account for the radial variation in the streamwise velocity as

$$U_c = \frac{\sum(u_p \cdot A_p)}{\sum A_p}. \tag{2.4}$$

Here, u_p is the instantaneous streamwise velocity of the cell p and A_p is the corresponding area of that cell. The numerator in this formulation computes the flow rate through the circular strip and the denominator is the area of strip. Here, $\sum$ is the summation over the strip. The innermost strip is nothing but a circle with radius equal to $0.2D$ and the radii of the subsequent annular (circular) strips are incremented by 10% relative to the radius of the preceding strip.

The lateral and spanwise boundaries are treated with the Neumann boundary condition $\partial\Theta/\partial n = 0$. This allows fluid to come in or out in the normal direction of computational domain. A no-slip boundary condition $u_i(x_{boundary}, t) = 0$ is employed for the wall between the two nozzle outlets and the wall surrounding the outer nozzle.

2.4 Simulation details

The cases are labeled as Sw0, Sw05, and Sw18 for cases with swirl numbers of 0, 0.5, and 1.8, respectively. The DNS domain size $L_x \times L_y \times L_z$ is $20D \times 20D \times 20D$ for case Sw0 and $20D \times 28D \times 28D$ for cases Sw05 and Sw18.

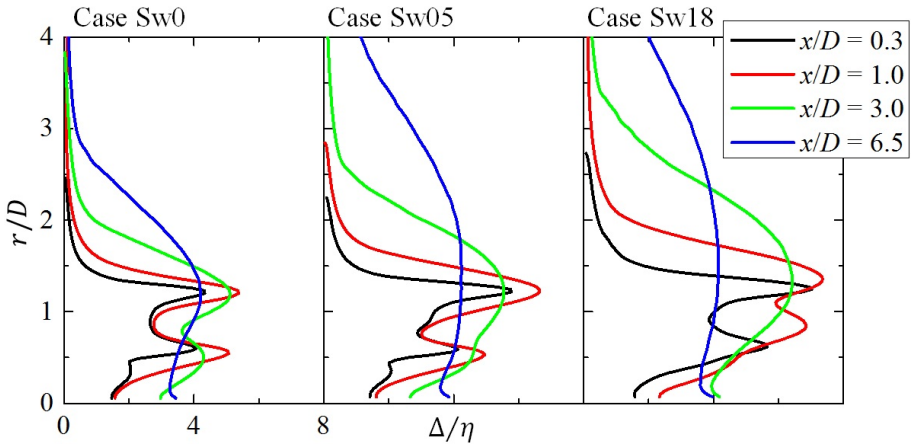

FIGURE 2.5: Radial distribution of Δ/η at various cross-sections for all three cases.

The larger cross-stream domain $L_y \times L_z$ for the swirling cases is adopted based on the greater expected spread of the jets. The grid points $N_x \times N_y \times N_z$, which are uniformly distributed, are of size $700 \times 700 \times 700$ for case Sw0 and $700 \times 980 \times 980$ for cases Sw05 and Sw18. The resolution of the grid $\Delta = (\Delta_X \Delta_Y \Delta_Z)^{1/3}$ is of the order of the Kolmogorov length scale η. The maximum Δ/η (see Figure 2.5) is located at the cross-section $x = 1.0D$ in all three cases and is equal to 5.1, 6.6, and 7.1 for cases Sw0, Sw05, and Sw18, respectively. Here, $\eta = (\nu^3/\epsilon)^{1/4}$ and ϵ is the kinetic energy dissipation rate per unit mass. The fluid in the domain is initially in the stationary state. The time-steps for cases Sw0, Sw05, and Sw18 are $0.00405D/U_{IJ}$, $0.00192D/U_{IJ}$, and $0.00192D/U_{IJ}$, respectively, and the corresponding Courant number is around 0.3. The Fortran programming language was used to develop the code and the message passing interface (MPI) library was used for code parallelization. Implementation of MPI is done using the two-dimensional domain decomposition in the $y - z$ plane.

Chapter 3

Momentum transport

3.1 Introduction

As demonstrated by Mehta *et al.* (1991) for a single swirling jet and by Ribeiro & Whitelaw (1980) for the coaxial swirling jet, the swirling flows are responsible for the intensification of the Reynolds stresses and TKE. This consequence of the swirl is an important point for the mixing enhancement. However, the reason of intensification of Reynolds stresses in coaxial jet due to the swirl has not been explored in detail. In this chapter, this is achieved by investigating the budgets of TKE and Reynolds normal stresses. Moreover, the analysis of budgets of TKE and Reynolds normal stresses for the coaxial swirling jet is rarely reported in the previous studies, and hence this study can form the basis for the turbulence modeling work.

The statistical data (i.e., Reynolds time-averaged data) are evaluated from the instantaneous data of 1296, 652, and 1056 time scales D/U_{IJ} for the cases Sw0, Sw05, and Sw18 respectively, which are observed to be enough to get statistically steady results for the mean velocity components and Reynolds stresses. Note that the cases Sw0 and Sw18 are simulated for longer time as the budget analysis is performed for those cases which contains third-order statistics.

In §3.2, the numerical results are verified with the experimental results. After a brief explanation about the instantaneous flow features in §3.3, the mean flow development is depicted in §3.4. The development of the Reynolds stresses and TKE is presented in §3.5, and the budgets of TKE and Reynolds normal

stresses are then presented for the cases Sw0 and Sw18 in §3.6. The conclusion is summarized in §3.7.

3.2 Code validation

Basic statistics of the flow fields obtained through simulations are verified based on experimental measurements in this section.

3.2.1 Experimental details

Experiments are performed by Mr. Masatoshi Sugino in the laboratory for the cases Sw0 and Sw18 with the identical nozzle configuration and the flow parameters. The measurements of flow field are carried out by particle image velocimetry (PIV) and the fluid used for the experiment is water. The streamwise and radial components of velocity field are measured in the $x-y$ plane and azimuthal component in the $y-z$ plane. An Nd: Yag laser (DANTEC RayPower 5000) sheet of wavelength 532 nm and thickness 1 mm is used for the illumination of the test section. The seeded particles dispersed in both the jets have the mean diameter 11 μm and 50 μm while carrying out measurements in $x-y$ and $y-z$ planes respectively. Note that the seeded particles are larger in $y-z$ plane as compared to that in $x-y$ plane because the distance of visualizing camera from the test section is comparatively longer in the case of $y-z$ plane and larger seeded particles are required for them to be recognized by camera. The flow is visualized by a high-speed video camera (Ametek Phantom V210) of 1280×800 pixel resolution. The band-pass filter (Asahi spectrometer PB0040) is affixed to the camera. The images are captured for 12 s in $x-y$ plane with the sampling frequency of 2000 Hz. In the $y-z$ plane, the sampling frequency spans around 1000 Hz to 600 Hz for the different locations and the images are captured for the same time. The spatial resolution to estimate the velocity field is 0.91 mm for the $x-y$ plane measurements, while that for the $y-z$ plane measurements ranges between 1.03 and 0.98 mm at different cross-sections. The captured images are converted into 8-bit digital codes. Both the camera and laser are mounted on the traversing beams with a jack to allow movement for the camera in the direction perpendicular to image capturing plane. The analysis of the flow field is carried out by a commercial software, DANTEC DynamicStudio.

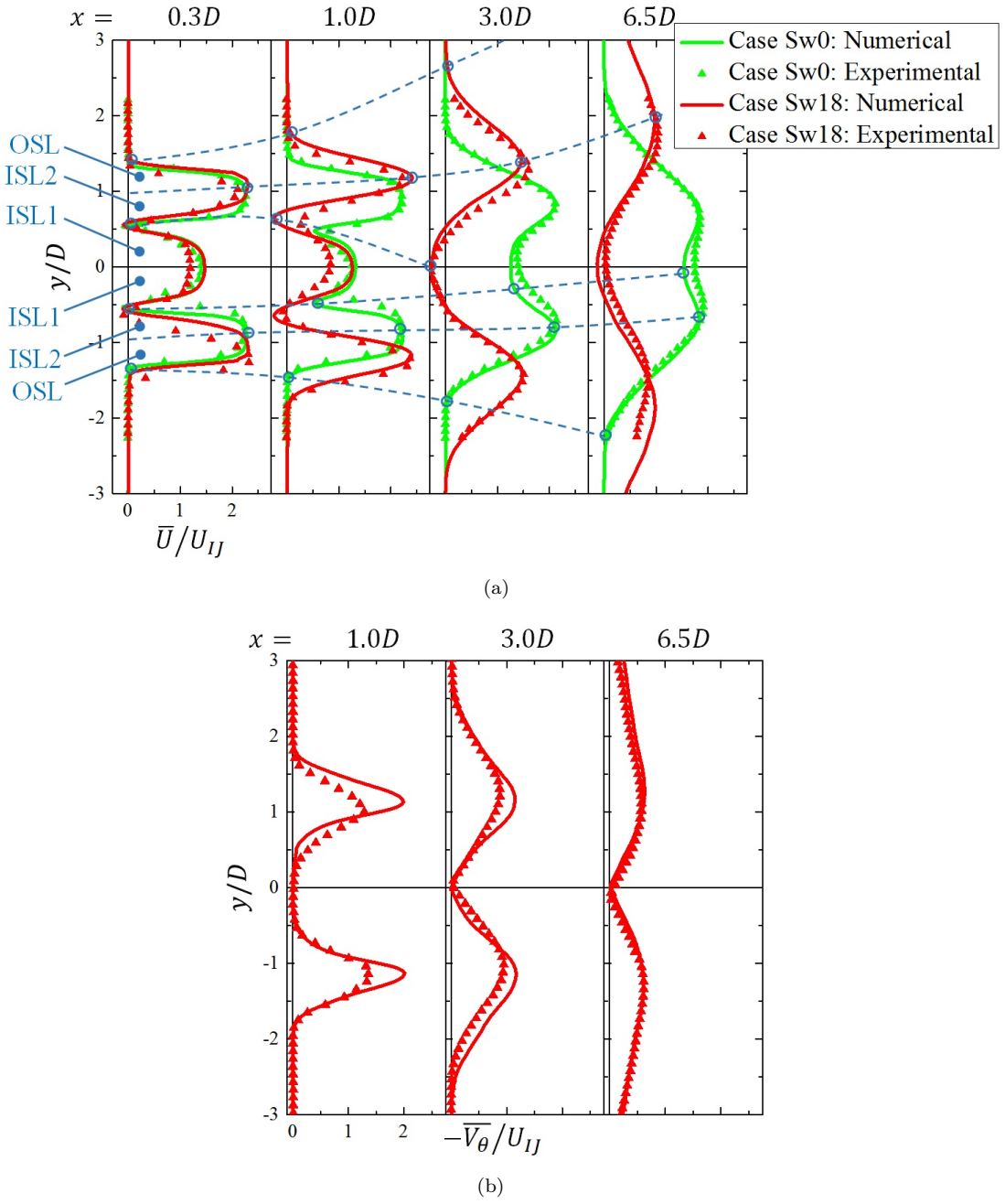

FIGURE 3.1: Comparison between numerical study and experiment: radial distribution of the mean velocity components. (a) Mean streamwise velocity. Dashed lines in region $y/D < 0$ enclose shear layers for case Sw0 and that in region $y/D > 0$ enclose shear layers for case Sw18. (b) Mean azimuthal velocity.

3.2.2 Comparison of results

Figure 3.1 compares the radial distribution of mean velocity components at various streamwise locations. The azimuthal velocity measurements are only carried out for the case Sw18. The computed mean streamwise velocity distribution for the case Sw0 depicted in Figure 3.1(a) shows very good agreement with

the measurements. The two shear layers, inner one (denoted as ISL) between the two jets and outer one (denoted as OSL) in between the peak in OJ region and surrounding ambient, are estimated correctly along with the peaks at jet cores. Inner shear layer (or can also be termed as inner mixing layer) is sub-divided for future reference into ISL1- between the axis and local minimum position of mean streamwise velocity separating two jets and, ISL2- between local minimum position and peak in the OJ region. Now we focus on the case Sw18. The measured mean streamwise velocity profile for OJ is inclined outwards at the upstream-most location $x/D = 0.3$. This outward inclination is also appeared for the simulation results at the nozzle exit (Figure 2.3(a)) and is carried forward to the downstream. The IJ mean streamwise velocity decays faster at around $x/D = 1.0$ for the experiment than that for simulation, but the agreement is better in OJ region. The recirculation is observed at $x/D = 3.0$ for both simulation and experiment, which also shows the improved agreement in the IJ region. In Figure 3.1(b), the peaks of upstream mean azimuthal velocity for the case Sw18 shows a discrepancy between the simulation and experiment, although the radial positions of peaks are same and profiles in the shear layers resemble each other. This disagreement can be attributed to the deviation of the simulation inlet condition from the experimental inflow. The distribution at downstream locations demonstrates the better agreement.

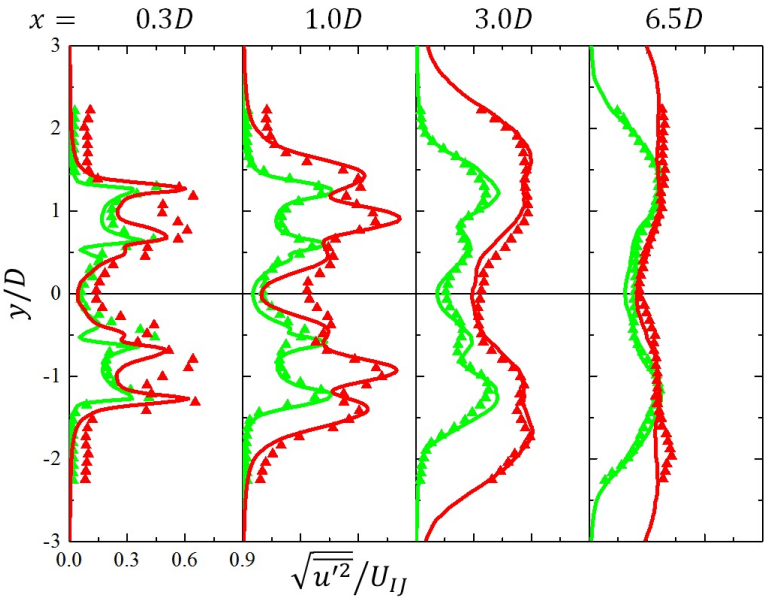
x = 0.3D 1.0D 3.0D 6.5D
y/D
3
2
1
0
-1
-2
-3
0.0 0.3 0.6 0.9
√u'2/U_IJ

(a)

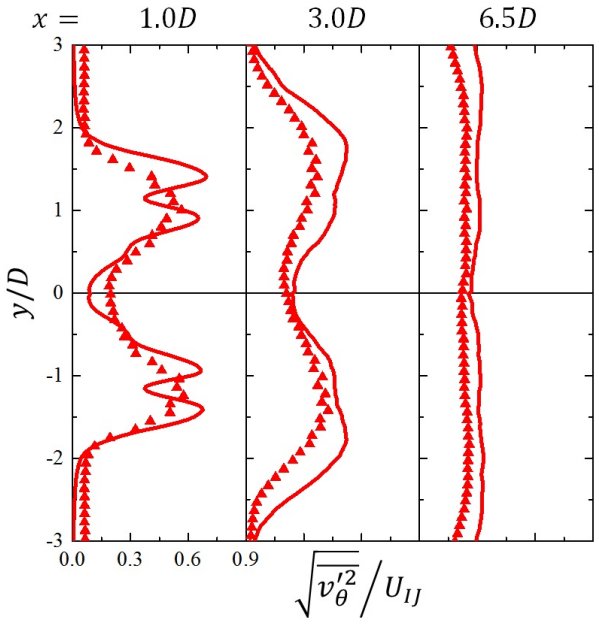
x = 1.0D 3.0D 6.5D
y/D
3
2
1
0
-1
-2
-3
0.0 0.3 0.6 0.9
√v'θ2/U_IJ

(b)

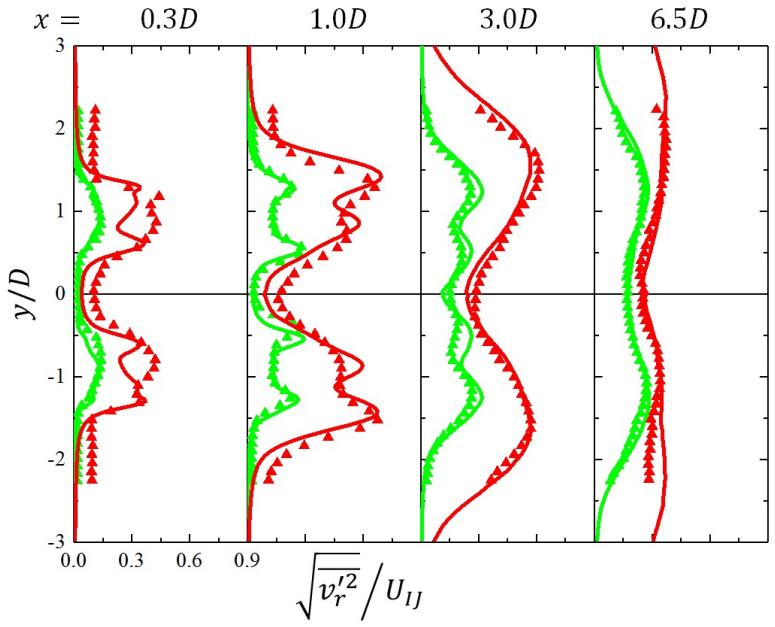

(c)

FIGURE 3.2: Comparison between numerical study and experiment: radial distribution of the turbulence intensities. Legend same as that for Figure 3.1. (a) Streamwise RMS velocity. (b) Azimuthal RMS velocity. (c) Radial RMS velocity.

Figure 3.2 shows the radial distribution of turbulence intensities. The computed streamwise and radial RMS velocities for case Sw0 display a good agreement with the experiment at all the streamwise locations. For the case Sw18, the level of upstream streamwise velocity fluctuations in the measurements is seen to be higher in OJ regions as compared to that in the simulation. At $x = 1.0D$, the IJ region of experiment exhibits higher fluctuations than that in the simulation, but the profile of computed fluctuations for OJ approaches towards the measurements. The downstream region displays the equivalent turbulence level. The simulation results show two peaks in a radial direction for the azimuthal RMS velocity, whereas the experiment shows the single peak. The presence of two peaks in OJ region can be traced back to the inlet condition (Figure 2.3(b)). Due to the unavailability of experimental upstream location data for azimuthal velocity fluctuations, the inflow distribution cannot be confirmed. At $x = 3.0D$, the simulation also shows a single peak in a radial direction, but the level is higher than the experimental intensity. From Figure 3.2(c), it is found that the profiles of radial velocity fluctuations for the simulation and experiment are reasonably collapsed at the location $x/D = 0.3$ in the IJ region, while OJ again exhibits the lower turbulence level for the simulation. The downstream simulation results show better agreement with the experimental ones.

The overall results suggest that the agreement between the simulation and experiment for the case Sw0 is remarkable. The discrepancy is observed for the case Sw18, but the trends seem to be identical. Note that the mean and RMS velocities presented here are just for the purpose of comparison between the simulation and experiment, and they are detailed in the subsequent sections.

3.3 Instantaneous flow features

Figure 3.3 shows the contours for the instantaneous streamwise velocity with vector field for the three cases. The instantaneous streamwise velocity contours show the negligible decay in the non-swirling case, while its overall vector field aligns with the streamwise direction. In case Sw05, the effect of swirl can be seen in both streamwise velocity and the vector field. The decay of streamwise velocity is observed with the spread. Vector field is in the state of slight disorder. Case Sw18, i.e., the case of strong swirl, has by far undergone the significant change. The spread of the jets is increased. The flow reversal is observed in the annular region between two jets at upstream and in the central region at downstream. Note that the occurrence of IRZ is consistent with the findings of Ben-Yeoshua (1993) (see Figure 1.2 and note that the conditions of present case Sw18 are $\dot{m}_r = 10.64$ and $Sw = 1.8$). Vector field demonstrates the chaotic structures initiating close to the nozzle exit.

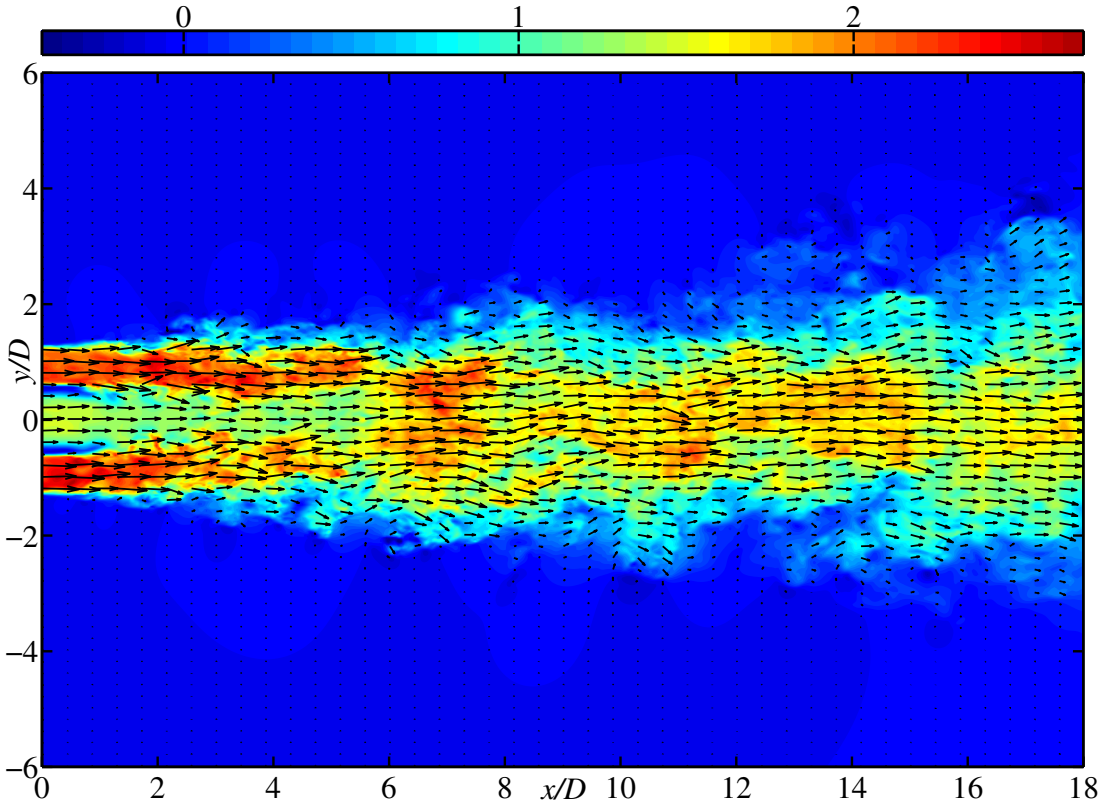
0
1
2
6
4
2
0
−2
−4
−6
y/D
0
2
4
6
8
x/D
10
12
14
16
18

(a)

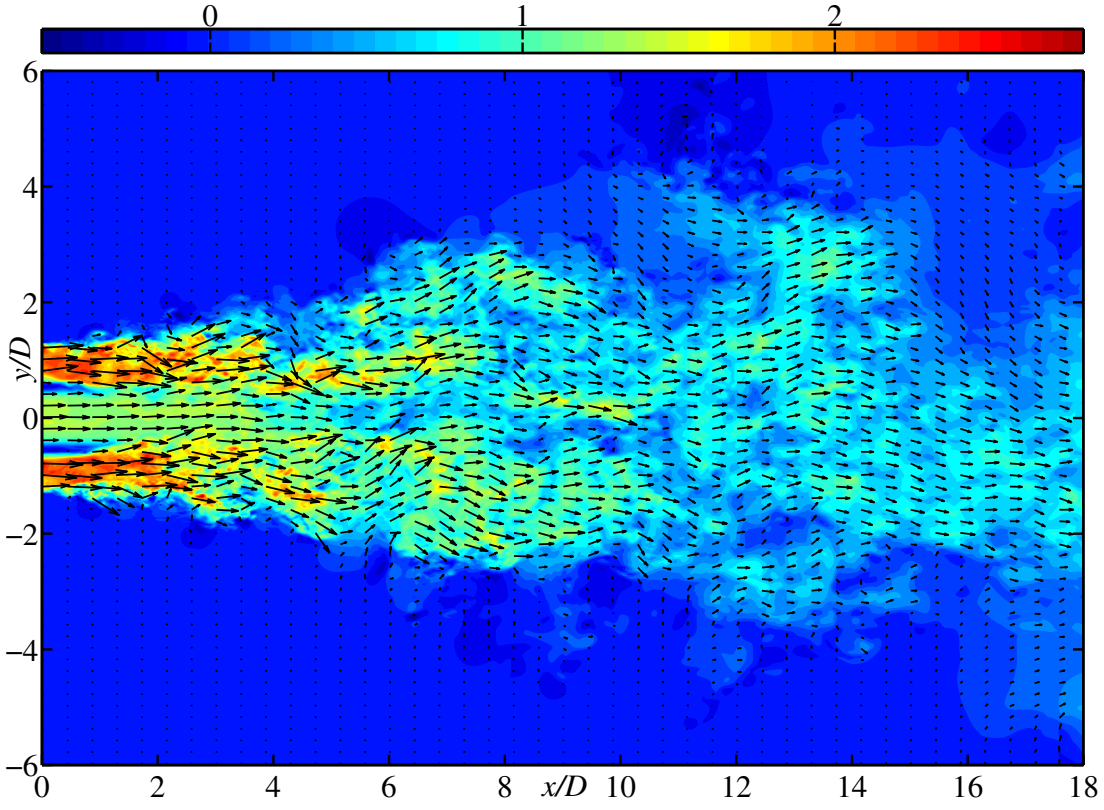
0
1
2
6
4
2
0
−2
−4
−6
y/D
0
2
4
6
8
x/D
10
12
14
16
18

(b)

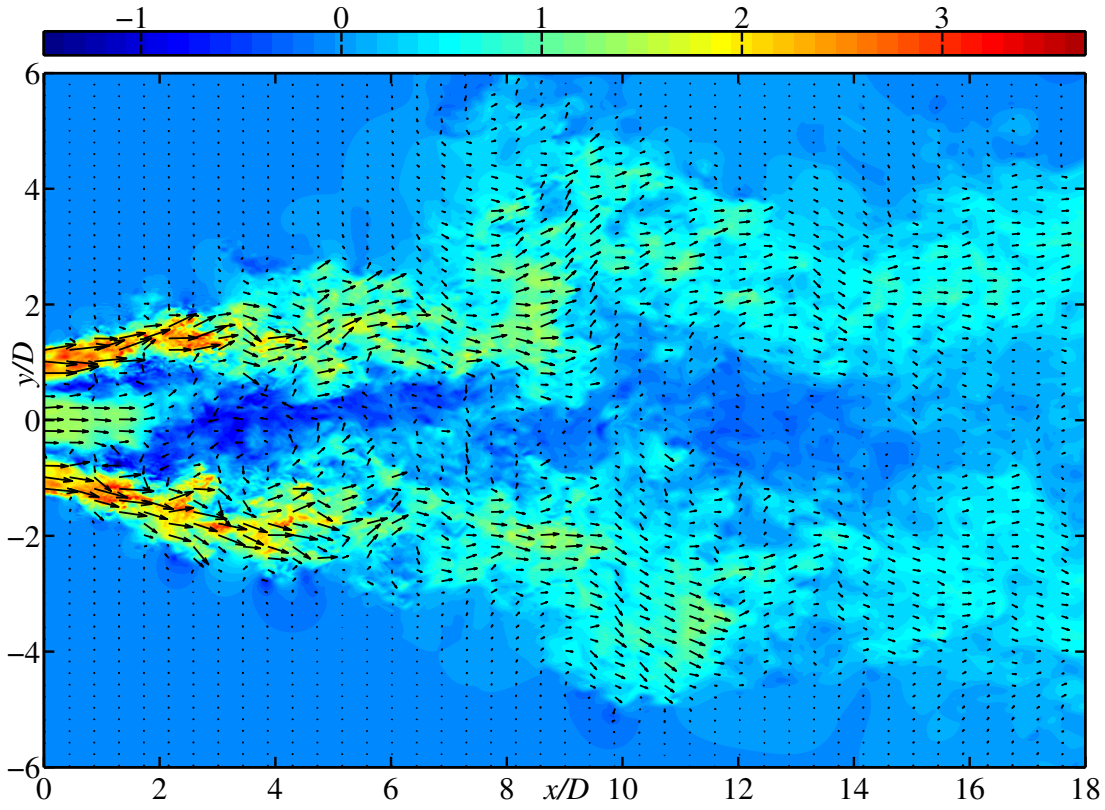

(c)

FIGURE 3.3: Instantaneous streamwise velocity u/U_{IJ} contours with vector field at the central plane for cases (a) Sw0, (b) Sw05, and (c) Sw18.

3.4 Mean flow development

Figures 3.4 and 3.5 present mean streamwise velocity contour maps with mean streamlines and mean static pressure, respectively, at the central cross-sectional plane for the three test cases. Figure 3.6 compares the centerline variation of mean streamwise velocity and mean static pressure. Figure 3.7 presents the mean azimuthal velocity contour maps for the swirling cases only, i.e., cases Sw05 and Sw18 (it is not presented for the case Sw0 due to the absence of azimuthal momentum).

The case Sw0 (shown in Figures 3.4(a) and 3.6) exhibits a decrease in centerline streamwise velocity until $x \leq 2.0D$. This is caused by the positive pressure gradient of static pressure (see Figure 3.5(a)) and was also observed by Rehab *et al.* (1997). The gradual increase in mean streamwise velocity thereafter marks the entrainment of OJ fluid having a high streamwise velocity toward the centerline.

With the introduction of swirl in case Sw05, a large deficit in static pressure is established in the central region $r \leq 0.6D$ close to the nozzle exit (see Figures 3.5(b) and 3.6), which is caused by centrifugal force that leads to the positive radial gradient of static pressure in the OJ region $0.6 < r/D < 1.3$ (because the approximation equation for mean radial momentum yields $\partial\overline{p}/\partial r \propto \overline{V_\theta}^2/r$). Based on the fact that azimuthal velocity decays in the downstream region (see Figure 3.7(a)), the static pressure at the downstream region approaches that in the ambient region and an adverse pressure gradient is generated in the axial direction. Figure 3.4(b) reveals a brief deceleration in the region $x < 2.0D$ based on this adverse axial gradient of static pressure. However, an increase in centerline streamwise velocity can be observed in the region $1.0 \leq x/D \leq 2.0$ and can be attributed to the slightly negative axial gradient of static pressure in that region. The strong influence of swirl at the centerline can be observed in the downstream region, where the flow decelerates continuously with expansion of the jets. Furthermore, the streamwise velocity in the OJ region decreases at a rate more rapid than that in case Sw0.

With a further increase in the swirling strength in case Sw18 (see Figure 3.7(b)), a very strong adverse pressure gradient is established (see Figures 3.5(c) and 3.6). The contour maps of streamwise velocity, which are presented in Figure 3.4(c), reveal an internal recirculation zone (IRZ) or a feature of VB spanning over $2.5 \leq x/D \leq 8.1$ on the centerline. This is formed as a result of the adverse pressure gradient. Similar IRZ structure is observed by Santhosh *et al.* (2013) and they termed it as a partially-penetrated VBB since the IJ penetrates the IRZ. The IRZ is characterized by flow reversal in the annular region between the two jets and the axis-symmetric vortex ring located in the downstream region. The latter characteristic is responsible for bringing the OJ fluid into the central region, ultimately resulting in mixing improvement. The stronger ISL (i.e., steeper radial gradient of mean streamwise velocity) is featured as a consequence of annular reversed flow. Furthermore, the IJ flow is directed radially outward through the annular reversed flow, which also improves mixing characteristics. Thus, IRZ is a key outcome of the swirling jet. The radial extent of the OJ also steadily increases in the streamwise direction.

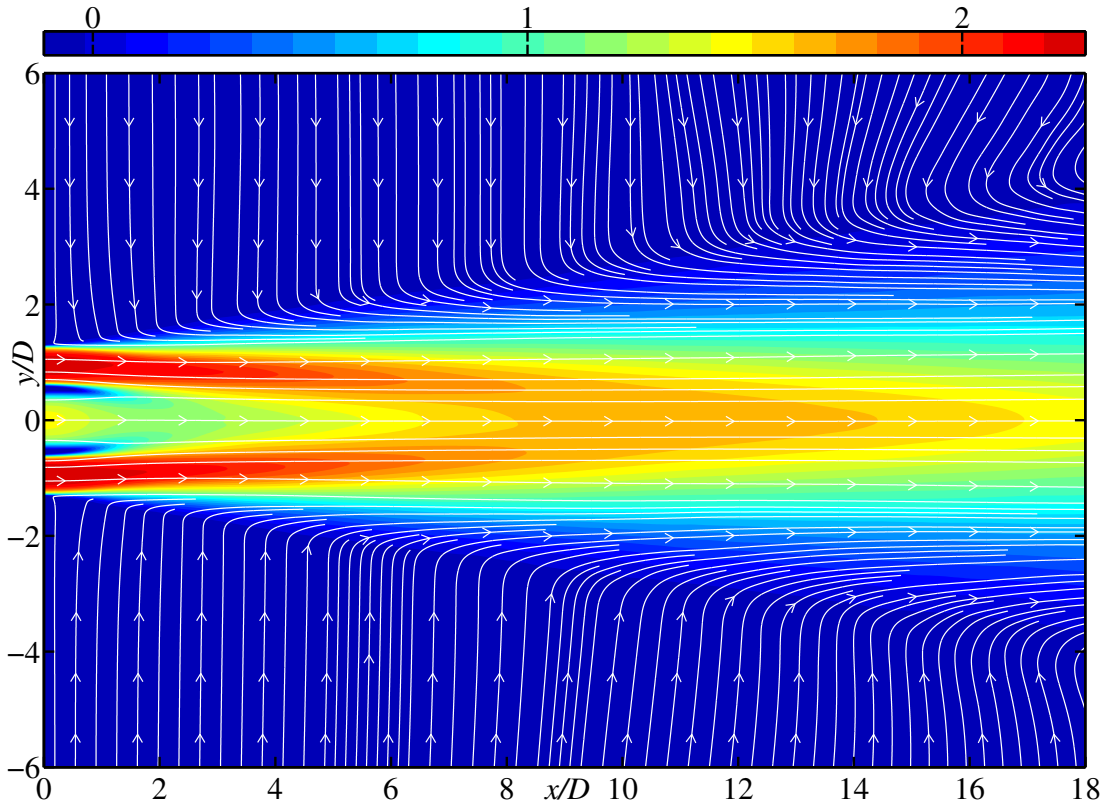
0
1
2
6
4
2
0
−2
−4
−6
y/D
0
2
4
6
8
x/D
10
12
14
16
18

(a)

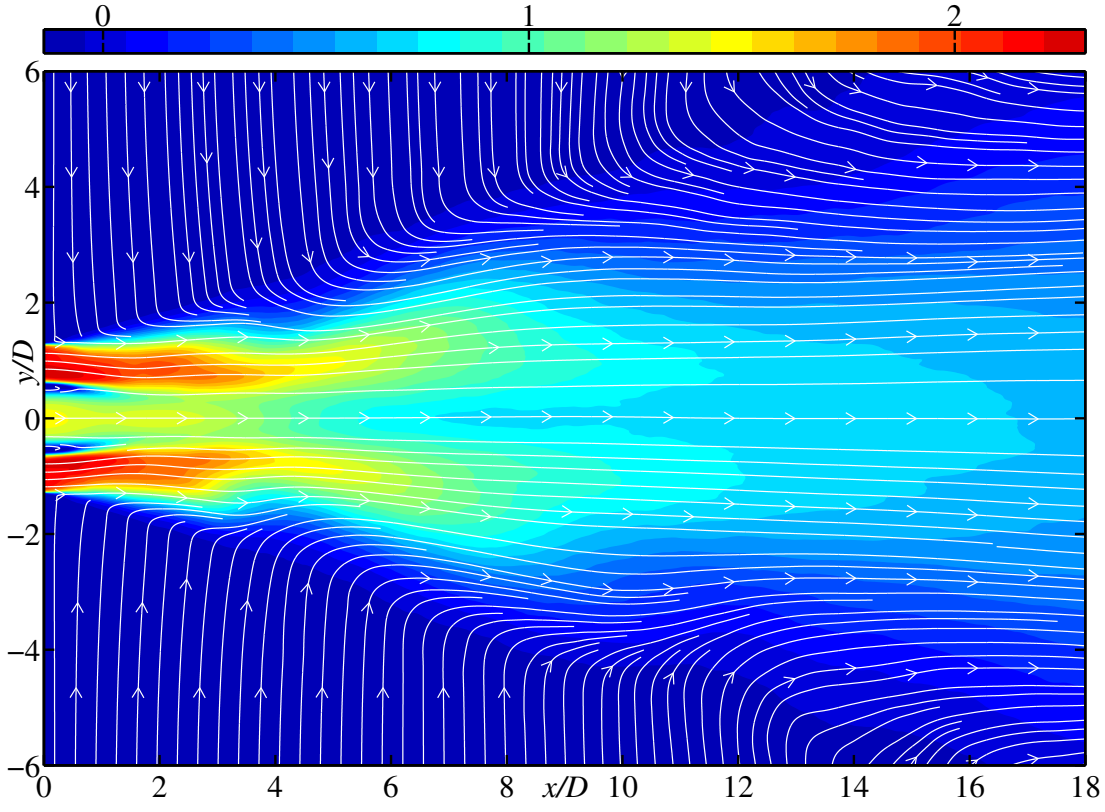
0
1
2
6
4
2
0
−2
−4
−6
y/D
0
2
4
6
8
x/D
10
12
14
16
18

(b)

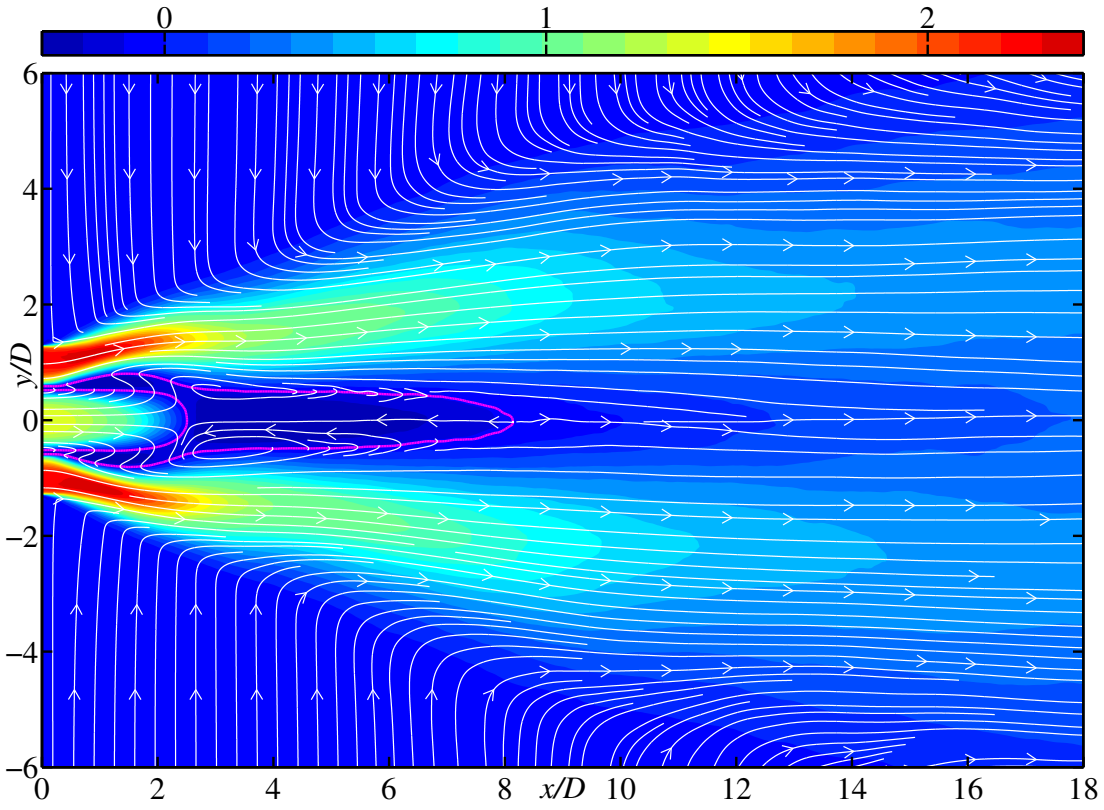

(c)

FIGURE 3.4: Mean streamwise velocity $\overline{U}/U_{IJ}$ contour maps with mean streamlines for cases (a) Sw0, (b) Sw05, and (c) Sw18. The pink line for case Sw18, which is an isoline of $\overline{U}/U_{IJ} = 0$, encloses an internal recirculation zone (IRZ).

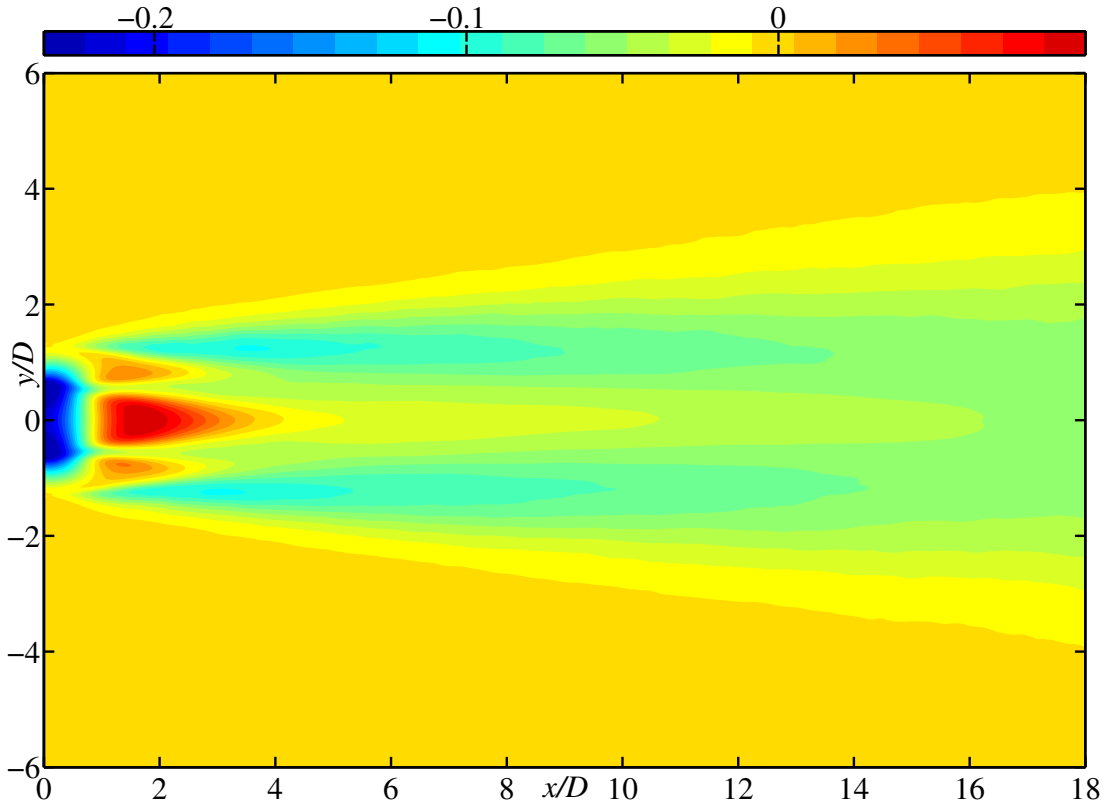
−0.2
−0.1
0
6
4
2
0
−2
−4
−6
y/D
0
2
4
6
8
x/D
10
12
14
16
18

(a)

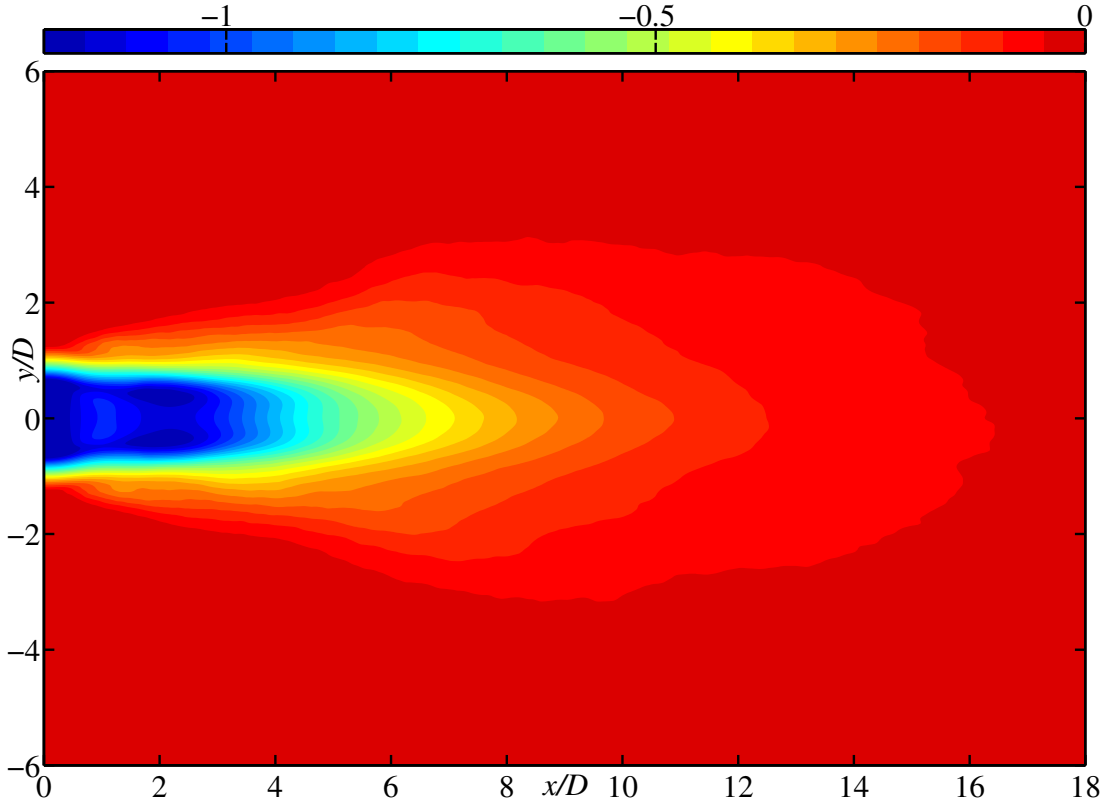
−1
−0.5
0
6
4
2
0
−2
−4
−6
y/D
0
2
4
6
8
x/D
10
12
14
16
18

(b)

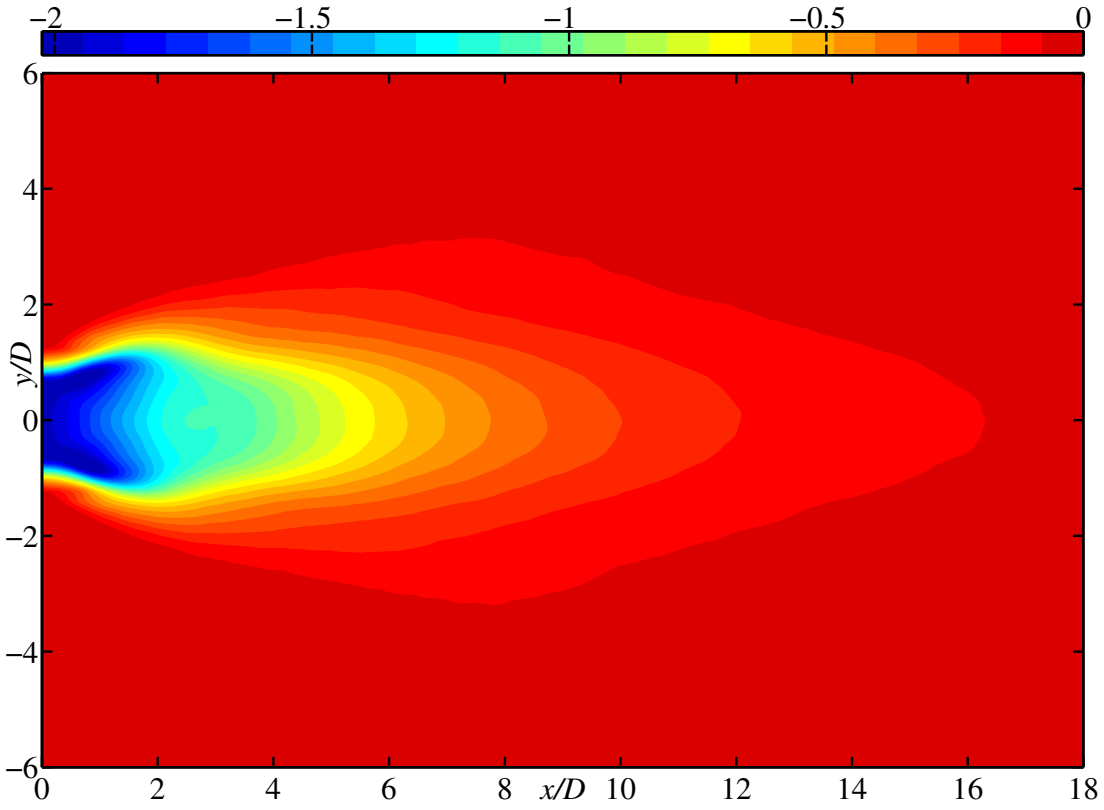

(c)

FIGURE 3.5: Mean static pressure $\overline{P}/(\rho U_{IJ}^2)$ contour maps for cases (a) Sw0, (b) Sw05, and (c) Sw18.

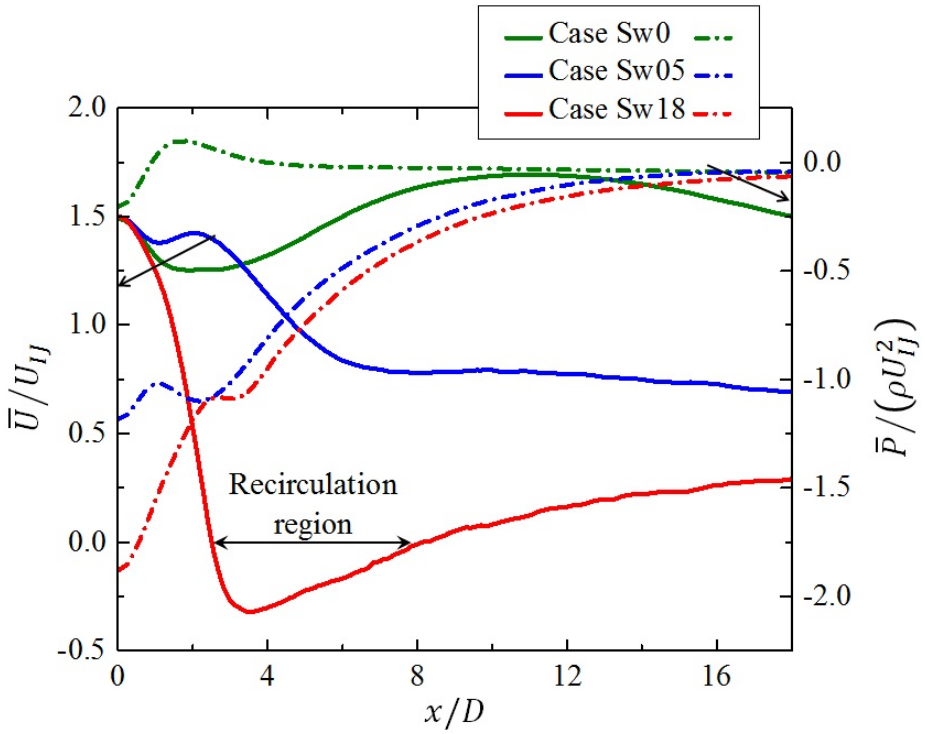

FIGURE 3.6: Centerline distribution of mean streamwise velocity and mean static pressure. Solid lines: mean streamwise velocity, and dotted lines: mean static pressure.

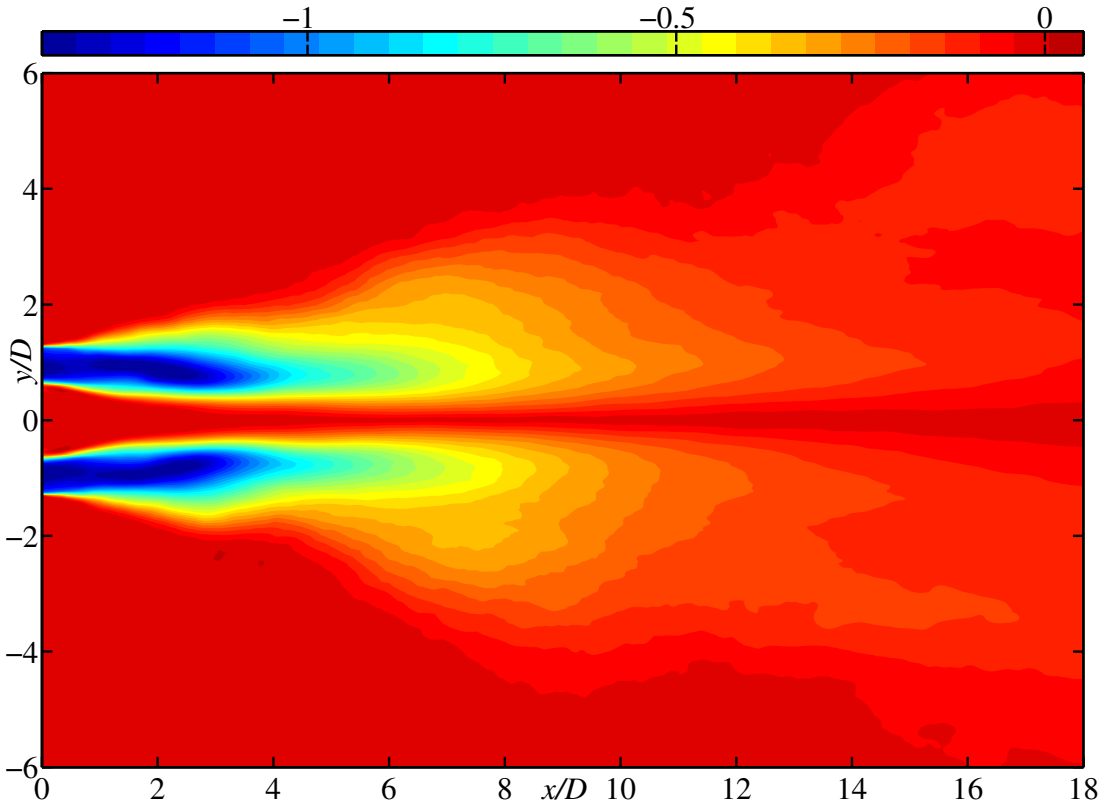

(a)

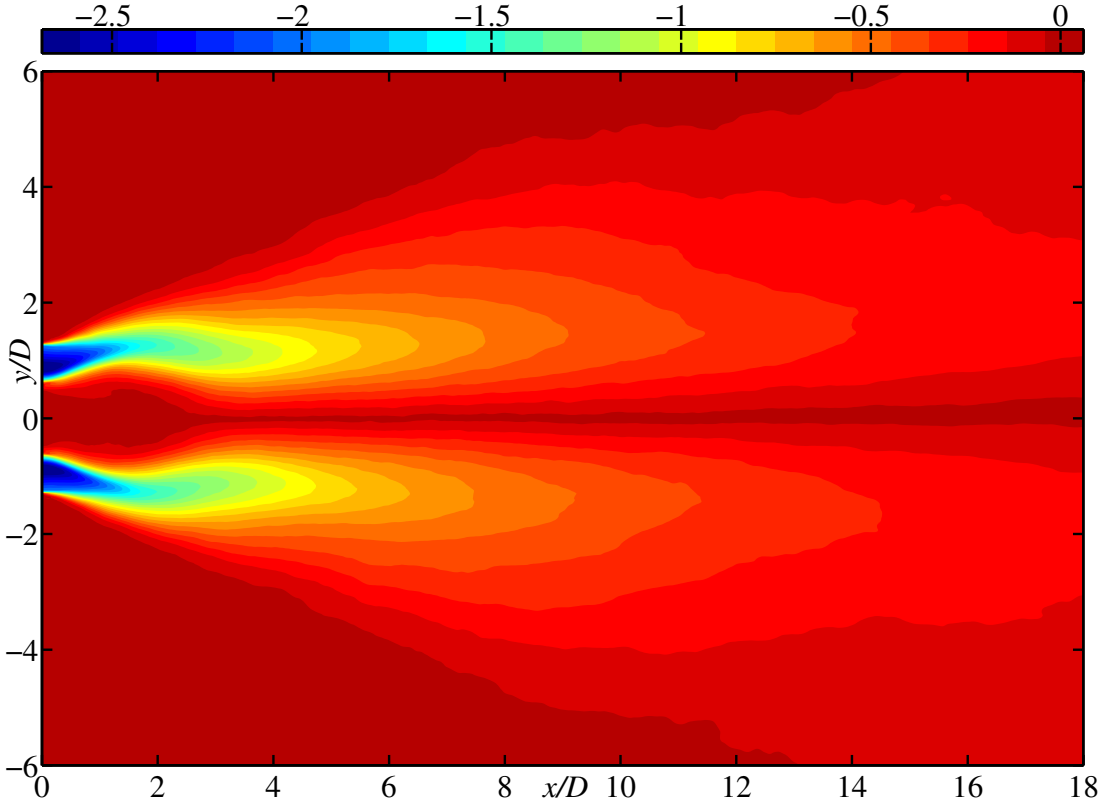

(b)

FIGURE 3.7: Mean azimuthal velocity $\overline{V_\theta}/U_{IJ}$ contour maps for cases (a) Sw05, and (b) Sw18.

3.5 Reynolds stresses and turbulent kinetic energy

Figure 3.8 shows the radial distribution of Reynolds normal stresses and TKE at various streamwise locations. The streamwise stress, $\overline{u'^2}$, plotted in Figure 3.8(a) exhibits the same level of intensity for all the cases in the inner region ($r \leq 0.3D$) close to the jet exit, with a slight increase in the region $0.3 < r/D \leq 1.0$ of case Sw18. The level of outer peaks for both swirling cases is increased with case Sw18 having highest $\overline{u'^2}$. At $x = 1.0D$, cases Sw0 and Sw05 exhibit a considerable increment in the level of streamwise stress, however, the level for case of Sw18 is immensely increased, especially in the ISL2 ($0.6 \leq r/D \leq 1.2$) and OSL ($1.2 \leq r/D \leq 1.8$). The peaks in case Sw18 are also moved radially outward and the peak in ISL2 ($r \approx 0.9D$) exceeds the OSL peak ($r \approx 1.4D$) in magnitude. The downstream region sees the spread of streamwise stress in radial outward as well as inward directions. The inner region $r < 0.5D$ of case Sw18 exhibits the higher streamwise stress at the pre-IRZ location $x = 2.0D$, thereafter it starts reducing. The case Sw05 shows higher $\overline{u'^2}$ at the location $x = 3.0D$ than that for the non-swirling case but still has a lower magnitude than case Sw18. By $x = 5.0D$, only a single peak is observed in all three cases, and by $x = 8.0D$, the swirling cases show the approximately equal peak magnitudes as in the non-swirling case, which lacks the spread.

The remaining Reynolds normal stresses, i.e., azimuthal ($\overline{v'^2_\theta}$) and radial ($\overline{v'^2_r}$) stresses, depicted in Figures 3.8(b) and 3.8(c) respectively, show similar trend as that of streamwise stress with varied magnitudes. Both components are smaller in magnitude for the non-swirling case as compared to the swirling cases. The distribution again shows two peaks at $x = 1.0D$ for both components of all the cases, however outer peaks of swirling cases are higher in magnitude. TKE (k) in Figure 3.8(d) replicates the similar trend as that in the normal stresses. A noteworthy intensification in the level of TKE is observed at $x = 1.0D$ for case Sw18 as compared to other two cases. Moreover, the two peaks observed at $x = 1.0D$ in shear layers are of the same magnitude in case Sw18. The peak levels for swirling cases become comparable to that for non-swirling case by $x = 8.0D$.

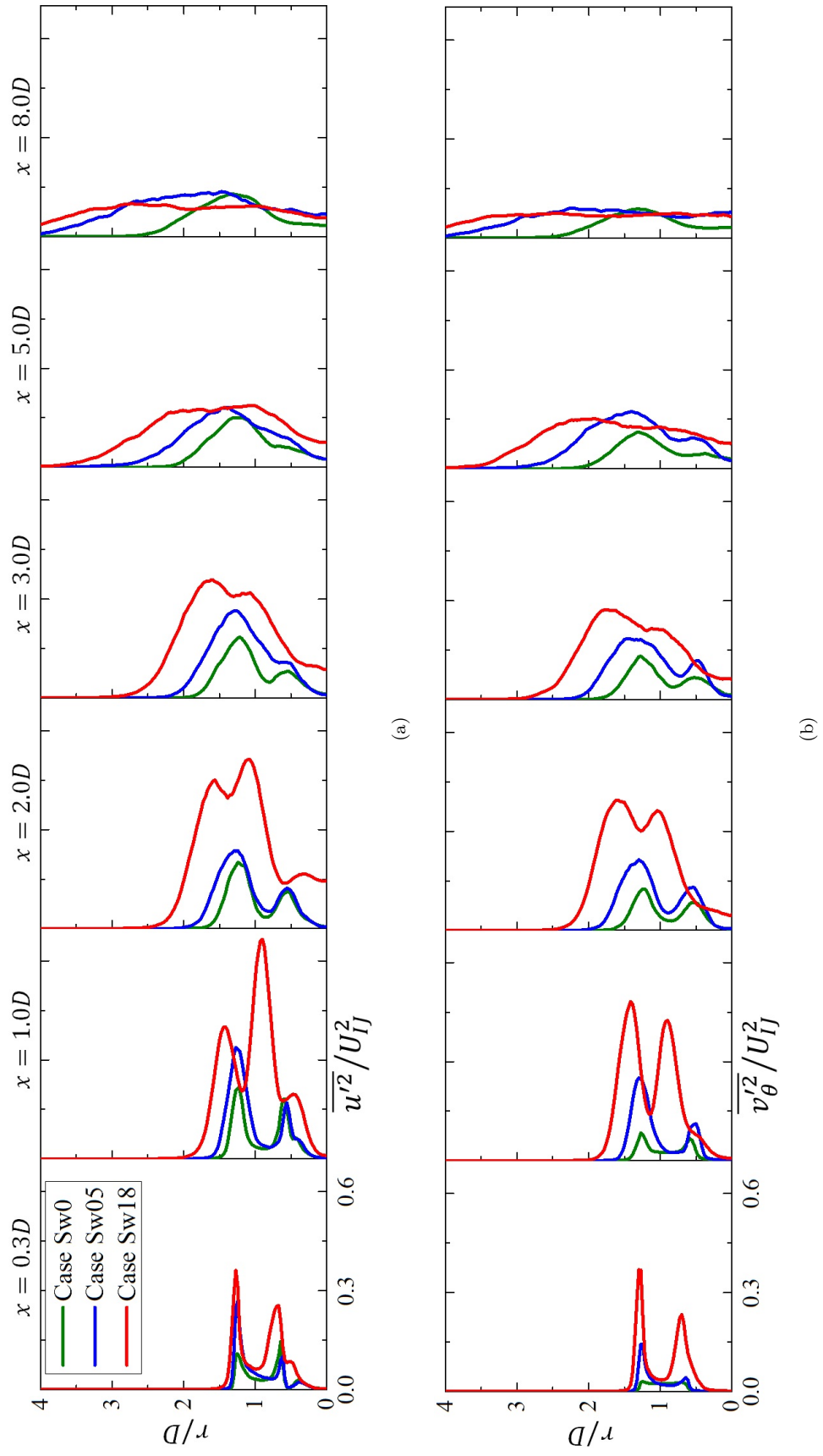
x = 0.3D
x = 1.0D
x = 2.0D
x = 3.0D
x = 5.0D
x = 8.0D
Case Sw0
Case Sw05
Case Sw18
r/D
$\overline{u'^2}/U_{IJ}^2$
$\overline{v_\theta'^2}/U_{IJ}^2$
(a)
(b)

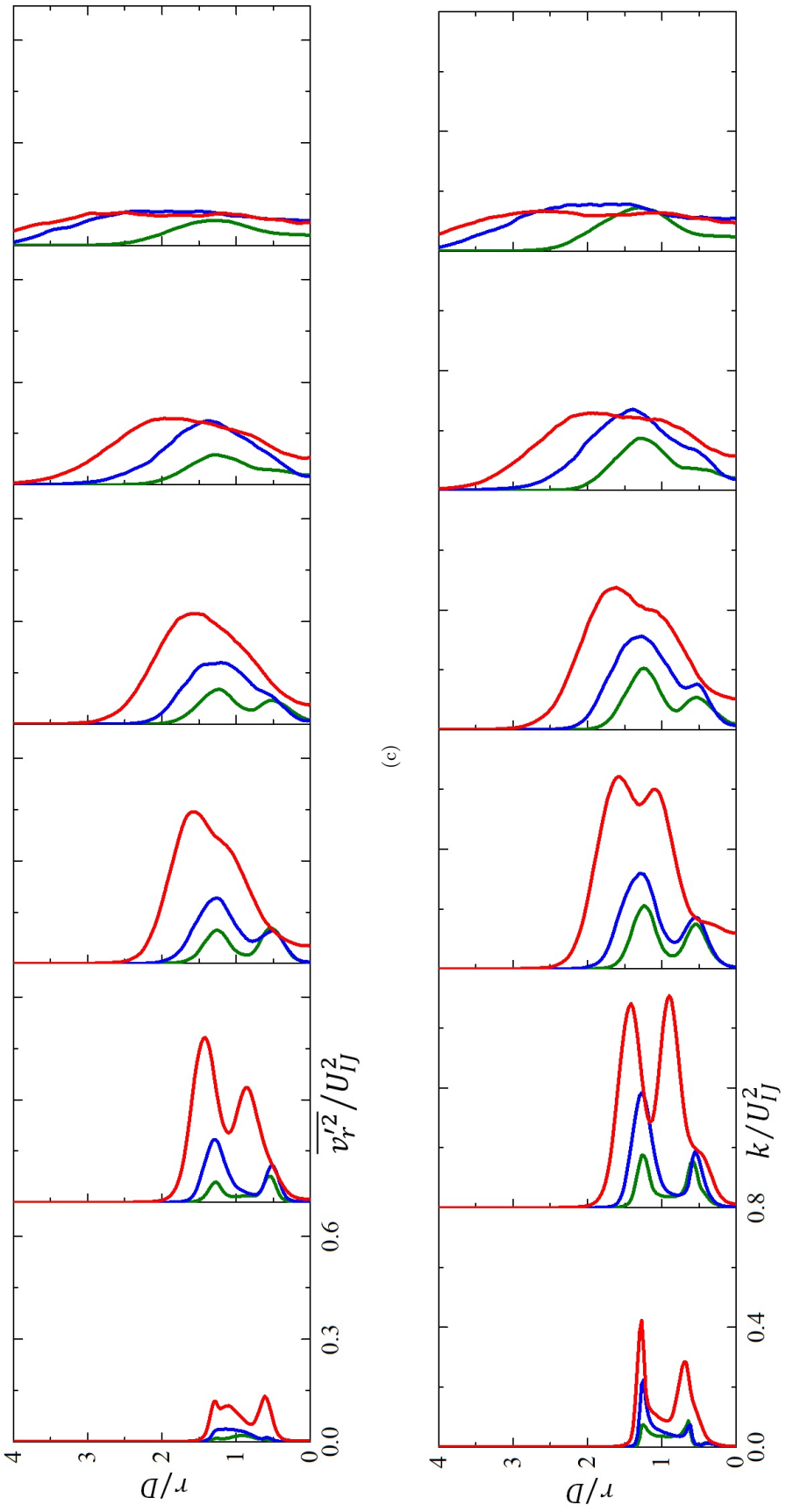

FIGURE 3.8: Radial distribution of Reynolds normal stresses and TKE. (a) Reynolds normal stress $\overline{u'^2}$. (b) Reynolds normal stress $\overline{v_\theta'^2}$. (c) Reynolds normal stress $\overline{v_r'^2}$. (d) TKE, $k = \overline{q^2}/2 = (\overline{u'^2} + \overline{v_\theta'^2} + \overline{v_r'^2})/2$

The radial distribution of the Reynolds primary shear stress, $\overline{u'v'_r}$, is shown in Figure 3.9(a). The shear stress $\overline{u'v'_r}$, which is responsible for the radial flux of axial momentum and hence for the spread of jets, is observed to be very high in the region $x \leq 5.0D$ for case Sw18. This is the consequence of the large velocity gradients developed due to the IRZ, forming the strong shear layers. The peak levels in case Sw18, however, approaches to the other two cases in the downstream region. The Reynolds secondary shear stresses $\overline{u'v'_\theta}$ and $\overline{v'_\theta v'_r}$ are plotted in Figures 3.9(b) and 3.9(c) respectively. A substantial increment for both secondary shear stress is noted in the presence of swirling motion. On the other hand, the case Sw0 does not show significant secondary shear stresses, which is due to the absence of credible azimuthal as well as radial momentum resulting into the negligible production.

The above discussion shows significant variations in the distributions of Reynolds stresses and TKE due to the introduction of swirl. Thus, to examine the enhancement of turbulence level, the budgets of TKE and Reynolds normal stresses are investigated along for cases Sw0 and Sw18 at the locations $x/D = 0.3$, 1.0, and 3.0, which see rapid changes.

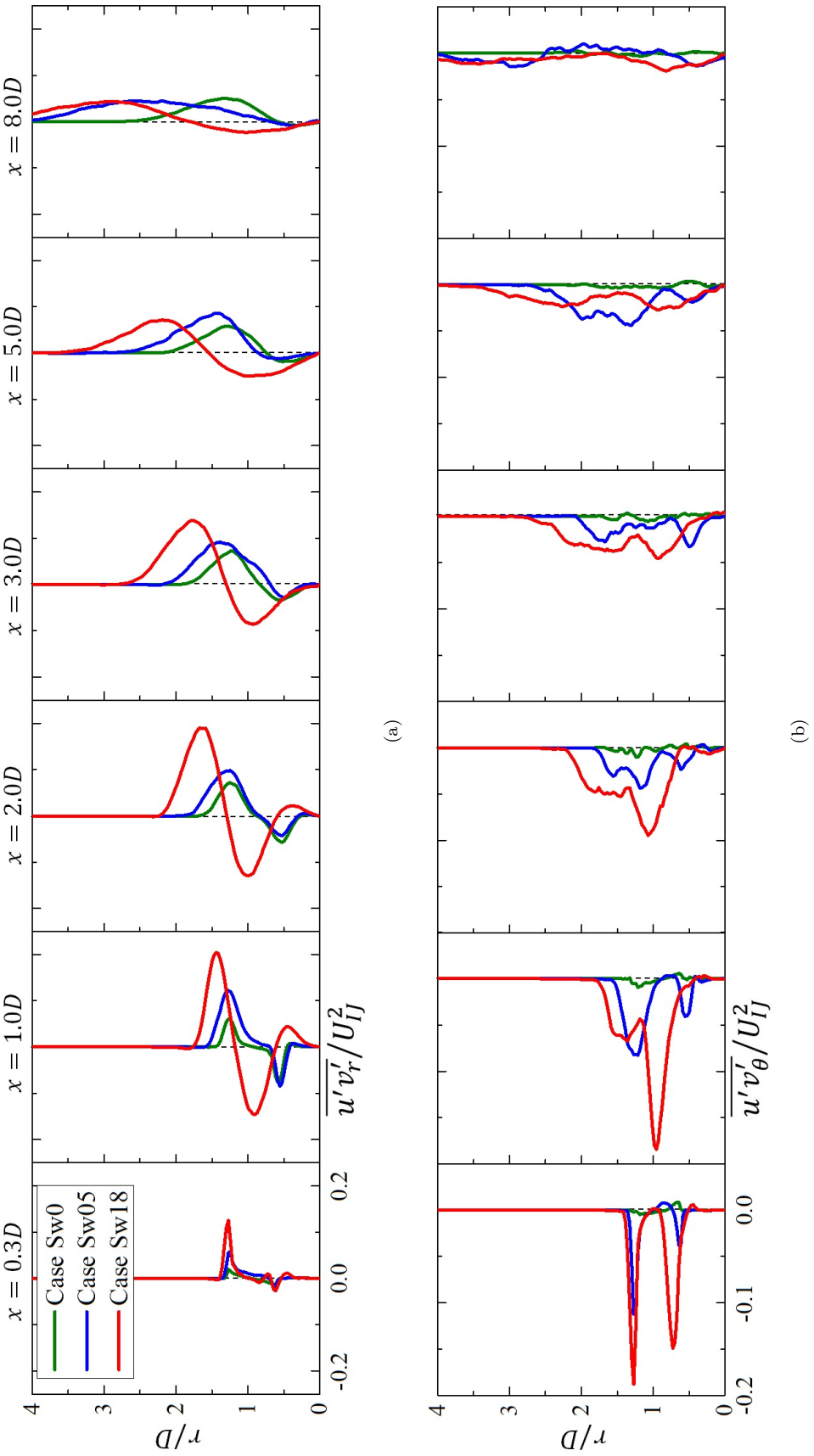
x = 8.0D
x = 5.0D
x = 3.0D
x = 2.0D
x = 1.0D
x = 0.3D
Case Sw0
Case Sw05
Case Sw18
r/D
$\overline{u'v'_r}/U_{IJ}^2$
$\overline{u'v'_\theta}/U_{IJ}^2$
(a)
(b)

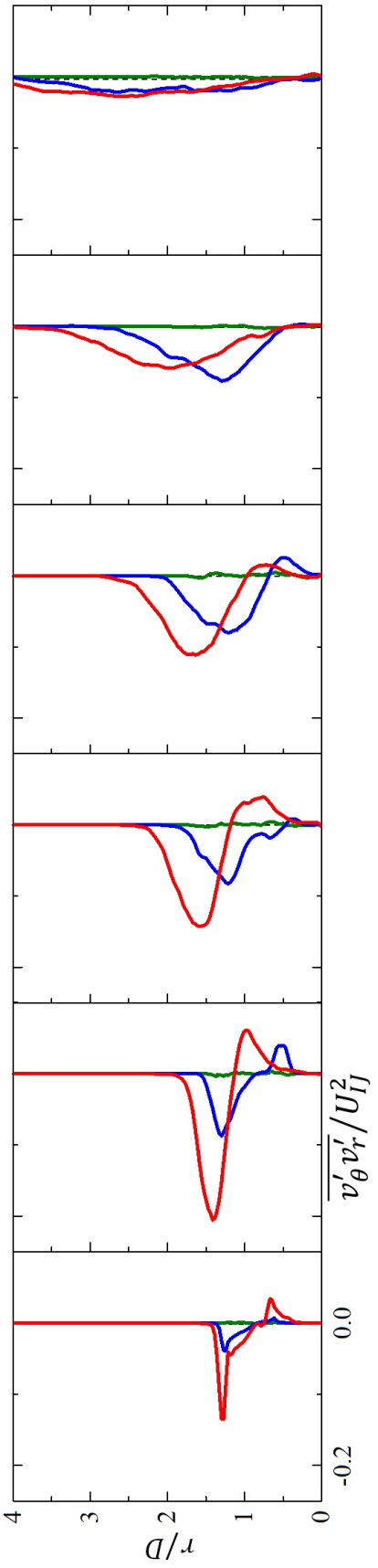

FIGURE 3.9: Radial distribution of Reynolds shear stresses. (a) Reynolds primary shear stress $\overline{u'v'_r}$. (b) Reynolds secondary shear stress $\overline{u'v'_\theta}$. (c) Reynolds secondary shear stress $\overline{v'_\theta v'_r}$.

3.6 Budgets analysis

3.6.1 Turbulent kinetic energy

The collective contribution of Reynolds stresses in generating TKE is studied in this section. The transport equation for TKE is given by,

$$0 = C_k + D_k^P + D_k^T + D_k^\nu + P_k + \epsilon_k, \tag{3.1}$$

where C_k is convection term, D_k^P is pressure diffusion term, D_k^T is turbulent diffusion term, D_k^ν is viscous diffusion term, P_k is production term, and ϵ_k is dissipation term. The equation is normalized by U_{IJ}^3/D. Flow axis-symmetry allows the angular gradient of mean variable to be neglected. Terms of TKE budget are taken in the cylindrical coordinate system. Each term is stated as follows (Shiri (2010)):

$$C_k = -\left\{\overline{U}\frac{\partial k}{\partial x} + \overline{V_r}\frac{\partial k}{\partial r} - \overline{V_\theta}\frac{\overline{v_r' v_\theta'}}{r} + \overline{V_r}\frac{\overline{v_\theta'^2}}{r}\right\}, \tag{3.2a}$$

$$D_k^P = -\left\{\frac{\partial \overline{p'u'}}{\partial x} + \frac{1}{r}\frac{\partial r\overline{p'v_r'}}{\partial r}\right\}, \tag{3.2b}$$

$$D_k^T = -\frac{1}{2}\left\{\frac{\partial \overline{u'q^2}}{\partial x} + \frac{1}{r}\frac{\partial r\overline{v_r'q^2}}{\partial r}\right\}, \tag{3.2c}$$

$$\begin{aligned} D_k^\nu = &\frac{1}{Re_D}\left\{\frac{\partial}{\partial x}\left(\frac{\partial k}{\partial x} + \frac{\partial \overline{u'^2}}{\partial x} + \frac{1}{r}\frac{\partial r\overline{u'v_r'}}{\partial r}\right)\right. \\ &\left. + \frac{1}{r}\frac{\partial}{\partial r}r\left(\frac{\partial k}{\partial r} + \frac{\partial \overline{u'v_r'}}{\partial x} + \frac{1}{r}\frac{\partial r\overline{v_r'^2}}{\partial r} - \frac{\overline{v_\theta'^2}}{r}\right)\right\}, \end{aligned} \tag{3.2d}$$

$$\begin{aligned} P_k = &-\overline{u'^2}\frac{\partial \overline{U}}{\partial x} - \overline{u'v_r'}\frac{\partial \overline{U}}{\partial r} - \overline{u'v_r'}\frac{\partial \overline{V_r}}{\partial x} - \overline{v_r'^2}\frac{\partial \overline{V_r}}{\partial r} \\ &- \overline{u'v_\theta'}\frac{\partial \overline{V_\theta}}{\partial x} - \overline{v_r'v_\theta'}\frac{\partial \overline{V_\theta}}{\partial r}, \end{aligned} \tag{3.2e}$$

$$\begin{aligned} \epsilon_k = &-\frac{1}{Re_D}\left\{2\overline{\left(\frac{\partial u'}{\partial x}\right)^2} + 2\overline{\left(\frac{\partial v_r'}{\partial r}\right)^2} - 2\frac{\overline{v_r'^2}}{r^2}\right. \\ &+ 2\overline{\frac{1}{r^2}\left(\frac{\partial v_\theta'}{\partial \theta}\right)^2} + \overline{\left(\frac{\partial v_r'}{\partial x} + \frac{\partial u'}{\partial r}\right)^2} \\ &\left. + \overline{\left(\frac{1}{r}\frac{\partial v_r'}{\partial \theta} + r\frac{\partial}{\partial r}\left(\frac{v_\theta'}{r}\right)\right)^2} + \overline{\left(\frac{\partial v_\theta'}{\partial x} + \frac{1}{r}\frac{\partial u'}{\partial \theta}\right)^2}\right\}. \end{aligned} \tag{3.2f}$$

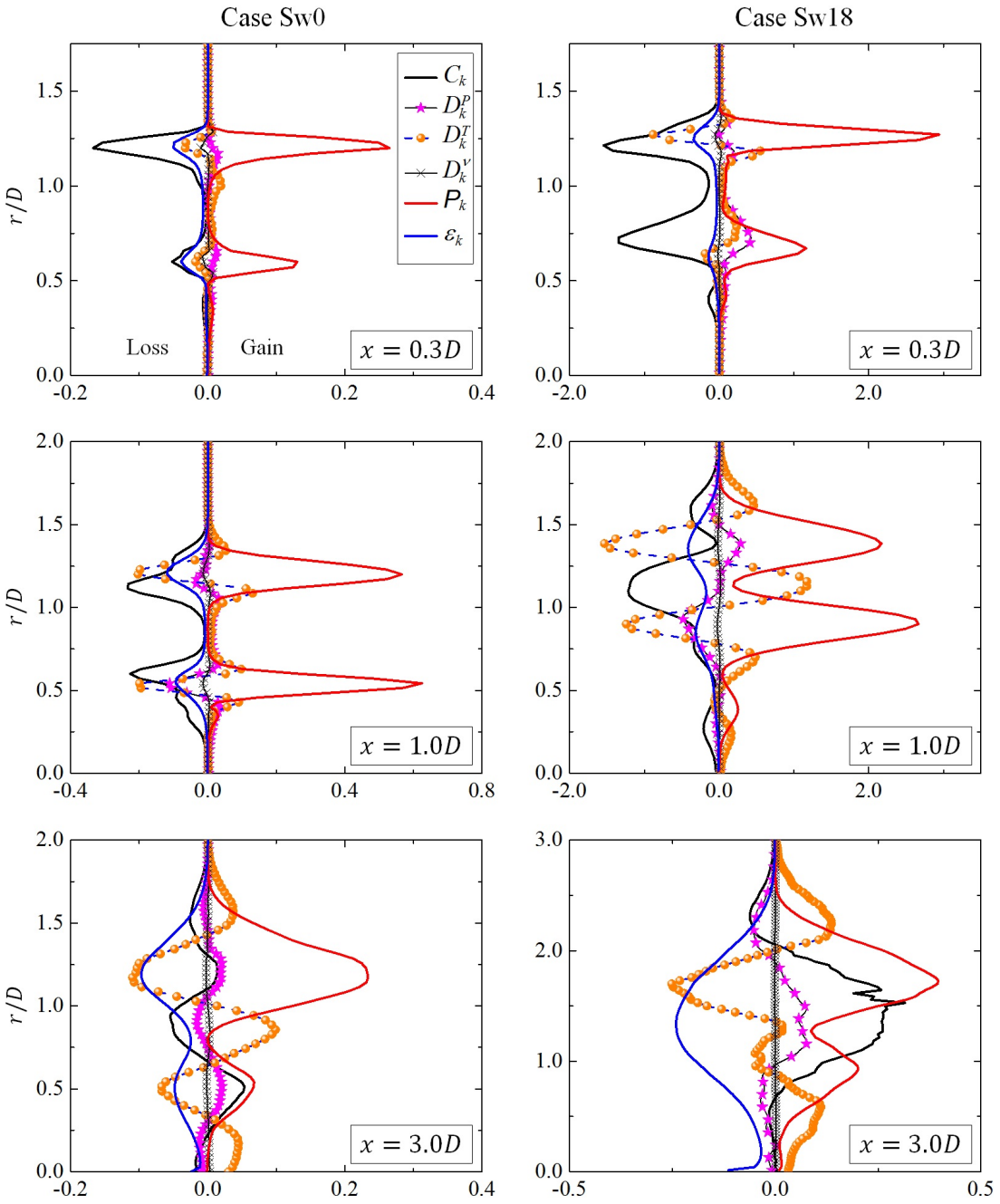

FIGURE 3.10: TKE budget at locations $x/D = 0.3$, 1.0, and 3.0 for cases Sw0 and Sw18.

Figure 3.10 shows the budget of TKE for the both cases at streamwise locations $x/D = 0.3$, 1.0, and 3.0. At $x = 0.3D$, TKE budgets exhibit insignificant activity in the jet central regions of both cases Sw0 ($r/D \leq 0.5$ for IJ and $0.7 \leq r/D \leq 1.0$ for OJ) and Sw18 ($r/D \leq 0.5$ for IJ and $0.9 \leq r/D \leq 1.1$ for OJ). Both the cases see the significant convection with negative contribution and the production of energy, whereas diffusion and dissipation also take part in a lesser extent. Note that the magnitudes of production peaks in the swirling case are

approximately 15 time higher than that in the non-swirling case.

At the downstream location $x = 1.0D$, the upstream trend continues for the case Sw0 with increased contribution from the turbulent diffusion and dissipation terms. However, the central regions of both jets ($r/D \leq 0.25$ for IJ and $0.7 \leq r/D \leq 1.0$ for OJ) continue to show negligible values. For case Sw18, apart from the significantly higher production of TKE, a noteworthy turbulent diffusion is observed. Here, TKE produced in the regions $0.8 \leq r/D \leq 1.0$ and $1.3 \leq r/D \leq 1.5$ is transported in the central region of OJ ($1.0 \leq r/D \leq 1.3$) due to the turbulent diffusion, and hence the corresponding region sees a significant TKE (see Figure 3.8(d)). The convection term is remained to be negative in both the cases and sizable pressure diffusion and dissipation are also observed.

At location $x = 3.0D$, the budgets are expanded radially with the reduced order of magnitude. Diffusion of the energy from shear layers ($0.3 \leq r/D \leq 0.7$ and $1.0 \leq r/D \leq 1.4$) to the central region of OJ ($0.7 \leq r/D \leq 1.0$) in case Sw0, which was seen at the upstream location $x = 1.0D$ in case Sw18, is taken place here. The IJ region ($r/D \leq 0.3$) of case Sw0 and the central region ($r/D \leq 0.8$) of case Sw18 see considerable positive contribution of turbulent diffusion. Unlike the upstream location, energy is gained due to the convection in the region $0.7 < r/D < 2.0$ of case Sw18, while the equivalent amount of energy is dissipated. This suggests an important feature in which the energy for $r/D > 0.5$ (not the IRZ region) is convected forward from the upstream highly-energetic region to this location. However, the positive contribution of the convective term is smaller in case Sw0.

Since the interesting features, such as heightened production and higher turbulent diffusion at upstream region due to the introduction of swirl, are appeared in the TKE budget, more insight can be obtained into these features by investigating the budgets of individual Reynolds normal stresses (presented in §3.6.2).

3.6.2 Reynolds normal stresses

Transport equation for Reynolds stresses is given by,

$$0 = C_{ij} + \Pi_{ij} + D^P_{ij} + D^T_{ij} + D^\nu_{ij} + P_{ij} + \epsilon_{ij}, \tag{3.3}$$

where C is convection term, Π is pressure-strain correlation term, D^P is pressure diffusion term, D^T is turbulent diffusion term, D^ν is viscous diffusion term, P is

production term, and ϵ is dissipation term. Subscripts for the terms of equation denote the corresponding Reynolds stress component. Terms of the above equation for each Reynolds stress are taken in the cylindrical coordinate system (Shiri (2010); Moser & Moin (1984)). The equations are normalized by U_{IJ}^3/D. The terms in the production are designated individually to study them separately.

Terms of momentum transfer equation for Reynolds normal stress $\overline{u'^2}$,

$$C_{uu} = -\left\{\overline{U}\frac{\partial\overline{u'^2}}{\partial x} + \overline{V_r}\frac{\partial\overline{u'^2}}{\partial r}\right\}, \tag{3.4a}$$

$$\Pi_{uu} = 2\,\overline{p'\frac{\partial u'}{\partial x}}, \tag{3.4b}$$

$$D_{uu}^P = -2\,\frac{\partial\overline{p'u'}}{\partial x}, \tag{3.4c}$$

$$D_{uu}^T = -\frac{\partial\overline{u'^3}}{\partial x} - \frac{1}{r}\frac{\partial r\overline{u'^2v_r'}}{\partial r}, \tag{3.4d}$$

$$D_{uu}^\nu = \frac{1}{Re_D}\left\{\frac{\partial^2\overline{u'^2}}{\partial x^2} + \frac{1}{r}\frac{\partial}{\partial r}\left(r\frac{\partial\overline{u'^2}}{\partial r}\right)\right\}, \tag{3.4e}$$

$$P_{uu} = \underbrace{-2\overline{u'^2}\frac{\partial\overline{U}}{\partial x}}_{P_{uu}^{U,x}}\underbrace{-2\overline{u'v_r'}\frac{\partial\overline{U}}{\partial r}}_{P_{uu}^{U,r}}, \tag{3.4f}$$

$$\epsilon_{uu} = -\frac{2}{Re_D}\left\{\overline{\left(\frac{\partial u'}{\partial x}\right)^2} + \overline{\left(\frac{\partial u'}{\partial r}\right)^2} + \overline{\left(\frac{1}{r}\frac{\partial u'}{\partial\theta}\right)^2}\right\}. \tag{3.4g}$$

Terms of momentum transfer equation for Reynolds normal stress $\overline{v_\theta'^2}$,

$$C_{v_\theta v_\theta} = -\left\{\overline{U}\frac{\partial\overline{v_\theta'^2}}{\partial x} + \overline{V_r}\frac{\partial\overline{v_\theta'^2}}{\partial r} + 2\overline{V_r}\frac{\overline{v_\theta'^2}}{r}\right\}, \tag{3.5a}$$

$$\Pi_{v_\theta v_\theta} = \frac{2}{r}\,\overline{p'\frac{\partial v_\theta'}{\partial\theta}}, \tag{3.5b}$$

$$D_{v_\theta v_\theta}^P = 0, \tag{3.5c}$$

$$D_{v_\theta v_\theta}^T = -\frac{\partial\overline{u'v_\theta'^2}}{\partial x} - \frac{1}{r}\frac{\partial r\overline{v_r'v_\theta'^2}}{\partial r} - 2\frac{\overline{v_r'v_\theta'^2}}{r}, \tag{3.5d}$$

$$D_{v_\theta v_\theta}^\nu = \frac{1}{Re_D}\left\{\frac{\partial^2\overline{v_\theta'^2}}{\partial x^2} + \frac{1}{r}\frac{\partial}{\partial r}\left(r\frac{\partial\overline{v_\theta'^2}}{\partial r}\right) - \frac{2}{r^2}\left(\overline{v_\theta'^2} - \overline{v_r'^2}\right)\right\}, \tag{3.5e}$$

$$P_{v_\theta v_\theta} = \underbrace{-2\overline{u'v_\theta'}\frac{\partial\overline{V_\theta}}{\partial x}}_{P_{v_\theta v_\theta}^{V_\theta,x}}\underbrace{-2\overline{v_r'v_\theta'}\frac{\partial\overline{V_\theta}}{\partial r}}_{P_{v_\theta v_\theta}^{V_\theta,r}}\underbrace{-2\overline{v_r'v_\theta'}\frac{\overline{V_\theta}}{r}}_{P_{v_\theta v_\theta}^{extra}}, \tag{3.5f}$$

$$\epsilon_{v_\theta v_\theta} = -\frac{2}{Re_D}\left\{\overline{\left(\frac{\partial v'_\theta}{\partial x}\right)^2} + \overline{\left(\frac{\partial v'_\theta}{\partial r}\right)^2} + \overline{\frac{1}{r^2}\left(\frac{\partial v'_\theta}{\partial \theta} + v'_r\right)^2}\right\}. \tag{3.5g}$$

Terms of momentum transfer equation for Reynolds normal stress $\overline{v'^2_r}$,

$$C_{v_r v_r} = -\left\{\overline{U}\frac{\partial \overline{v'^2_r}}{\partial x} + \overline{V_r}\frac{\partial \overline{v'^2_r}}{\partial r} - 2\overline{V_\theta}\frac{\overline{v'_r v'_\theta}}{r}\right\}, \tag{3.6a}$$

$$\Pi_{v_r v_r} = 2\,\overline{p'\frac{\partial v'_r}{\partial r}}, \tag{3.6b}$$

$$D^P_{v_r v_r} = -\frac{2}{r}\frac{\partial r\overline{p'v'_r}}{\partial r}, \tag{3.6c}$$

$$D^T_{v_r v_r} = -\frac{\partial \overline{u'v'^2_r}}{\partial x} - \frac{1}{r}\frac{\partial r\overline{v'^3_r}}{\partial r} + 2\frac{\overline{v'_r v'^2_\theta}}{r}, \tag{3.6d}$$

$$D^\nu_{v_r v_r} = \frac{1}{Re_D}\left\{\frac{\partial^2 \overline{v'^2_r}}{\partial x^2} + \frac{1}{r}\frac{\partial}{\partial r}\left(r\frac{\partial \overline{v'^2_r}}{\partial r}\right) + \frac{2}{r^2}\left(\overline{v'^2_\theta} - \overline{v'^2_r}\right)\right\}, \tag{3.6e}$$

$$P_{v_r v_r} = \underbrace{-2\overline{u'v'_r}\frac{\partial \overline{V_r}}{\partial x}}_{P^{V_r,x}_{v_r v_r}} \underbrace{-2\overline{v'^2_r}\frac{\partial \overline{V_r}}{\partial r}}_{P^{V_r,r}_{v_r v_r}} \underbrace{+2\overline{v'_r v'_\theta}\frac{\overline{V_\theta}}{r}}_{P^{extra}_{v_r v_r}}, \tag{3.6f}$$

$$\epsilon_{v_r v_r} = -\frac{2}{Re_D}\left\{\overline{\left(\frac{\partial v'_r}{\partial x}\right)^2} + \overline{\left(\frac{\partial v'_r}{\partial r}\right)^2} + \overline{\frac{1}{r^2}\left(\frac{\partial v'_r}{\partial \theta} - v'_\theta\right)^2}\right\}. \tag{3.6g}$$

At $x = 0.3D$ (see Figure 3.11), the budgets for case Sw18 are significantly higher in magnitude than the budgets for case Sw0. In case Sw0, the production term is only significant in $\overline{u'^2}$ budget compared to that in other Reynolds normal stresses. On the other hand, the swirling case sees the significant increase in production for all the normal stresses. Comparing peaks of P_{uu} for the cases Sw0 and Sw18, the value in swirling case is about 5 times of the value in the non-swirling case. This is reflected in the radial distribution of $\overline{u'^2}$ presented in Figure 3.8(a), where the streamwise component of Reynolds normal stress in case Sw18 is higher than that in case Sw0. The production $P_{v_\theta v_\theta}$ is notably high in the swirling case, which justifies larger $\overline{v'^2_\theta}$ in the region (see Figure 3.8(b)). However, the production of $\overline{v'^2_r}$ in case Sw18 is comparatively smaller than that of other normal stress components and the region $0.5 \leq r/D \leq 0.8$ sees a distinctive negative production of $\overline{v'^2_r}$. As a consequence of this, $\overline{v'^2_r}$ profile in case Sw18 exhibits lower intensity than $\overline{u'^2}$ (see Figure 3.8(a)) and $\overline{v'^2_\theta}$ (see Figure 3.8(b)). The pressure-strain correlation term Π, which is responsible for the redistribution of energy among the stress components, acts as a sink for the stress $\overline{u'^2}$ and a source for $\overline{v'^2_\theta}$ and $\overline{v'^2_r}$ in

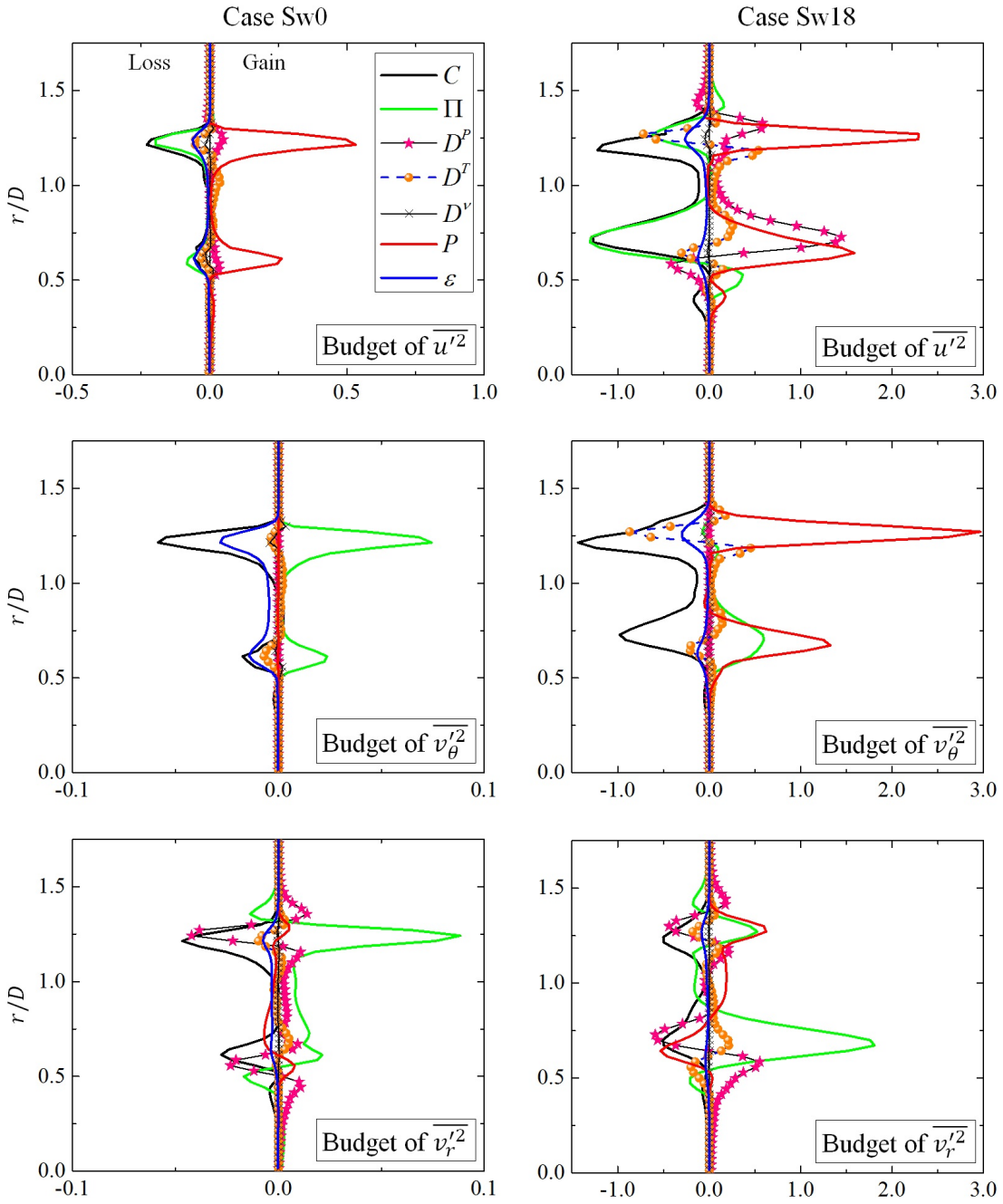

FIGURE 3.11: Budgets of Reynolds normal stresses at location $x = 0.3D$ for cases Sw0 and Sw18.

both cases. However, for case Sw18, the negative production of $\overline{v_r'^2}$ is compensated by higher $\Pi_{v_r v_r}$. As observed in the budgets of TKE (see Figure 3.10), both cases exhibit negative convection. In both cases, the pressure diffusion and turbulent diffusion terms show their presence in all the normal stresses. The dissipation is observed to be smaller for all normal stresses of both the cases.

At the downstream location $x = 1.0D$ (see Figure 3.12), the budget magnitudes are drastically changed for both the cases with the most effect being observed

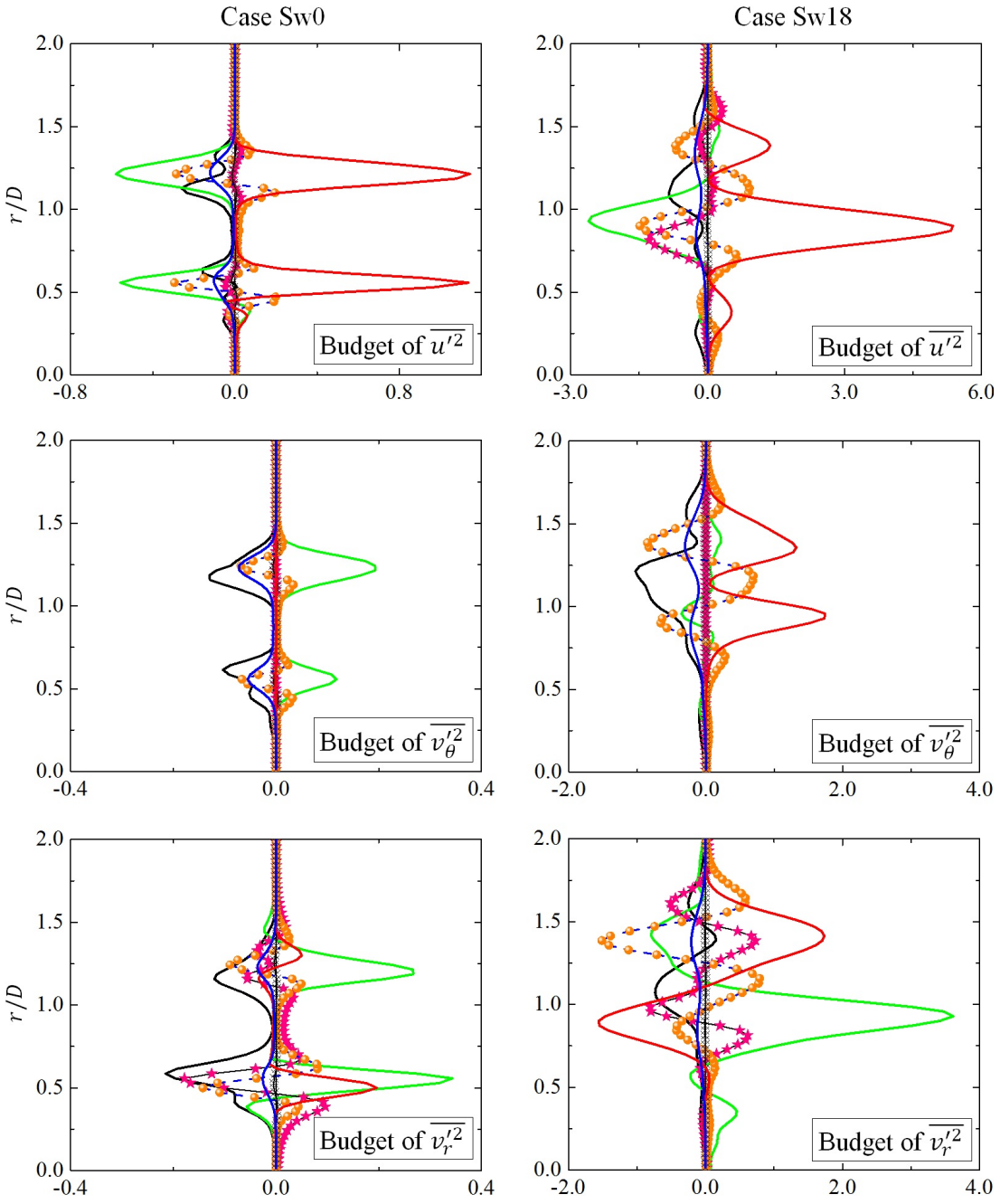

FIGURE 3.12: Budgets of Reynolds normal stresses at location $x = 1.0D$ for cases Sw0 and Sw18. Same legend as Figure 3.11.

in case Sw18. The overall trend in the budgets of case Sw0 is similar to the upstream location, except the turbulent diffusion term which starts to become more dominant for the budgets of all normal stress components. However, the turbulent diffusion term in case Sw0 lacks in transporting the energy from the shear layers to the central region of OJ ($0.7 \leq r/D \leq 1.0$) in contrast to the case Sw18, which sees the positive contribution of the turbulent diffusion term in the central region of OJ ($1.0 \leq r/D \leq 1.3$). For case Sw18, a significant spread is observed in the

budgets, thus broadening the profiles of turbulence intensities (see Figures 3.8(a), 3.8(b) and 3.8(c)). A greater peak is seen at around $r \approx 0.9D$ in the profile of $\overline{u'^2}$ of case Sw18 (see Figure 3.8(a)) which can be justified by the tremendously higher production in the corresponding region. The production of $\overline{v_\theta'^2}$ is negligible for case Sw0 as observed at the upstream location $x = 0.3D$ whereas its two peaks become comparable in the case Sw18 as opposed to the upstream location. The positive contribution of production $P_{v_r v_r}$ is observed in case Sw0, however, a significant negative contribution of $P_{v_r v_r}$ is observed in case Sw18 at the ISL2 ($0.6 \leq r/D \leq 1.2$). The pressure-strain rate correlation term at the OSL ($1.2 \leq r/D \leq 1.6$) of case Sw18 exhibits a noteworthy feature in which it acts as a sink for $\overline{v_r'^2}$, and the minor source for $\overline{u'^2}$ and $\overline{v_\theta'^2}$.

Further downstream at location $x = 3.0D$ (see Figure 3.13), the order of magnitude of budgets of the case Sw18 becomes comparable to that of case Sw0. In non-swirling case, the previously equivalent two production P_{uu} peaks differ in magnitude at this location with the higher production at the OSL ($0.8 \leq r/D \leq 1.7$). This is also reflected in the distribution of the $\overline{u'^2}$ where profile shows a greater peak in the same region (see Figure 3.8(a)). In contrast, the previously greater peak of P_{uu} in case Sw18 at the ISL2 ($r \approx 1.0D$) become equivalent to OSL peak ($r \approx 1.7D$) and is also reflected in the distribution of $\overline{u'^2}$ (see Figure 3.8(a)). Negative convection witnessed at the upstream location is seen to be positive in case Sw18 and can be a reason for increasing stresses in the central region of OJ (around $r/D = 1.5$) (see Figure 3.8). Although the comparatively less activity is seen at the upstream locations in the central region ($r < 0.3D$) in the budgets except for $\overline{u'^2}$ and $\overline{v_r'^2}$ budgets of case Sw18, the terms are observed to be non-negligible in this region at location $x = 3.0D$. The dissipation ϵ becomes one of the dominant terms at this location.

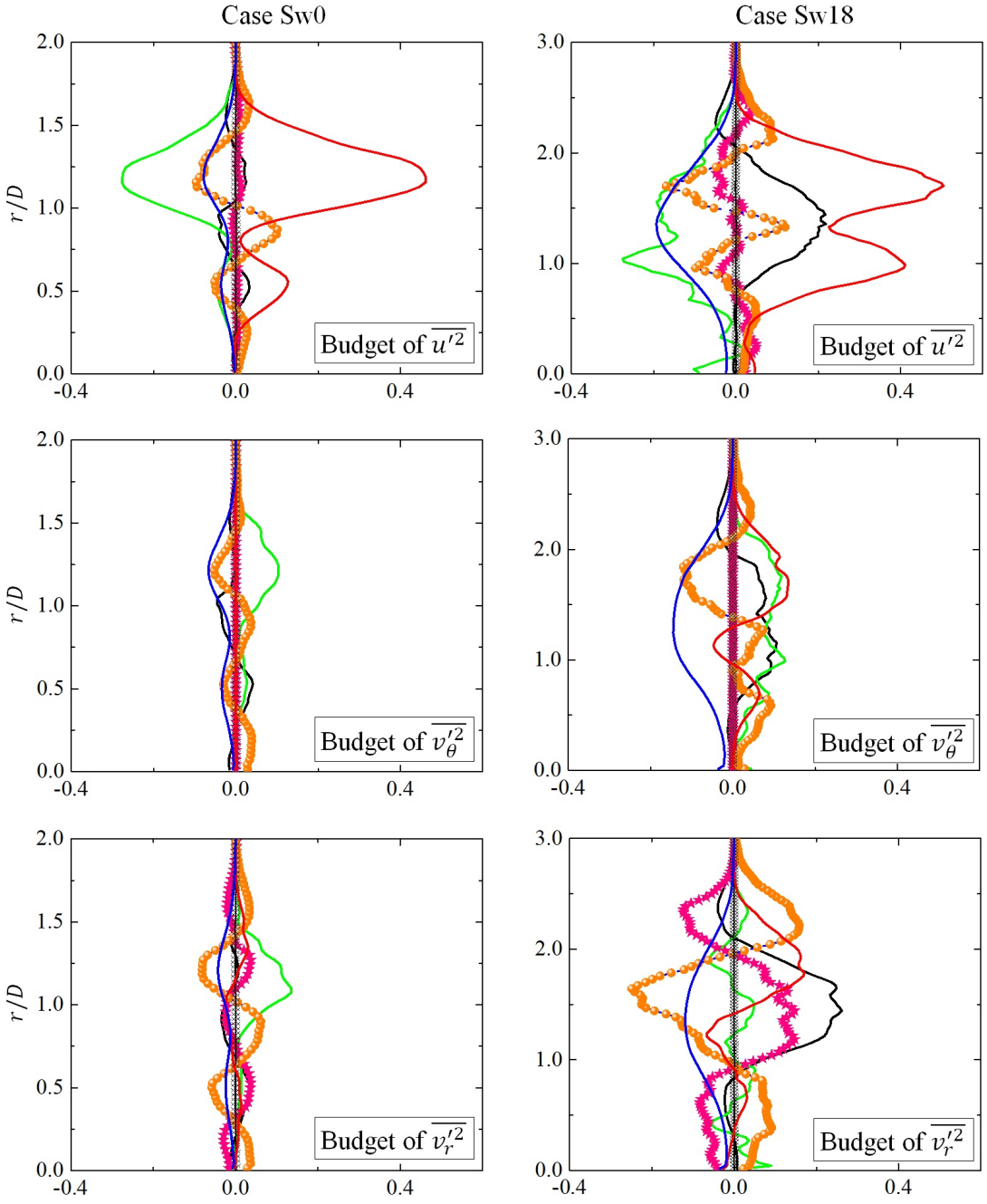

FIGURE 3.13: Budgets of Reynolds normal stresses at location $x = 3.0D$ for cases Sw0 and Sw18. Same legend as Figure 3.11.

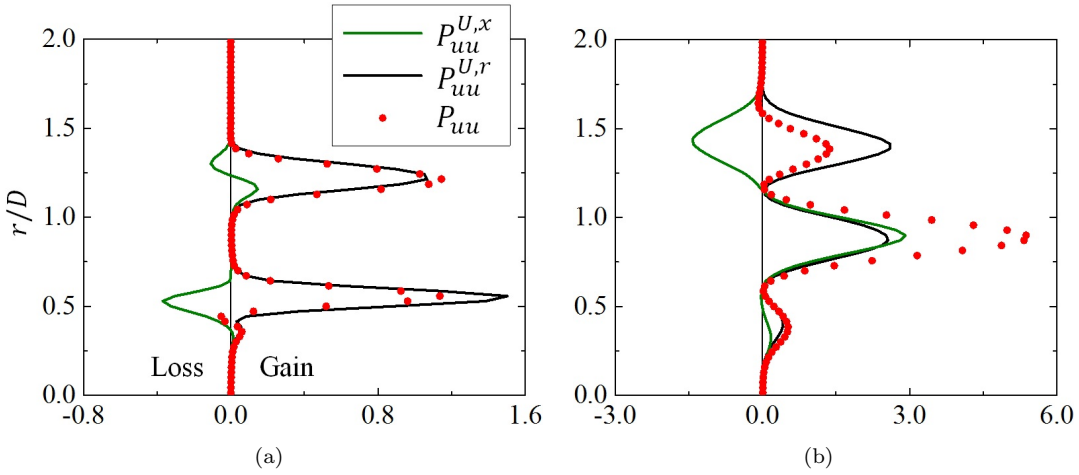

FIGURE 3.14: Production terms of Reynolds stress $\overline{u'^2}$ at location $x = 1.0D$ for cases (a) Sw0, and (b) Sw18.

In order to investigate the cause of higher production in swirling case than the non-swirling case, the contribution of each term in the production of Reynolds normal stresses is demonstrated at the location $x = 1.0D$. Figures 3.14(a) and 3.14(b) demonstrates the production terms of $\overline{u'^2}$ for cases Sw0 and Sw18 respectively. The term $P_{uu}^{U,r}$ is the dominant one with a positive contribution to the production in both the cases. A higher magnitude of $P_{uu}^{U,r}$ in case Sw18 is caused by the higher radial gradient of mean streamwise velocity resulted from the flow reversal between two jets (see Figure 3.4(c)). The least dominant term $P_{uu}^{U,x}$ in the non-swirling case becomes larger in the swirling case. Moreover, the radial outward displacement of the outer peak of mean streamwise velocity due to the centrifugal force along with its narrowed profile results into the sign-change and inflation of $\partial\overline{U}/\partial x$. As a consequence, negative contribution of the term $P_{uu}^{U,x}$ is seen at the OSL ($1.2 \leq r/D \leq 1.8$) for case Sw18, while it adds into the production at ISL2 ($0.6 \leq r/D \leq 1.2$).

Figure 3.15 demonstrates the production terms of $\overline{v_\theta'^2}$ for case Sw18 only since the azimuthal momentum is negligibly small in non-swirling case resulting into the vanished $P_{v_\theta v_\theta}$. Here also the radial gradient term $P_{v_\theta v_\theta}^{V_\theta,r}$ is dominating, whereas the axial gradient term $P_{v_\theta v_\theta}^{V_\theta,x}$ is comparable to the radial gradient term at ISL2 ($0.6 \leq r/D \leq 1.2$). The extra term $P_{v_\theta v_\theta}^{extra}$ also shows its presence.

Production terms of $\overline{v_r'^2}$ are demonstrated in Figures 3.16(a) and 3.16(b) for cases Sw0 and Sw18 respectively. In non-swirling case, the radial gradient term $P_{v_r v_r}^{V_r,r}$ is only seen to be contributing to the production. In swirling case, although the radial gradient term is observed to be dominant, the axial gradient term $P_{v_r v_r}^{V_r,x}$ and extra term $P_{v_r v_r}^{extra}$ also contribute to $P_{v_r v_r}$. Negative production of

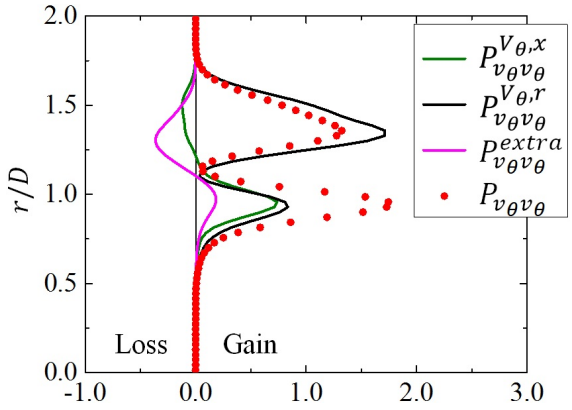

FIGURE 3.15: Production terms of Reynolds stress $\overline{v_\theta'^2}$ at location $x = 1.0D$ for case Sw18.

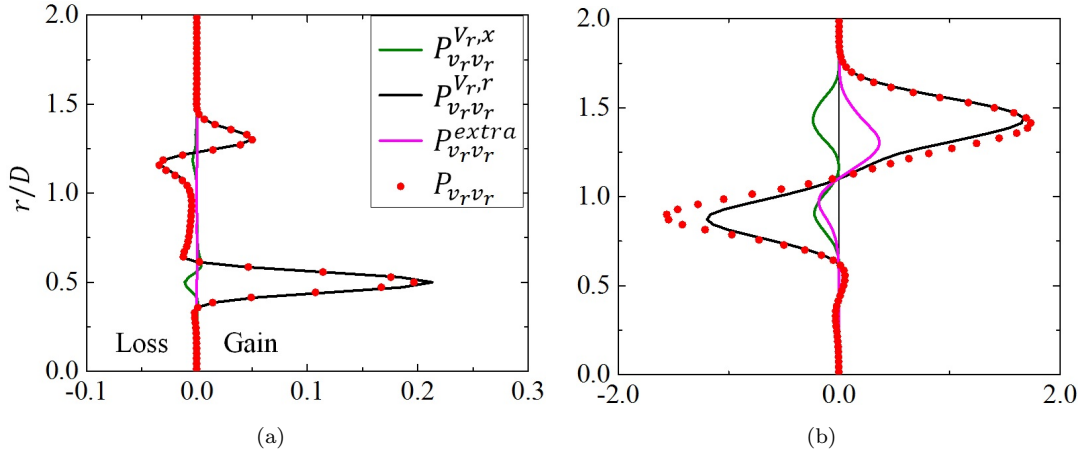

FIGURE 3.16: Production terms of Reynolds stress $\overline{v_r'^2}$ at location $x = 1.0D$ for cases (a) Sw0, and (b) Sw18.

$\overline{v_r'^2}$ observed in the ISL2 ($0.6 \leq r/D \leq 1.2$) is the result of flow divergence due to the swirling motion, which in turn results in the steep radial profiles of $\overline{V_r}$. This causes highly positive and negative radial gradients of $\overline{V_r}$ in the shear layers ISL2 ($0.6 \leq r/D \leq 1.2$) and OSL ($1.2 \leq r/D \leq 1.8$) respectively, which drive the term $P^{V_r,r}_{v_r v_r}$.

3.7 Conclusions

Direct numerical simulations were performed to investigate the coaxial swirling jet with the swirl numbers 0, 0.5, and 1.8. Simulation results exhibited remarkable agreement with the experiment for the non-swirling case, while that for the strongly swirling case were satisfactory. This also demonstrated the usefulness of precursor simulation for the nozzle.

In intermediate swirl case (i.e., case Sw05), a contrasting acceleration after a brief decay in streamwise velocity was observed at the upstream region due to the negative pressure gradient. However, the downstream region exhibited a centerline decay and radial spread of streamwise velocity. The rates of centerline decay and spread of jet were further enhanced with the increment in swirling strength (i.e., case Sw18), which eventually formed the IRZ or partially-penetrated VBB.

Other prime consequences of swirling motion were observed in the Reynolds stresses and TKE, which were seen to be substantially increasing with the swirl. The budgets of TKE and Reynolds normal stresses were investigated for cases Sw0 and Sw18, and the following key observations were made:

- Due to swirl, the turbulent diffusion term in TKE budget became more active in the upstream region (around $x = 1.0D$). This caused the energy level to increase in the central region of OJ of swirling case.
- TKE in the region outside of IRZ was convected from highly energetic upstream region ($x = 0.3D, 1.0D$) to the downstream region ($x = 3.0D$) in the swirling case, whereas the positive contribution by the convection term in non-swirling case seemed to be smaller.
- At $x = 1.0D$, the pressure-strain correlation term acted as energy sink for radial component of Reynolds normal stress at OSL in the swirling case contrary to the non-swirling case.
- The analysis of production terms of Reynolds normal stresses at $x = 1.0D$ (where the great difference is observed between cases Sw0 and Sw18) showed that in addition to the higher production for the streamwise component of normal stress, the significant production was observed for the other components with the introduction of swirl. This was due to the fact that with the introduction of swirl, the terms having streamwise gradient of mean velocity also contributed to the production in addition to the terms with the radial gradient of mean velocity. In the region upstream of central stagnation point (case Sw18), a distinctive negative production at ISL was observed for the radial component of normal stress, which was the consequence of positive radial gradient of mean radial velocity in the region caused by the spreading of jets.

Chapter 4

Passive scalar transport

4.1 Introduction

In addition to the conventional statistics (i.e., RMS scalar fluctuations and turbulent scalar fluxes), numerous measures have been devised for mixing quantification and are used in various studies for different problems. Everson *et al.* (1998) proposed a novel measure to quantify mixing called entropy, which has been used in several recent studies (Ito *et al.* (2018); Tsujimoto *et al.* (2011)) to analyze turbulent jets. However, only the diffusion of scalars can be inferred from entropy and this quantification seems to be insufficient for deriving insights into mixing efficiency when two jet streams are considered. Danckwerts (1952) introduced a segregation parameter based on the correlation between scalar fluctuations normalized by the product of their mean concentrations. It is clear that the sign and magnitude of the segregation parameter indicate mixing characteristics, where positive values correspond to "mixedness" and negative values correspond to "unmixedness". Experimental studies (Tong & Warhaft (1995); Cai *et al.* (2011); Komori *et al.* (1991)) have demonstrated the significance of the segregation parameter. Despite these advances in the analysis of mixing characteristics, the analysis of coaxial swirl jet has not been reported.

Additionally, swirling motion promotes the entrainment of surrounding ambient fluid into the main flow (Komori & Ueda (1985); Park & Shin (1993)). Note that this can be considered as a favorable characteristic for non-premixed confined combustion because the entrained fluid, which is composed of heated products and unburned reactants, will improve combustion efficiency. The effect of ambient

fluid on the statistics of IJ and OJ scalars, which are not found in previous studies, are also required to investigate.

In this chapter, the mixing characteristics is studied for coaxial jet under the influence of swirl introduced in OJ for the three cases Sw0, Sw05, and Sw18. As mentioned earlier in §1.2 that injection of passive scalars through only one of the two jets of coaxial swirling jet limited the investigations aiming the mixing features, simultaneous passive scalars are introduced from each jet to better understand the mixing characteristics. Moreover, the effect of ambient fluid on the statistics of passive scalars is also explored. The §4.2 presents the numerical methodology used for the transport of passive scalars. It is followed by the development of mean scalar fields and the entrained fluid in §4.3. The RMS scalar fluctuations and the turbulent scalar fluxes are presented in the §4.4 and §4.5, respectively. The §4.6 presents the quantification of mixing between two scalars based on entropy and the segregation parameter. In §4.7, the joint probability density functions (JPDFs) between scalars and velocity are illustrated for the leading stagnation point on the centerline of the case Sw18. The conclusion is made in §4.8.

4.2 Numerical method

The equation used for the computation of transport of passive scalars is defined as follows:

$$\frac{\partial \phi_k}{\partial t} + u_j \frac{\partial \phi_k}{\partial x_j} = \frac{1}{Re_D \; Sc_{\phi_k}} \frac{\partial^2 \phi_k}{\partial x_j \partial x_j}. \tag{4.1}$$

Here, $k = 1, 2$, where $k = 1$ for the scalar injected through the IJ and $k = 2$ for the scalar injected through the OJ. Additionally, $Sc_{\phi_k} = \nu / \mathfrak{D}_{\phi_k}$ is the Schmidt number and $\mathfrak{D}_{\phi_k}$ is the mass diffusivity of scalar k.

The transport equation for passive scalars are solved in conjunction with the momentum equations (Equation 2.1), and with the same discretization schemes for the time advancement and spatial differentiation (see §2.1). Passive scalars are not considered in the precursor simulations (presented in §2.2) and are injected with the top-hat profiles at the jet exits. The scalar ϕ_1 is set to one for the IJ and zero for the OJ, while the scalar ϕ_2 is set to one for the OJ and zero for the IJ. The Schmidt numbers for both scalars are set to one. Moreover, the cross-stream boundaries are treated with the Neumann boundary condition and the

convective outflow boundary condition is used for the outlet plane (by equating Θ with ϕ_k in Equation 2.3). Because the inlet conditions and Schmidt numbers for the scalars are of unit magnitude, ϕ_1 represents the mass fraction of the IJ fluid and ϕ_2 represents the mass fraction of the OJ fluid. The domain initially contains only stationary ambient fluid (i.e., the ϕ_A value representing the mass fraction of the ambient fluid is initially equal to one). Note that the transport equation for ϕ_A is not solved explicitly because the equation $\phi_1 + \phi_2 + \phi_A = 1$ holds true at any given location in the domain to conserve mass and ϕ_A can be estimated using this equation. The statistical data from the main simulations are 972, 480, and 556.8 time scales D/U_{IJ} for cases Sw0, Sw05, and Sw18 respectively. These values are sufficient to derive statistically reliable results.

4.3 Mean scalar fields

Figure 4.1 presents the contour maps of mean IJ scalar $\overline{\phi_1}$ at the central cross-section for the three test cases. Case Sw0, which is presented in Figure 4.1(a), exhibits an outward radial spread with a very slow rate downstream of the streamwise location $1.0D$, followed by centerline decay from $x = 2.0D$. Similarly, case Sw05, which is presented in Figure 4.1(b), exhibits a slower spreading rate in the upstream region ($x \leq 4.0D$). However, the centerline decay is slower in case Sw05 compared to that in case Sw0 in the upstream region $x \leq 4.0D$, which is undesirable for mixing. This may be a result of the flow acceleration in the region $1.0 \leq x/D \leq 2.0$ in case Sw05 (see Figures 3.4(b) and 3.6), resulting in the advection of the scalar $\overline{\phi_1}$ to the downstream region at a greater rate. Regardless, the spreading rate is enhanced in the downstream region $x > 4.0D$ based on the greater spread of the jet. A drastically enhanced rate of spread and centerline decay can be observed for case Sw18 in Figure 4.1(c). This phenomenon is essentially prompted by the IRZ. The central recirculating flow acts as a barrier to the IJ scalar and the annular reversed flow combined with the radially outward directing flow advects the scalar beyond the radial extent of $0.5D$. The magnitude of $\overline{\phi_1}$ is less than 0.2 in the downstream region $x > 4.0D$.

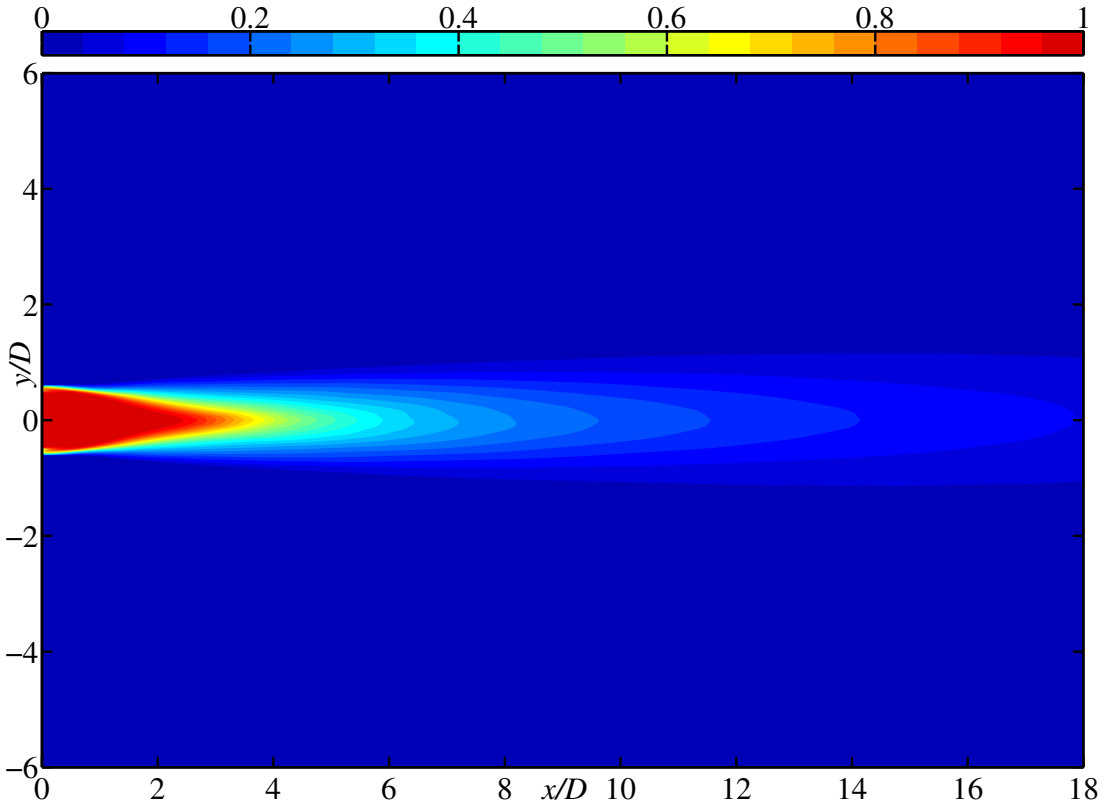
0
0.2
0.4
0.6
0.8
1
6
4
2
0
−2
−4
−6
y/D
0
2
4
6
8
x/D
10
12
14
16
18

(a)

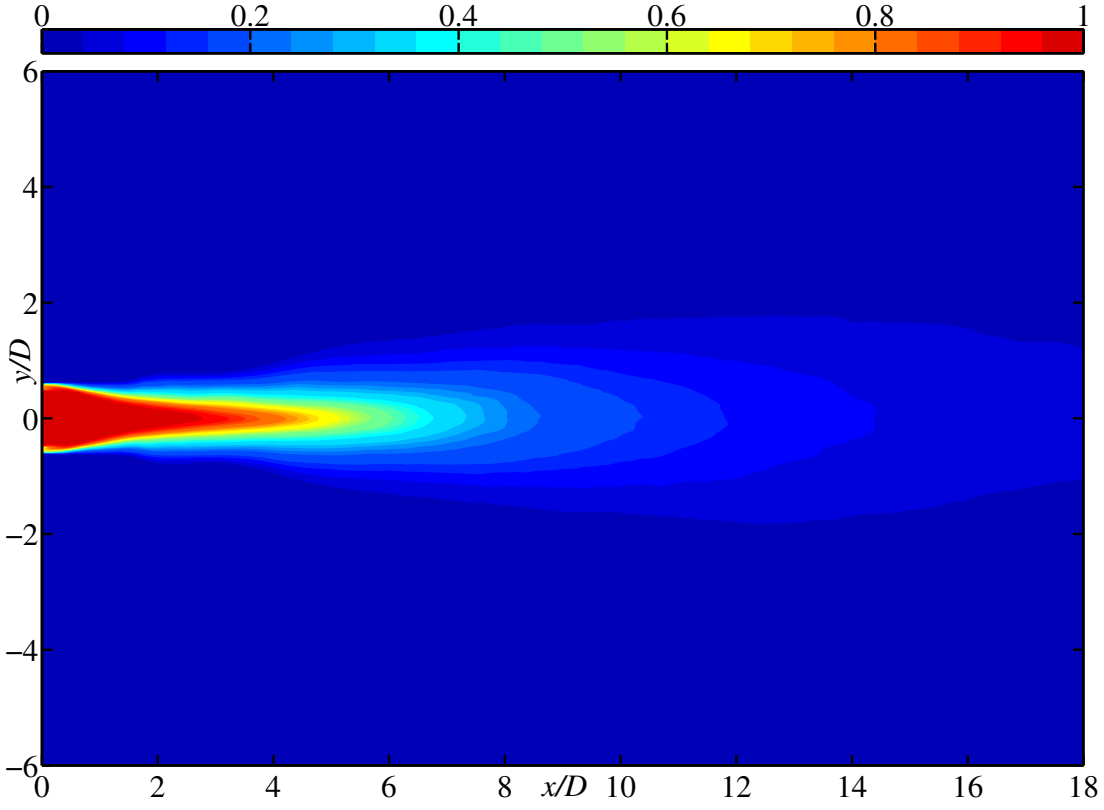
0
0.2
0.4
0.6
0.8
1
6
4
2
0
−2
−4
−6
y/D
0
2
4
6
8
x/D
10
12
14
16
18

(b)

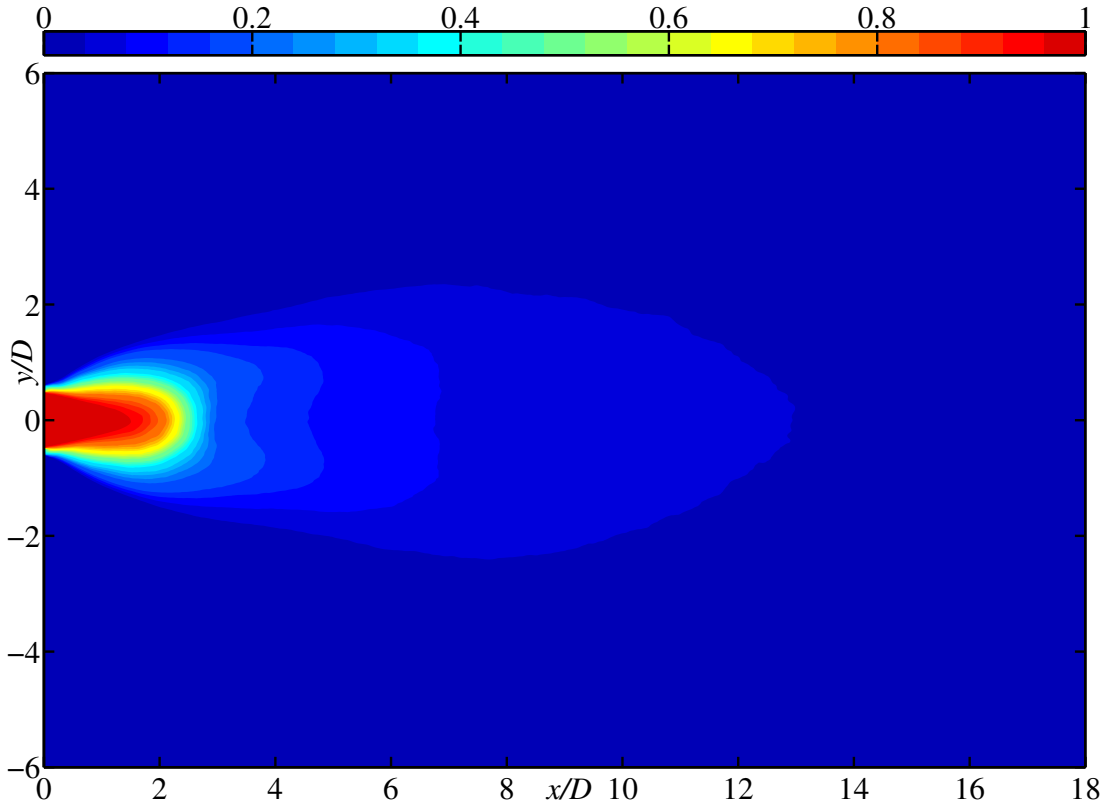

(c)

FIGURE 4.1: Contour maps of the mean IJ scalar $\overline{\phi_1}$ for cases (a) Sw0, (b) Sw05, and (c) Sw18.

Figure 4.2 presents the contour maps of the mean OJ scalar $\overline{\phi_2}$. The contour maps for case Sw0, which are presented in Figure 4.2(a), exhibit a monotonous spread in both radial directions and the centerline magnitude exceeds 0.4 for locations of $x > 4.0D$ prior to reaching a maximum value in the region around the location $x = 9.0D$. The obvious centerline decay caused by this spread can be observed at farther downstream region. Figure 4.2(b) reveals that it takes an extra $1.0D$ for case Sw05 compared to case Sw0 to exceed a magnitude of 0.4 at the centerline. The downstream region ($x > 4.0D$) in case Sw05 exhibits radial outward spread at a greater rate than that in case Sw0. Compared to the other cases, the OJ scalar in case Sw18, which is presented in Figure 4.2(c), reaches the centerline earlier and exceeds the magnitude of 0.4 just downstream of the stagnation point, which is located at $x = 2.5D$. The IRZ formed in the region $2.5 \leq x/D \leq 8.1$ is responsible for advection of the OJ scalar toward the axis and upstream. Greater radial outward spread can also be observed.

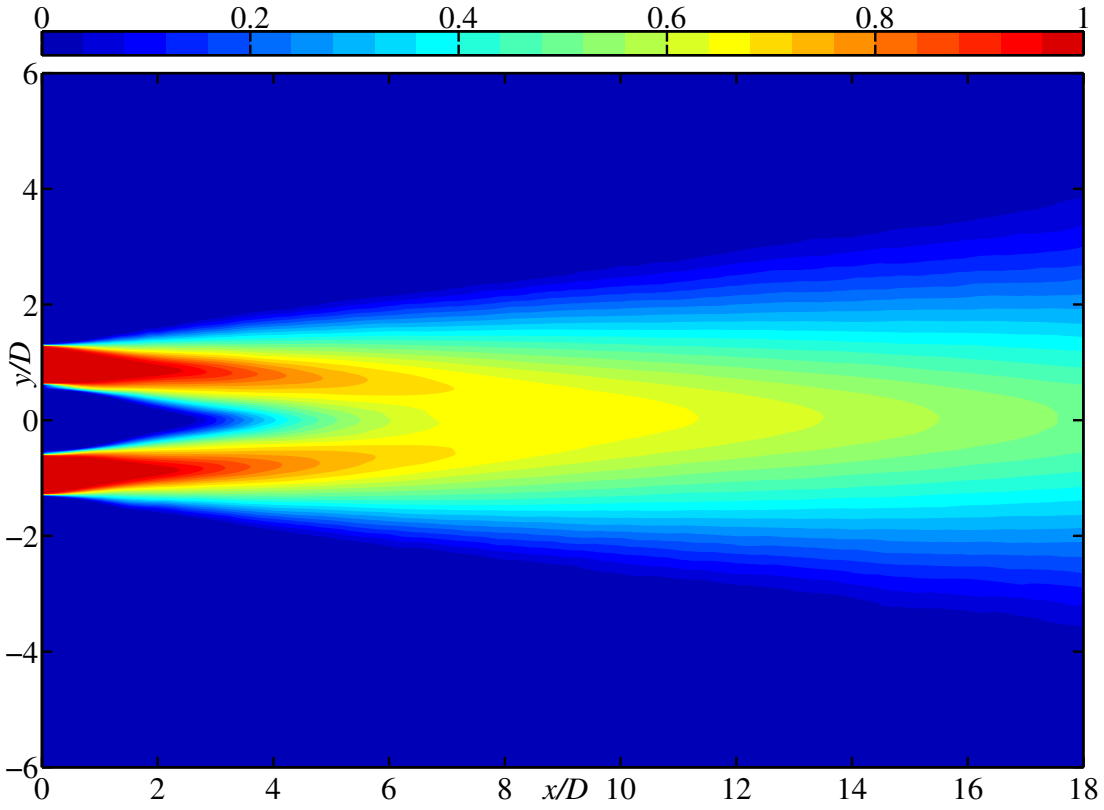
0
0.2
0.4
0.6
0.8
1
6
4
2
0
−2
−4
−6
y/D
0
2
4
6
8
x/D
10
12
14
16
18

(a)

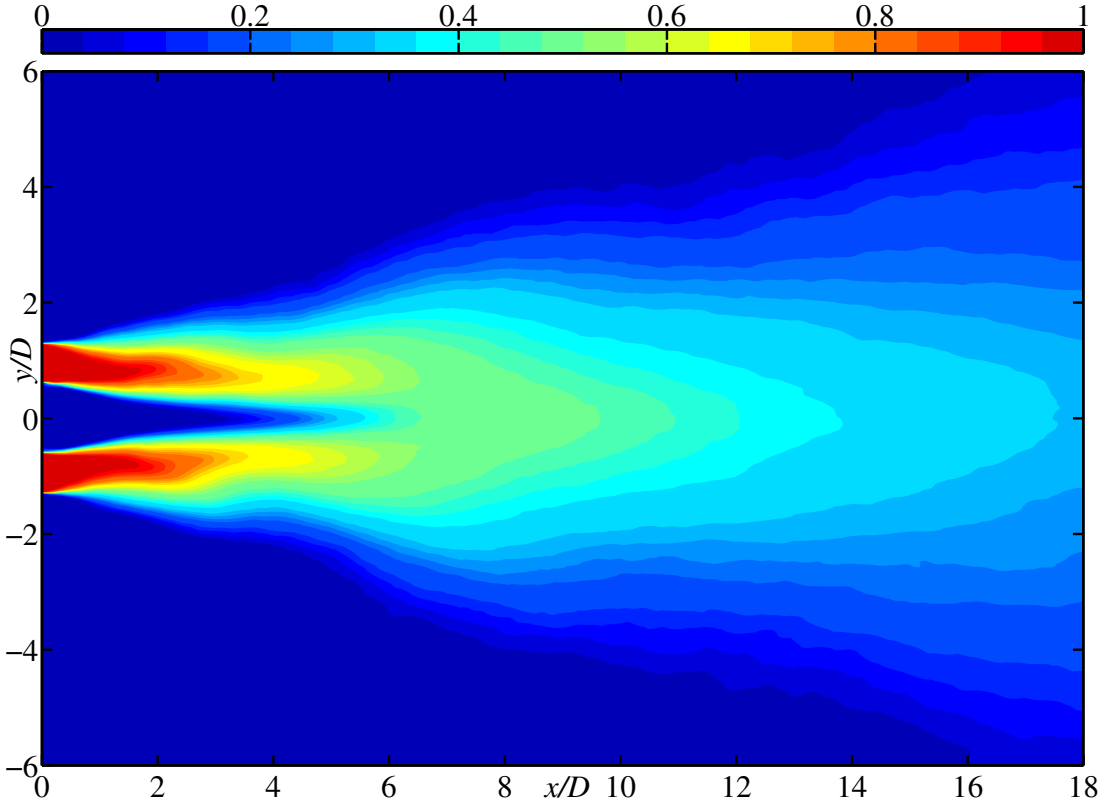
0
0.2
0.4
0.6
0.8
1
6
4
2
0
−2
−4
−6
y/D
0
2
4
6
8
x/D
10
12
14
16
18

(b)

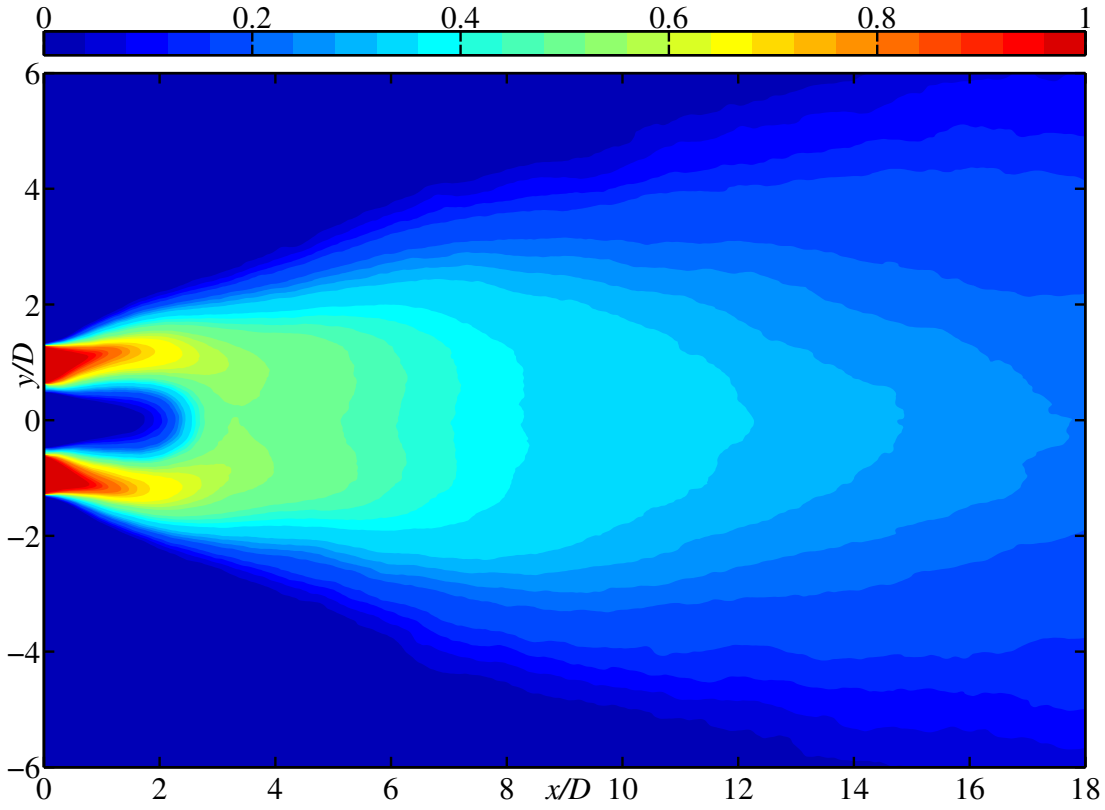

(c)

FIGURE 4.2: Contour maps of the mean OJ scalar $\overline{\phi_2}$ for cases (a) Sw0, (b) Sw05, and (c) Sw18.

The mean scalar distributions demonstrate that case Sw05 exhibits an undesirable spread of both scalars in the upstream region ($x < 4.0D$), unlike case Sw0, further delaying mixing between the two scalars. However, it exhibits improved spread in the downstream region. In contrast, case Sw18 is only preferable for the mixing of scalars immediately downstream of jet the exits. However, this phenomenon can only be confirmed through further investigation, which is presented in §4.6.

The entrainment rate Ψ is calculated as $(Q - Q_{x_0})/Q_{x_0}$ and its streamwise variation is presented in Figure 4.3. Here, Q is the total flow rate through a cross section and is calculated as $Q = \iint \overline{U} dydz$, and Q_{x_0} is the flow rate at the nozzle exit plane. The entrainment rate represents the ratio between the amount of ambient fluid entrained and the amount of fluid injected through the nozzles. This rate increases constantly in the streamwise direction for case Sw0 whereas its slope increases with the increase in swirl number. This observation of increase in entrainment rate with the swirl number is consistent with Komori & Ueda (1985); Park & Shin (1993). The mean amount of entrained ambient fluid $\overline{\phi_A}$ at a location

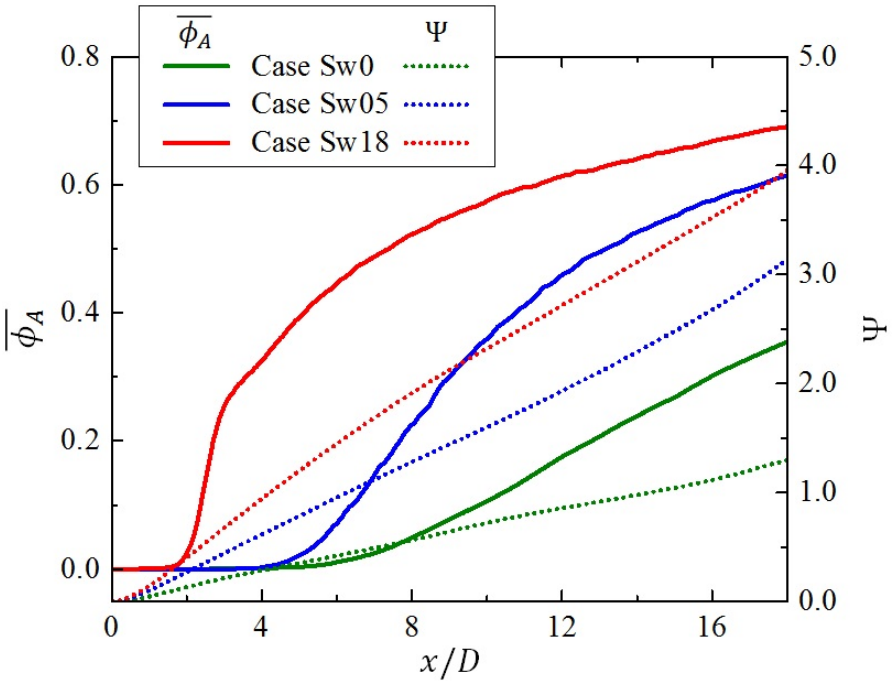

FIGURE 4.3: Centerline distribution of the mean ambient fluid and variation in the entrainment rate in the streamwise direction. Solid lines: $\overline{\phi_A}$, and dotted lines: Ψ.

can be estimated as $1 - \overline{\phi_1} - \overline{\phi_2}$. Figure 4.3 presents the mean ambient fluid at the centerline. The entrained ambient fluid reaches the centerline at $x \approx 4.0D$ for cases Sw0 and Sw05. However, its volume in the latter case increases in the streamwise direction compared to the former case based on the higher entrainment rate in case Sw05. In contrast, the entrained ambient fluid in case Sw18 reaches the centerline at far upstream location of $x < 2.0D$, which is upstream of the stagnation point. This is the combined effect of a higher entrainment rate and IRZ. The amount of entrained fluid at the centerline is always higher for case Sw18 than for the other two cases.

4.4 RMS fluctuations of scalars

Figure 4.4 compares the centerline distributions of RMS fluctuations of both scalars for all three test cases. Here, σ_1 and σ_2 are the RMS fluctuations of the IJ and OJ scalars, respectively, which are calculated as $\sigma_1 = (\overline{\phi_1'^2})^{1/2}$ and $\sigma_2 = (\overline{\phi_2'^2})^{1/2}$, respectively. The profiles for case Sw0 show insignificant fluctuations for both scalars of $x < 2.0D$, indicating that the OJ scalar ϕ_2 did not reach the centerline. In other words, there is no mixing between the scalars. The RMS fluctuations for the scalars continue to increase thereafter prior to reaching to

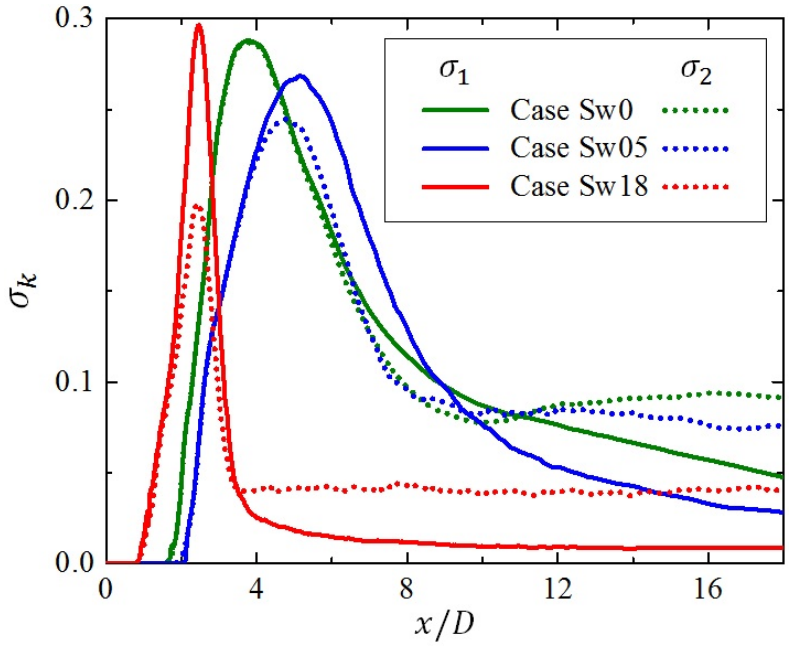

FIGURE 4.4: Centerline distribution of RMS fluctuations of the IJ scalar (σ_1) and OJ scalar (σ_2). Solid lines: σ_1, and dotted lines: σ_2.

a peak value of ≈ 0.28 at $x \approx 4.0D$. The equality between σ_1 and σ_2 can be attributed to the absence of entrained fluid, which is explained mathematically in Appendix A. In the downstream region, the profiles exhibit a decline, and σ_1 and σ_2 begin to differ from each other. This phenomenon is a result of the entrainment of ambient fluid. However, the OJ scalar fluctuation σ_2 increases slightly in the downstream region. The trends in RMS fluctuations in case Sw05 are similar to those in case Sw0, except that the peak fluctuations are located farther downstream with the peak of σ_2 being smaller than the σ_1 peak and the differentiation of profiles of σ_1 and σ_2 initiates earlier compared to case Sw0. The non-zero RMS fluctuations at $x \approx 1.1D$ in case Sw18 confirm that the OJ scalar reaches the centerline earlier compared to the other two cases. Similar to case Sw05, the peak of σ_2 in case Sw18 is smaller than that of σ_1, but the difference is greater in case Sw18 based on its higher entrainment rate. Note that the peaks in case Sw18 are farther upstream than in the other two cases and are located close to the leading stagnation point ($x = 2.5D$). The fluctuation σ_2 exhibits a greater magnitude than σ_1 in the downstream region in case Sw18, similar to the other two cases, starting from $x \approx 3.5D$.

The radial profiles of the RMS fluctuations of the scalars at six downstream locations are compared for the three test cases in Figure 4.5. The RMS fluctuations of the IJ scalar σ_1 in Figure 4.5(a) indicate that at the cross-section $x = 0.3D$, there is only a single peak for all three cases at approximately $0.5 \leq r/D \leq 0.6$

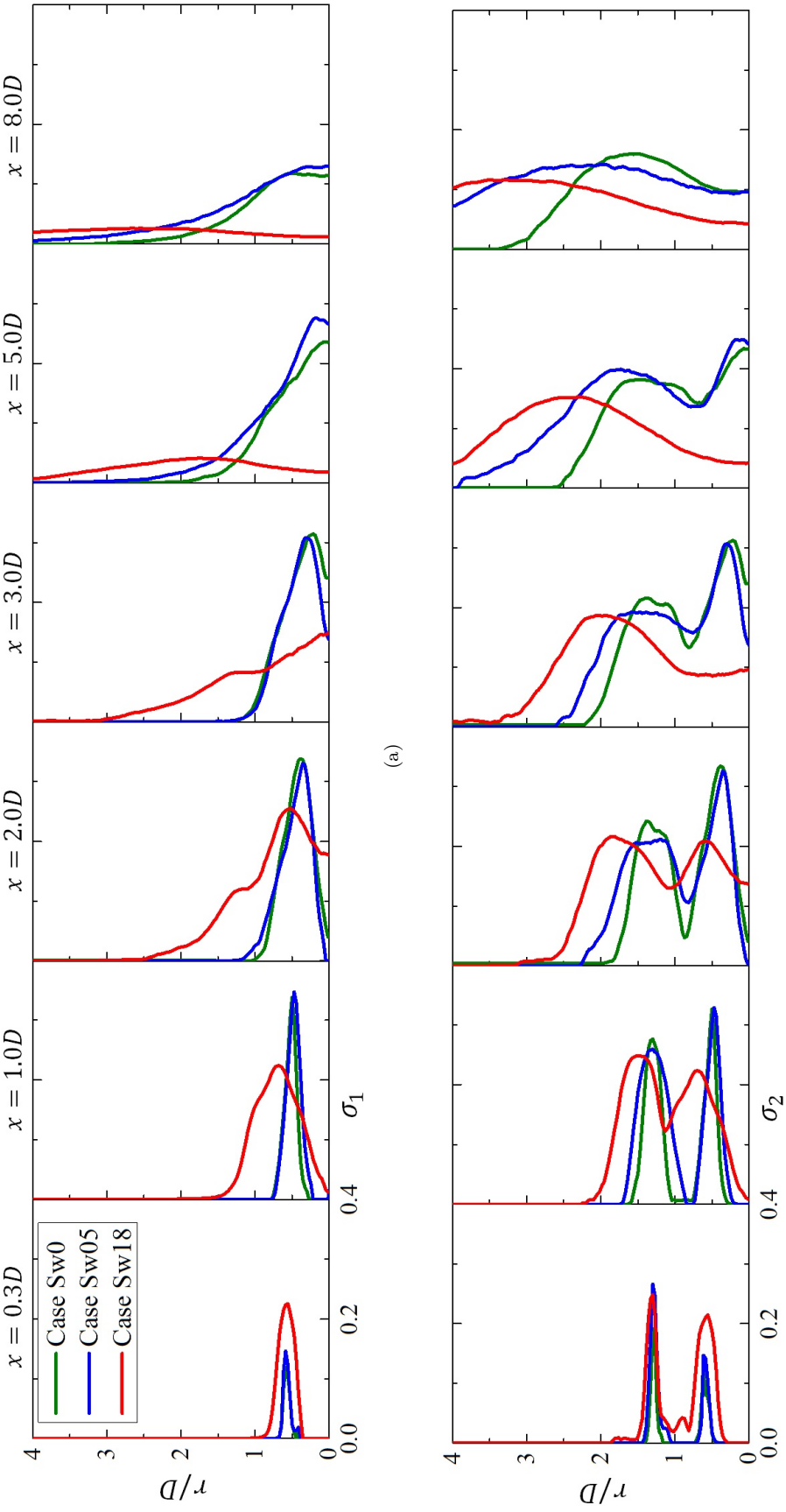

FIGURE 4.5: Radial distributions of the RMS fluctuations of the (a) IJ scalar and (b) OJ scalar.

(i.e., in the ISL). However, the profile for case Sw18 exhibits higher peaks and a greater spread. At $x = 1.0D$, the peak values in cases Sw0 and Sw05 increase with a slight broadening of profiles, whereas the profile spans over a much larger radial area in case Sw18 with unchanged peak value. In the downstream region, the profiles continue to show similarities between cases Sw0 and Sw05, and the peak positions in these cases move toward the centerline. The fluctuations in case Sw18 show remarkable decay and a nearly flat profile at $x = 5.0D$. However, it should be noted that $\overline{\phi_1}$ also decays by that point (see Figure 4.1(c)). Roback & Johnson (1983) reported similar development for σ_1 compared to that in case Sw18. The other two cases exhibit fluctuation decay in the downstream region with a slower rate. Figure 4.5(b) shows that the OJ RMS scalar fluctuations σ_2 exhibit two distinct peaks for $x < 8.0D$ for cases Sw0 and Sw05, and $x < 3.0D$ for case Sw18. One peak lies at the ISL between the two jets and the other lies at the OSL between the OJ and ambient fluid. Although the radial location of the inner peak is consistent with the single peak of σ_1 in all three test cases, the magnitude of the peak seems to be affected at the downstream locations of $x \geq 5.0D$ for case Sw05 and $x \geq 2.0D$ for case Sw18 based on the entrainment of ambient fluid. At downstream locations fo $x > 2.0D$, the higher rate of jet spread in case Sw05 causes the outer peak to move radially outward compared to case Sw0, whereas case Sw18 exhibits this tendency only in the upstream region.

4.5 Turbulent scalar fluxes

Figure 4.6 presents the radial distributions of the turbulent fluxes of the IJ scalar ϕ_1 at six downstream locations. Cases Sw0 and Sw05 exhibit a similar trend of $\overline{u'\phi_1'}$ with a less significant inner positive peak and an outer negative peak in ISL. In addition to the increased magnitude of the negative peak, enhanced positive streamwise flux of the IJ scalar can be observed in case Sw18. This is caused by enhanced production as a result of the steeper streamwise and radial gradients of the mean variables because of the IRZ. The positive peak moves toward the centerline and continues to increase in strength until reaching the leading stagnation point of the IRZ. The positive and negative peaks of $\overline{u'\phi_1'}$ can be explained based on its production as

$$P_{u\phi_1} \cong \underbrace{-\overline{u'\phi_1'}\frac{\partial \overline{U}}{\partial x}}_{P_{u\phi_1}^{U,x}} \underbrace{-\overline{v_r'\phi_1'}\frac{\partial \overline{U}}{\partial r}}_{P_{u\phi_1}^{U,r}} \underbrace{-\overline{u'^2}\frac{\partial \overline{\phi_1}}{\partial x}}_{P_{u\phi_1}^{\phi_1,x}} \underbrace{-\overline{u'v_r'}\frac{\partial \overline{\phi_1}}{\partial r}}_{P_{u\phi_1}^{\phi_1,r}}. \tag{4.2}$$

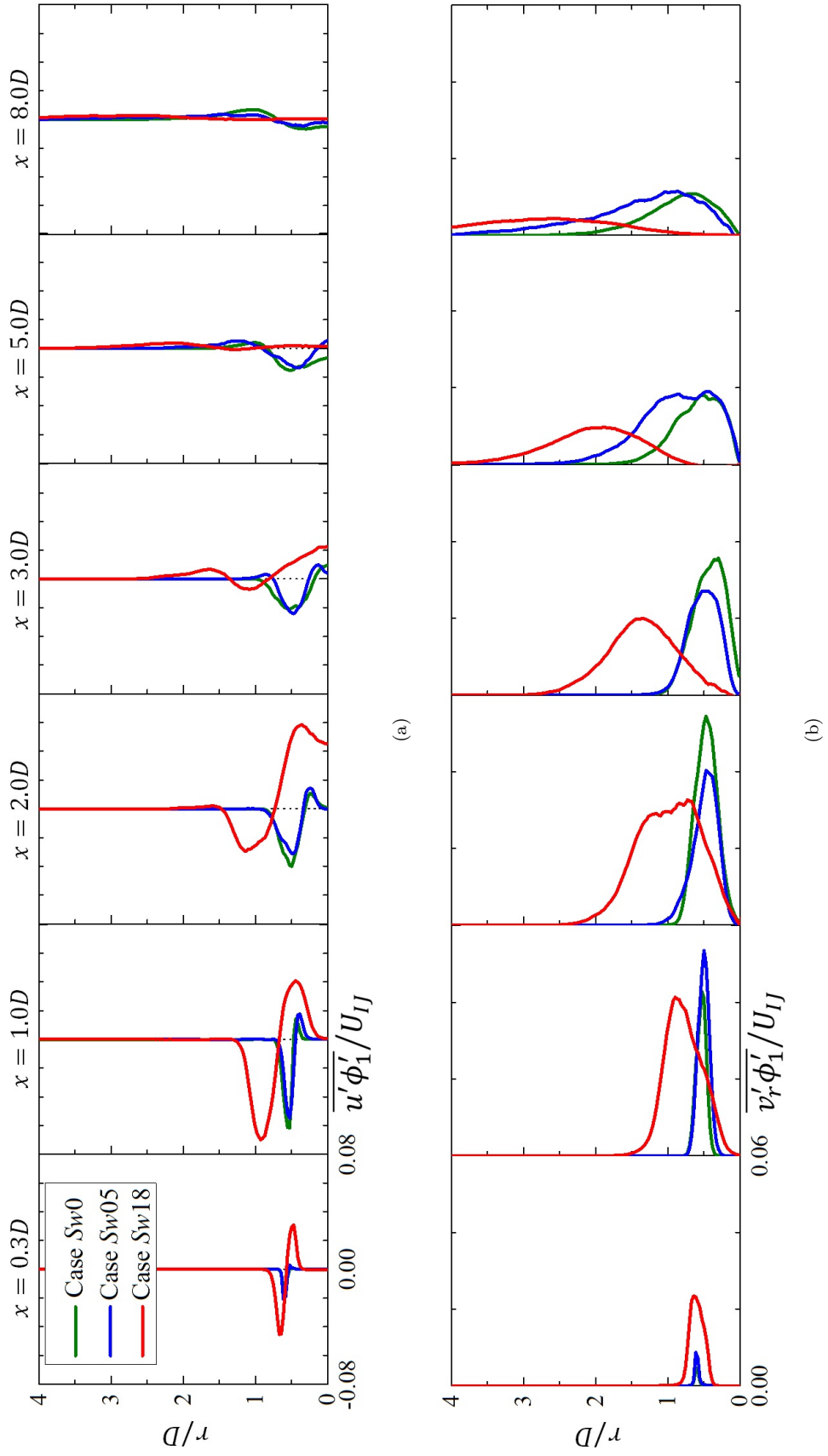
x = 0.3D
x = 1.0D
x = 2.0D
x = 3.0D
x = 5.0D
x = 8.0D
Case Sw0
Case Sw05
Case Sw18
r/D
$\overline{u'\phi_1'}/U_{IJ}$
$\overline{v_r'\phi_1'}/U_{IJ}$
(a)
(b)

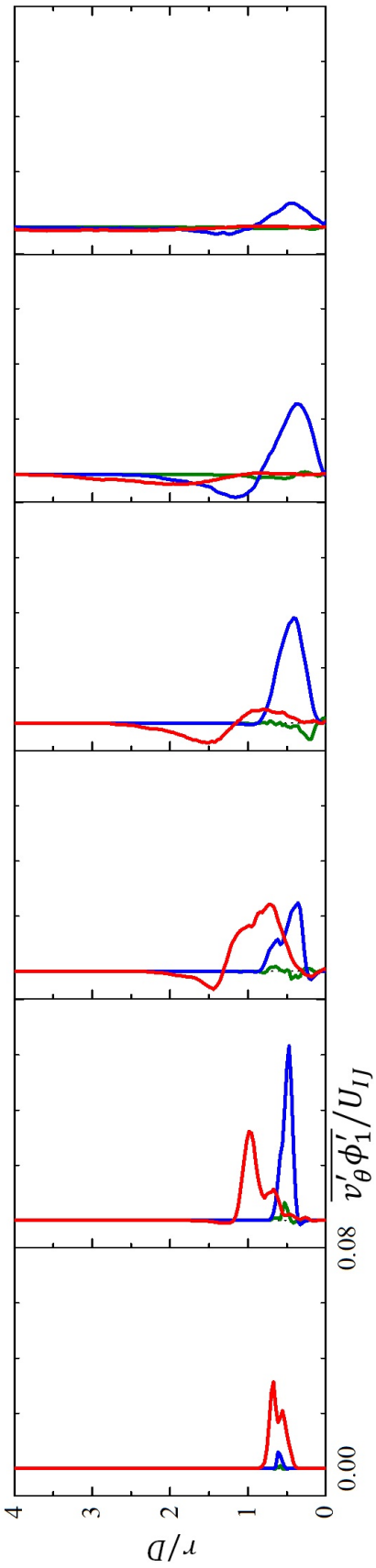

FIGURE 4.6: Radial distributions of the turbulent fluxes of the IJ scalar in the (a) streamwise direction, (b) radial direction, and (c) azimuthal direction.

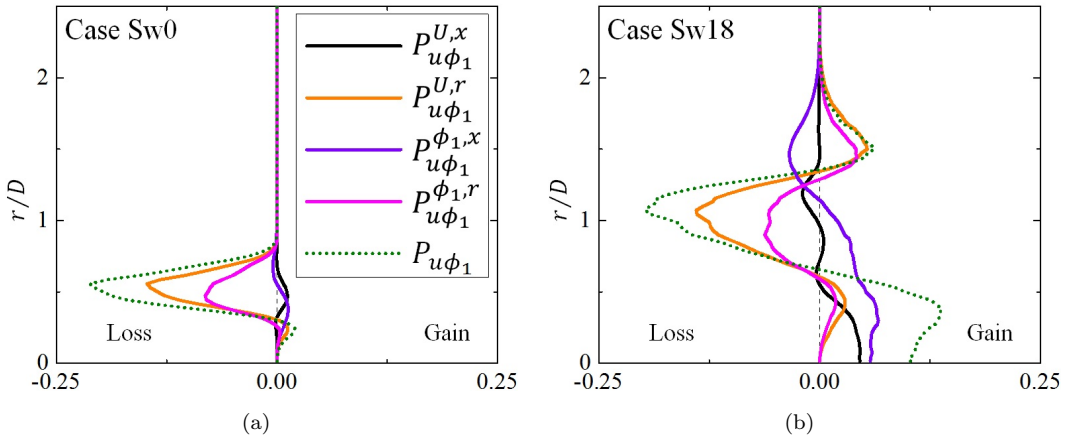

FIGURE 4.7: Production terms for turbulent streamwise flux of the IJ scalar $\overline{u'\phi'_1}$ at a downstream location of $x = 2.0D$ for cases Sw0 and Sw18.

Figure 4.7 presents the radial distribution of the production $P_{u\phi_1}$ and its terms for cases Sw0 and Sw18 (case Sw05 is not presented because it exhibits a similar trend of $\overline{u'\phi'_1}$ compared to case Sw0) at a downstream location of $x = 2.0D$. The high positive value of $\overline{u'\phi'_1}$ in the central region $r < 0.7D$ in case Sw18 (see Figure 4.6(a)) can be attributed to the production gain in this region. An analysis of terms suggests that this primarily occurs as a result of the terms involving the axial gradients of the mean streamwise velocity and mean IJ scalar. In contrast, case Sw0 exhibits negligible production in the central region $r \leq 0.3D$ based on the absence of any significant axial or radial gradients of mean flow quantities. Negative production $P_{u\phi_1}$ in both cases can be observed in the outer regions ($0.3D < r \leq 0.9D$ for case Sw0 and $0.7D \leq r \leq 1.3D$ for case Sw18), resulting in a negative value of $\overline{u'\phi'_1}$. The terms with radial gradients for the mean streamwise velocity and mean IJ scalar are responsible for the negative production in cases Sw0 and Sw18. The turbulent streamwise flux (see Figure 4.6(a)) becomes negligible at $x = 5.0D$ for case Sw18 and $x = 8.0D$ for the other two cases. The profiles of turbulent radial flux $\overline{v'_r\phi'_1}$ exhibit a single peak for all three cases. The peak magnitudes at $x = 2.0D$ and $x = 3.0D$ are higher for case Sw0 than for case Sw05. However, the magnitude of peaks in the downstream region are consistent and the spread is greater for the profile in case Sw05. Case Sw18 shows a smaller peak, but with substantial radial spread. The turbulent azimuthal flux $\overline{v'_\theta\phi'_1}$ is negligible for case Sw0 (see Figure 4.6(c)). The production of $\overline{v'_\theta\phi'_1}$ can be expressed as

$$P_{v_\theta\phi_1} \cong -\overline{u'\phi'_1}\frac{\partial\overline{V_\theta}}{\partial x} - \overline{v'_r\phi'_1}\frac{\partial\overline{V_\theta}}{\partial r} - \overline{u'v'_\theta}\frac{\partial\overline{\phi_1}}{\partial x} - \overline{v'_r v'_\theta}\frac{\partial\overline{\phi_1}}{\partial r}. \tag{4.3}$$

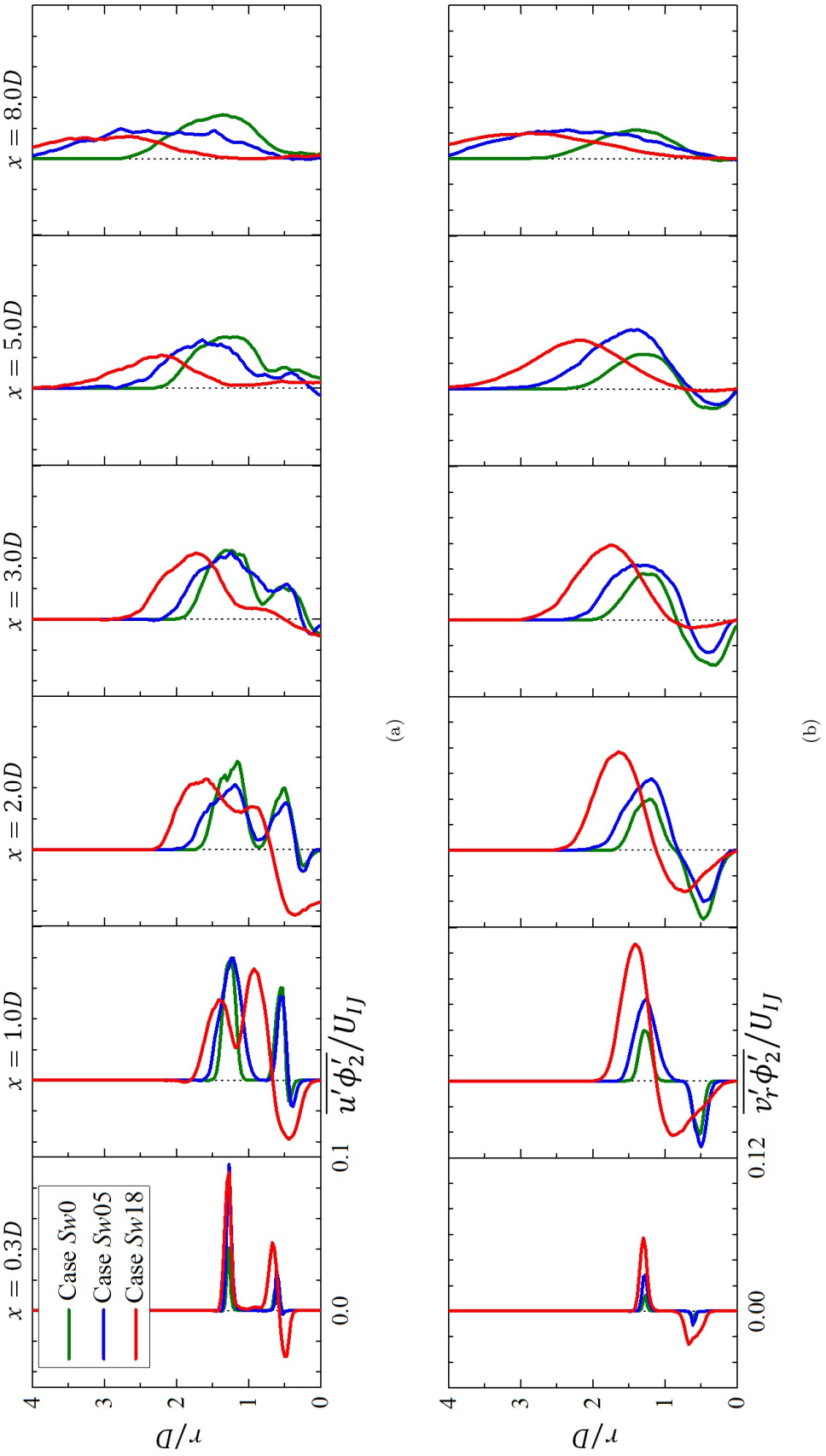
x = 0.3D
x = 1.0D
x = 2.0D
x = 3.0D
x = 5.0D
x = 8.0D
Case Sw0
Case Sw05
Case Sw18
0.0
0.1
0.00
0.12
r/D
(a)
(b)

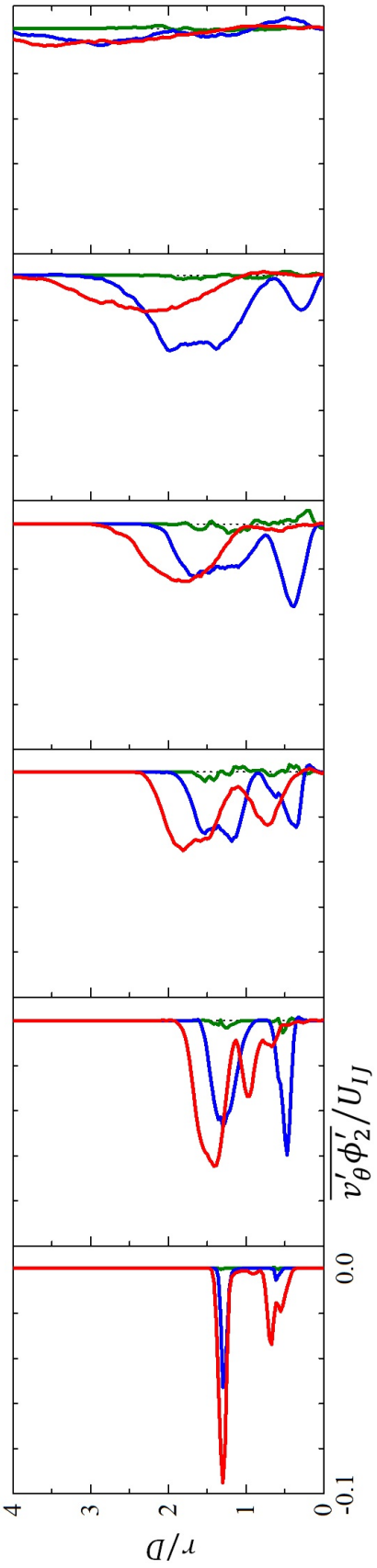

FIGURE 4.8: Radial distributions of the turbulent fluxes of the OJ scalar in the (a) streamwise direction, (b) radial direction, and (c) azimuthal direction.

The absence of any azimuthal momentum and the negligible shear stresses $\overline{u'v'_\theta}$ and $\overline{v'_r v'_\theta}$ in case Sw0 (see Figures 3.9(b),(c)) lead to negligible production, which dictates that $\overline{v'_\theta \phi'_1}$. In contrast, the swirling cases exhibit significant azimuthal momentum and secondary shear stresses, which lead to the production of flux $\overline{v'_\theta \phi'_1}$. This phenomenon contributes to mixing enhancement in the swirling cases.

The radial distribution of the turbulent fluxes of the OJ scalar ϕ_2 are presented in Figure 4.8. The flux $\overline{u'\phi'_2}$ exhibits a similar distribution for cases Sw0 and Sw05 with two significant positive peaks. Case Sw18 exhibits a strong upstream flux of ϕ_2, especially in the region close to the leading stagnation point. As expected, the radial distribution of $\overline{v'_r \phi'_2}$ exhibits radial inward and outward flux of the OJ scalar in all three test cases. The radial inward flux, which is of particular interest when considering the mixing of ϕ_2 with ϕ_1, is slightly higher in case Sw0 at locations of $x = 2.0D$ and $x = 3.0D$ when compared to case Sw05. This factor combined with the comparatively lower $\overline{v'_r \phi'_1}$ (see Figure 4.6(b)) indicates poor mixing characteristics in this region for case Sw05 compared to case Sw0. Similar to the IJ scalar, the azimuthal flux is negligible in case Sw0 for the OJ scalar. The swirling cases exhibit a stronger flux of $\overline{v'_\theta \phi'_2}$.

4.6 Mixing quantification

This section discusses the quantification of mixing between two scalars based on entropy and the segregation parameter. The advantage of injecting separate scalars from each jet at a time can be noticed in the later quantifications.

4.6.1 Entropy

Simply put, entropy (Everson *et al.* (1998)) measures the probabilities of different arrangements of scalar scattering occurring over a target area. Therefore, entropy represents the diffusion of scalars. Entropy is formulated as follows:

$$S_k = k_B \, \Phi_k \, \ln \Phi_k - k_B \iint \overline{\phi_k} \, \ln \overline{\phi_k} \, dydz, \tag{4.4}$$

where k_B is the Boltzmann constant, which is assumed to be equal to one, and $\Phi_k = \iint \overline{\phi_k} \, dydz$. The integrations in Φ_k and the second term of S_k are applied over the entire cross-section (i.e., $y - z$ plane). The first term in this formulation represents statistical entropy (S_{sta_k}) and the second term represents fluctuation

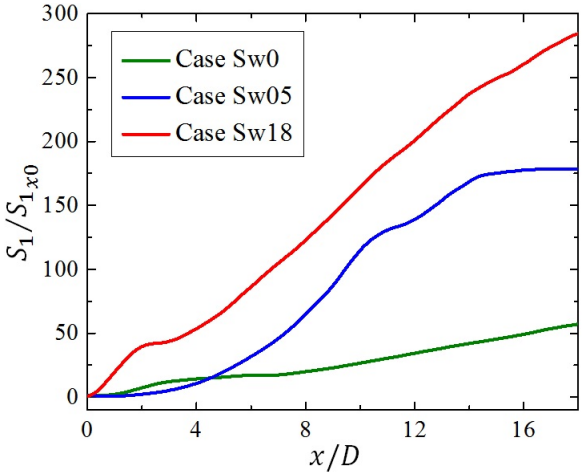

(a)

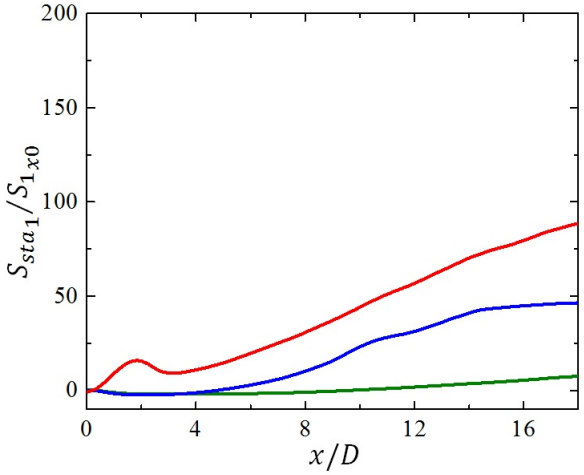

(b)

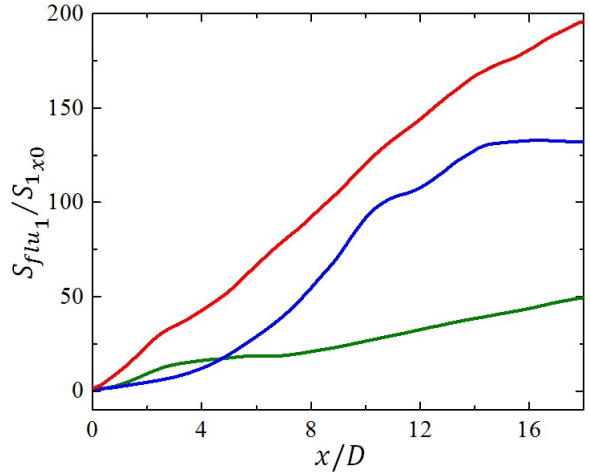

(c)

FIGURE 4.9: Axial variation of (a) total entropy, (b) statistical entropy, and (c) fluctuation entropy for an IJ scalar. Profiles are normalized by the total entropy at $x = 0.0D$.

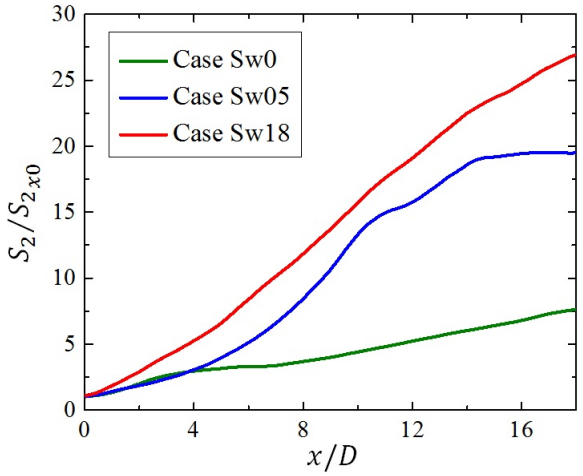

(a)

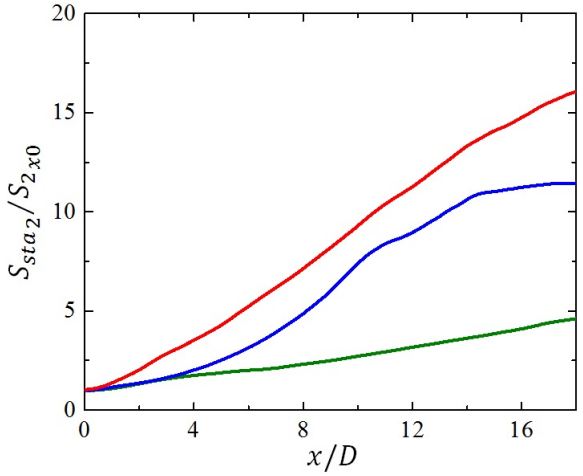

(b)

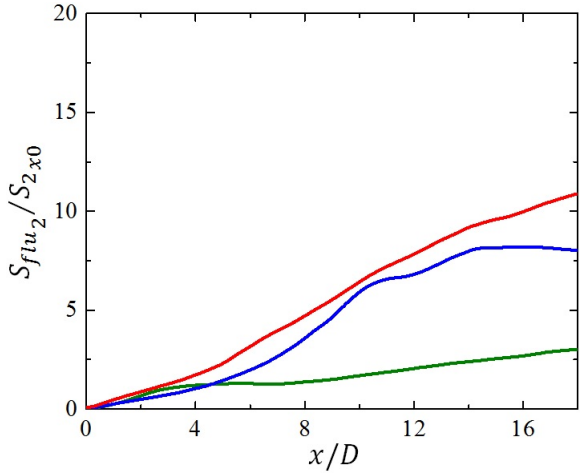

(c)

FIGURE 4.10: Axial variation of (a) total entropy, (b) statistical entropy, and (c) fluctuation entropy for an OJ scalar. Profiles are normalized by the total entropy at $x = 0.0D$.

entropy (S_{flu_k}). Figure 4.9 presents the streamwise evolution of total entropy and its terms for an IJ scalar. The values are normalized by the total entropy at the nozzle exit cross-section. For $x < 5.0D$, the total entropy values for cases Sw0 and Sw05 are comparable in magnitude. However, the entropy of case Sw05 increases at a greater rate in the downstream region. Case Sw18 consistently exhibits higher total entropy compared to the other two cases. The contribution of fluctuation entropy is greater than that of statistical entropy by over two times in all three cases. Figure 4.10, which presents the total entropy and its terms for an OJ scalar, reveals the same trends in the evolution of total entropy as those for the IJ scalar. However, statistical entropy scales higher than fluctuation entropy for the OJ scalar, unlike the IJ scalar. The above observations from the distribution of total entropy support the previous observations based on contour maps of mean scalars that case Sw05 exhibits greater diffusion of the two scalars compared to case Sw0 in the region of $x \geq 5.0D$. Additionally, case Sw18 exhibits greater diffusion than the other two cases from the nozzle exit only.

4.6.2 Segregation parameter

The segregation parameter α is defined as $\overline{\phi_1'\phi_2'}/(\overline{\phi_1}\ \overline{\phi_2})$. The numerator in this expression represents the correlation between fluctuations of two scalars at a point, which drives the sign of α. The denominator is the product of mean scalars at that point. If $\alpha \leq 0$, its magnitude can be interpreted as the degree of "unmixedness" between two scalars. In contrast, it is an indicator of the degree of "mixedness" if $\alpha > 0$. It is worth noting that $\overline{\phi_1'\phi_2'} > 0$ is only ensured by the presence of an ambient fluid. However, the converse statement is not always true (Tong & Warhaft (1995); Cai *et al.* (2011)) (refer to Appendix A for a mathematical explanation). This is because if there is no ambient fluid at a location, the scalars hold the relationship $\phi_1 + \phi_2 = 1$, which means their fluctuations are anti-correlated. Furthermore, it becomes clear that positive values of α will first become evident in the radial outward region before they appear in the downstream centerline region because additional downstream distance is required to reach the ambient fluid at the centerline.

Figure 4.11 presents the contour maps of α for the three test cases at the central cross-section plane. To retain a considerable amount of scalars and prevent α from approaching an unrealistic value, regions with $\overline{\phi_1} < 0.05$ or $\overline{\phi_2} < 0.05$ are ignored. The centerline evolutions of α for the three test cases are compared in Figure 4.12. Case Sw0 exhibits large negative values of α in the upstream region,

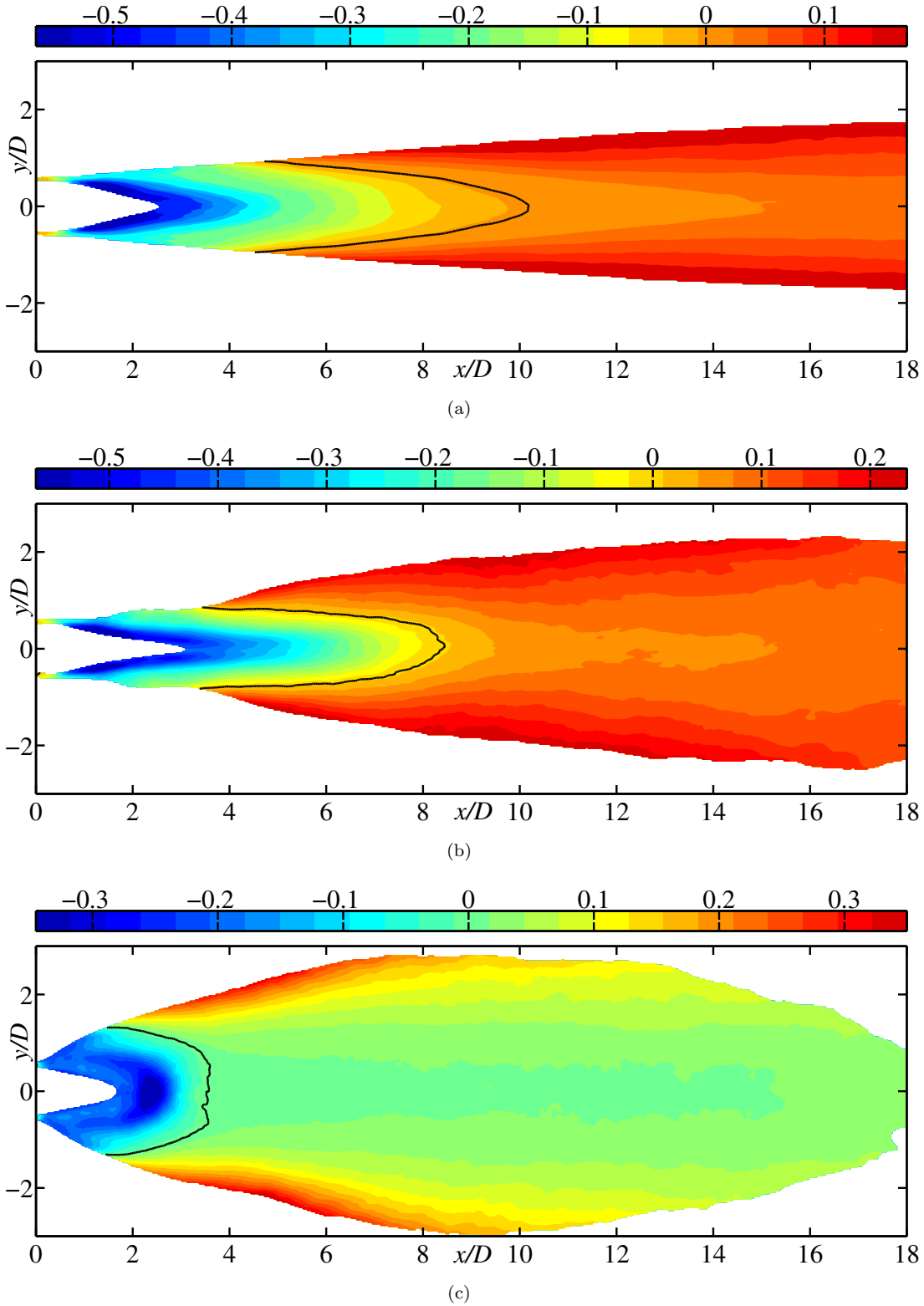

FIGURE 4.11: Segregation parameter contour maps for cases (a) Sw0, (b) Sw05, and (c) Sw18. The black line is the isoline of $\alpha = 0$, where the downstream region has $\alpha > 0$. The regions where $\overline{\phi_1} < 0.05$ or $\overline{\phi_2} < 0.05$ are whited out.

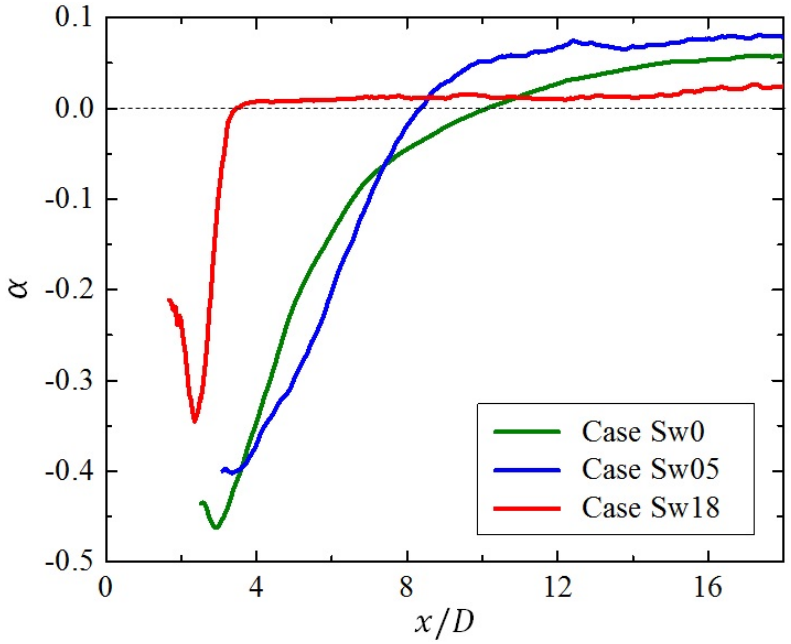

FIGURE 4.12: Centerline distribution of the segregation parameter.

indicating weak mixing. The centerline distribution shows an initial decrease, followed by a rapid increase in α. The positive α values first appear at approximately $x = 4.5D$ near $r = 0.9D$ and are visible closer to the centerline in the downstream region. The centerline distribution reveals that α becomes positive at $x \approx 10.0D$, but it approaches a constant value of ≈ 0.06 in the downstream region. This trend in the centerline distribution, where α decreases and then rapidly increases before reaching to a positive constant value, was also observed by Cai *et al.* (2011). Case Sw05 exhibits inferior α values at the region close to the centerline compared to case Sw0. However, the α value in case Sw05 tends to become positive at a farther upstream region compared to case Sw0. It is also slightly greater in the downstream region. This suggests that even though the mixing characteristics in case Sw05 are poor in the central upstream region, mixing in the radial outward region and downstream region is improved. In case Sw18, α does not decrease beyond -0.35, unlike the other two cases, and its minimum value occurs at the stagnation point. It quickly increases to a positive value by $x = 3.5D$, which is far upstream compared to the other two cases. Although case Sw18 exhibits lower α values in the downstream centerline region compared to the other two cases, its performance in the radially outward region is superior.

4.7 JPDFs at centerline stagnation point

Because the leading stagnation point on the centerline of case Sw18 (i.e., $(x, r) = (2.5D, 0.0D)$) represents large scalar fluctuations, it is interesting to examine this point further. Figure 4.13 presents the JPDF of the fluctuations of two scalars, as well as the JPDFs of the fluctuations of the streamwise velocity and each scalar. The JPDF of (ϕ_1', ϕ_2') in Figure 4.13(a) indicates negative correlation between the fluctuations of the two scalars, which was also observed for α. The distribution is a line-like shape with two noteworthy peaks: one at the second quadrant with a higher probability and the other in the fourth quadrant with a relatively low probability. The line-like shape is a consequence of insufficient ambient fluid at this location. The two peaks, however, indicate a strong flapping between ϕ_1 and ϕ_2. This flapping is caused by the oscillating stagnation point (note that the stagnation point separates the upstream region enriched with ϕ_1 and the downstream region enriched with ϕ_2) and it results in the poor mixing between ϕ_1 and ϕ_2 at this location (also evidenced by the highly negative value of α, see Figures 4.11(c) and 4.12). Figure 4.13(b) presents the JPDF of (u', ϕ_1'), which exhibits a positively correlated parallelogram-like shape distribution. This suggests a stronger streamwise flux for the IJ scalar. In addition to having a primary peak in the third quadrant, there is a secondary peak in the first quadrant with a lower probability. Similarly, the JPDF of (u', ϕ_2') in Figure 4.13(c) exhibits a parallelogram-like shape with anti-correlation between the fluctuations in streamwise velocity and the OJ scalar.

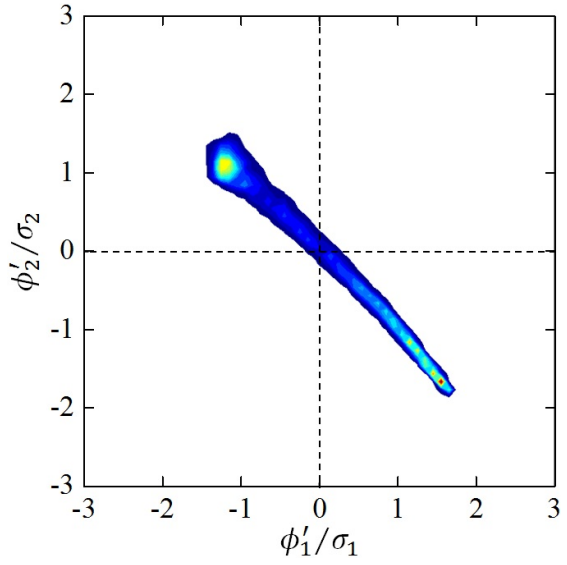
3
2
1
0
-1
-2
-3
-3
-2
-1
0
1
2
3
ϕ_2'/σ_2
ϕ_1'/σ_1

(a)

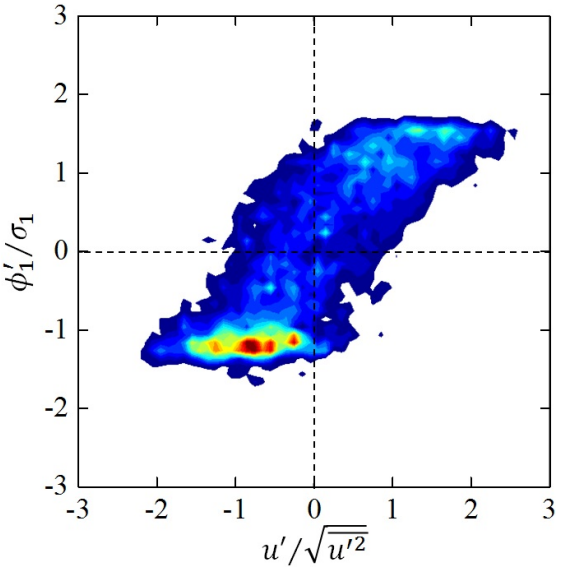
3
2
1
0
-1
-2
-3
-3
-2
-1
0
1
2
3
ϕ_1'/σ_1
$u'/\sqrt{\overline{u'^2}}$

(b)

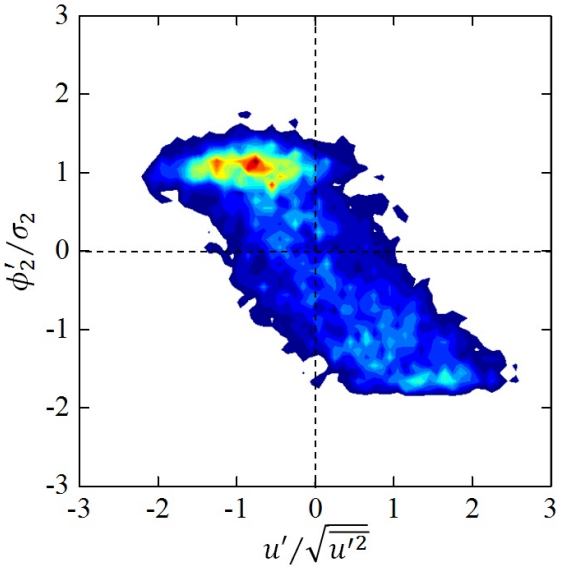

(c)

FIGURE 4.13: Joint probability density functions (JPDFs) of the (a) inner and OJ scalar fluctuations, (b) streamwise velocity and IJ scalar fluctuations, and (c) streamwise velocity and OJ scalar fluctuations for case Sw18 at the leading centerline stagnation point (i.e., $(x, r) = (2.5D, 0.0D)$). The contour levels are 0.167:0.167:3.340 for (a), 0.034:0.034:0.680 for (b), and 0.030:0.030:0.600 for (c).

4.8 Conclusions

In this section, the transport of separate passive scalars injected through each jet is studied and an attempt is made to examine the mixing between the scalars with the help of different statistics. The intermediate swirling case (i.e., case Sw05), exhibiting a contrasting acceleration in the upstream central region, exhibited a slower decay of the mean IJ scalar and slower growth of the mean OJ scalar compared to the non-swirling case. However, the downstream region exhibited a wider spread of scalars, which was confirmed by quantifying the diffusion of scalars based on entropy. In the strongly swirling case (i.e., case Sw18), the formation of an IRZ led to a dramatically improved spreading rate of mean scalars, which was also confirmed based on entropy evolution. This spreading was more prominent in this case than in the other two cases.

Enhancement of the entrainment rate because of an increase in swirling strength resulted in the enhanced mixing of both scalars with ambient fluid, since the enhanced entrainment rate is a key factor enabling positive correlation between scalar fluctuations. The greater presence of ambient fluid in the swirling cases is

also a reason for the declining peaks of OJ scalar fluctuation at the centerline compared to the IJ scalar fluctuations. A distinctively stronger turbulent azimuthal flux was observed in the swirling cases compared to the non-swirling case, where this flux was negligible. The segregation parameter demonstrates the positive correlation between scalar fluctuations, which signifies better mixing characteristics, in strongly swirling case from far upstream region. Furthermore, the maximum negative magnitude of the segregation parameter, which represents the degree of "unmixedness", was lower in the strongly swirling case compared to the other two cases.

The JPDF of the scalar fluctuations at the leading centerline stagnation point in the strongly swirling case contained two peaks, which indicates the flapping between IJ and OJ scalars caused by the oscillation of the stagnation point.

Chapter 5

SPOD analysis for strongly swirling case

5.1 Introduction

Various techniques of modal decomposition have been employed to better understand the physically important structures or modes in the flow fields. These techniques include proper orthogonal decomposition (POD) (Lumley (1967); Sirovich (1987)), dynamic mode decomposition (DMD) (Schmid (2010)), and spectral proper orthogonal decomposition (SPOD) (Sieber *et al.* (2016)), the last of which, as its name suggests, is based on POD. The method of POD focuses on the coherent structures with maximum TKE, whereas DMD separates out those coherent structures with a particular frequency. SPOD, however, attempts to leverage the characteristics of both methods, resulting in a clearer representation of the structures involved. These methods are used for the identification of structures in the swirling flows. Oberleithner *et al.* (2011) applied POD to a single swirl jet flow and demonstrated the presence of helical structures surrounding the recirculation zone. This was confirmed by Stöhr *et al.* (2011) and Markovich *et al.* (2014) with the help of modal decomposition techniques. However, the analysis in the past studies is mostly limited to the single swirling jet and that for the coaxial swirling jet is rarely explored (Rajamanickam & Basu (2018)).

The effect of the coherent structures on the passive scalars can be insightful for the investigation of mixing characteristics. Borée (2003) proposed an extension to the POD technique to investigate the influence of coherent structures on other simultaneously measured physical quantities in the system, such as pressure and

scalar concentration. Antoranz *et al.* (2018) used the extended POD modes to demonstrate a correlation between velocity and temperature in pipe flow. Stöhr *et al.* (2011) used this approach to correlate the flow and a combustion flame in swirling flow, while Sieber *et al.* (2017) also employed it in their SPOD analysis.

In this chapter, SPOD analysis is carried out at 2D planes to investigate the coherent structures present in the flow for the case of strong swirl (i.e., case Sw18). Note that the configuration of swirling coaxial jet has been rarely examined using modal decomposition techniques. The effect of the existing flow field structures on the passive scalar transport, which has also been scarcely reported, is addressed in the present study. A brief description of the SPOD methodology in §5.2 is followed by an illustration of the first few most energetic modes for the velocity and scalar fields at various cross-sections in §5.3. The influence of low-order modes on the turbulent quantities is then demonstrated in §5.4 by reconstructing those quantities. The conclusion is made in §5.5 from the implications of the results.

5.2 Method for structure identification

5.2.1 Spectral proper orthogonal decomposition

The SPOD method of Sieber *et al.* (2016) used in the present study resembles the snapshot POD method introduced by Sirovich (1987) except for the prior filtering of the correlation matrix. Consider M time-series data or snapshots collected for N grid points in a 2D plane with $M < N$. Here, each snapshot contains the three components (U, V, W) of the velocity vector $\boldsymbol{U}$, which can be decomposed into mean $\langle \boldsymbol{U} \rangle$ and fluctuating $\boldsymbol{u}'$ parts. The fluctuating part $\boldsymbol{u}'$ is arranged in matrix form as

$$\boldsymbol{u}' = \begin{bmatrix} u'(x_1,t_1) & u'(x_1,t_2) & \cdots & u'(x_1,t_M) \\ \vdots & \vdots & \vdots & \vdots \\ u'(x_N,t_1) & u'(x_N,t_2) & \cdots & u'(x_N,t_M) \\ v'(x_1,t_1) & v'(x_1,t_2) & \cdots & v'(x_1,t_M) \\ \vdots & \vdots & \vdots & \vdots \\ v'(x_N,t_1) & v'(x_N,t_2) & \cdots & v'(x_N,t_M) \\ w'(x_1,t_1) & w'(x_1,t_2) & \cdots & w'(x_1,t_M) \\ \vdots & \vdots & \vdots & \vdots \\ w'(x_N,t_1) & w'(x_N,t_2) & \cdots & w'(x_N,t_M) \end{bmatrix}, \tag{5.1}$$

where x denotes the coordinate and t_i denotes the ith snapshot. To find the optimal basis (based on optimizing the mean square of the data variable or turbulent kinetic energy while considering the fluctuating velocity field), the correlation matrix $\boldsymbol{R}$ is obtained by computing the inner product (denoted by $\langle\ ,\ \rangle$) between every pair of snapshots (temporal correlation):

$$R_{i,j} = \frac{1}{M}\ \langle \boldsymbol{u}'(\boldsymbol{x},t_i), \boldsymbol{u}'(\boldsymbol{x},t_j)\rangle, \tag{5.2a}$$

$$= \frac{1}{M}\ \sum_{l=1}^{N} \Big(u'(x_l,t_i)\ u'(x_l,t_j) + v'(x_l,t_i)\ v'(x_l,t_j) + w'(x_l,t_i)\ w'(x_l,t_j) \Big). \tag{5.2b}$$

Thus, the correlation matrix $\boldsymbol{R}$ is simply equal to $(\boldsymbol{u}'^T\boldsymbol{u}')/M$ and its size is $M \times M$. A filtering operation is now performed on the correlation matrix $\boldsymbol{R}$ to improve the diagonal similarity of $\boldsymbol{R}$, which allows continuous shifting between the energetically optimal POD and the spectrally clean DMD. A simple Gaussian low-pass filter is given by

$$S_{i,j} = \sum_{k=-M_f}^{M_f} g_k\ R_{i+k,j+k}, \tag{5.3}$$

where g_k represents the coefficients of the symmetric finite-impulse-response filter of length $2M_f + 1$. Generally, the filter length M_f can be chosen to correspond to the characteristics time scale, and in the present study it is taken as equivalent to the time D/U_{IJ}, leading to $M_f = 100$. Here, the Gaussian filter is used for the smooth temporal response taking account of periodicity at the extremes of the time series. It is given by $g_k = (1/\sqrt{2\pi}\sigma)e^{-k^2/2\sigma^2}$, with standard deviation $\sigma = M_f/5$. The eigenvalues λ_i and eigenvectors $\boldsymbol{a}_i$ of the filtered correlation matrix $\boldsymbol{S}$ are then computed by solving the eigenvalue problem. Note that the

eigenvalues λ_i represent the modal energies and are arranged in descending order of magnitude $\lambda_1 \geq \lambda_2 \geq \cdots \geq \lambda_M \geq 0$, whereas the eigenvectors $\boldsymbol{a}_i$ are the temporal mode coefficients. The ith SPOD spatial modes $\boldsymbol{\Phi}_i(\boldsymbol{x})$ are now determined by projecting the snapshots onto the temporal coefficients:

$$\boldsymbol{\Phi}_i(\boldsymbol{x}) = \frac{1}{M\lambda_i} \sum_{j=1}^{M} a_i(t_j)\ \boldsymbol{u}'(\boldsymbol{x}, t_j). \tag{5.4}$$

Finally, the fluctuations in the vector field are reconstructed by

$$\boldsymbol{u}'(\boldsymbol{x}, t_j) = \sum_{i=1}^{m} a_i(t_j)\ \boldsymbol{\Phi}_i(\boldsymbol{x}). \tag{5.5}$$

Here, m denotes the number of modes used for the reconstruction of the field, and its magnitude can be scaled anywhere between 1 and M to demonstrate the contribution of low-order modes.

5.2.2 Extension to the passive scalar field

The above analysis is then extended to the simultaneously computed scalar field by using the approach of Borée (2003) which demonstrates the correlation between the flow structures and scalar field. Similar to the velocity field, the scalar ϕ is decomposed into mean $\langle\phi\rangle$ and fluctuating ϕ' parts (the subscript on ϕ denoting the IJ or OJ scalar is omitted here to avoid confusion). Analogously to Equation 5.4, the extended SPOD modes $\Psi_i(\boldsymbol{x})$ are determined for each scalar:

$$\Psi_i(\boldsymbol{x}) = \frac{1}{M\lambda_i} \sum_{j=1}^{M} a_i(t_j)\ \phi'(\boldsymbol{x}, t_j), \tag{5.6}$$

where the modal energies λ_i and the temporal mode coefficients $a_i(t_j)$ are the same as those obtained from the decomposition of the velocity field. It was shown by Borée (2003) that these modes give only the part that is correlated with the SPOD velocity modes $\boldsymbol{\Phi}_i(\boldsymbol{x})$, while reconstructing the field of scalar fluctuations,

$$\phi'_{corr}(\boldsymbol{x}, t_j) = \sum_{i=1}^{m} a_i(t_j)\ \Psi_i(\boldsymbol{x}), \tag{5.7}$$

whereas the part that is uncorrelated with these modes is given by

$$\phi'_{uncorr}(\boldsymbol{x}, t_j) = \phi'(\boldsymbol{x}, t_j) - \phi'_{corr}(\boldsymbol{x}, t_j). \tag{5.8}$$

In the present study, $\phi'_{uncorr}(\boldsymbol{x}, t_j)$ is calculated exactly by prior calculation of $\phi'_{corr}(\boldsymbol{x}, t_j)$ by taking $m = M$, while the effect of the correlated low-order modes is demonstrated by varying m,

$$\phi'(\boldsymbol{x}, t_j) = \phi'_{uncorr}(\boldsymbol{x}, t_j) + \sum_{i=1}^{m} a_i(t_j)\ \Psi_i(\boldsymbol{x}). \tag{5.9}$$

5.2.3 Data extraction

The number of snapshots (M) taken for SPOD analysis is $10,000$. The cross-sections just upstream and downstream of the central leading stagnation point are focused in this study. Thus, the data is extracted from the $2d$ cross-sections at $x/D = 0.3$, 1.0, 2.5, and 3.5. The corresponding extracted cross-sectional domains ($L_y \times L_z$) are $2D \times 2D$, $3D \times 3D$, $4D \times 4D$, and $4D \times 4D$, while the corresponding grid points ($N_y \times N_z$) are 141×141, 211×211, 281×281, and 281×281, respectively. Thus, the number of snapshots is such that $M < N$, where total grid points $N = N_y \times N_z$. The SPOD analysis is carried out using the computing language MATLAB.

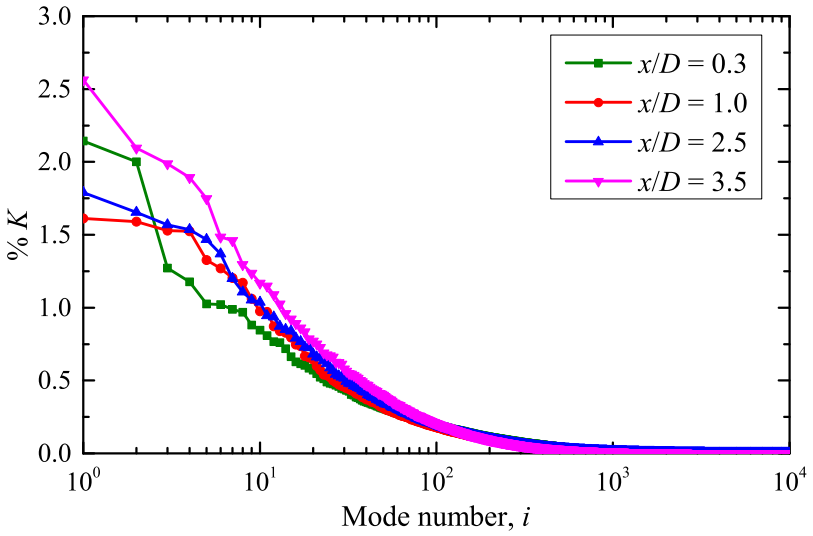

FIGURE 5.1: Percentage energy content of velocity fluctuations ($K = \lambda_i / \sum_{k=1}^{M} \lambda_k$) in the considered four downstream y-z sections associated with SPOD mode i.

5.3 SPOD spatial modes

5.3.1 SPOD spatial modes of velocity field

Figure 5.1 shows the percentage energy content of the SPOD mode of velocity fluctuations ($K = \lambda_i / \sum_{k=1}^{M} \lambda_k$) at the four selected cross-sections (i.e., at $x/D = 0.3$, 1.0, 2.5, and 3.5). The first four (most energetic) SPOD spatial modes of the velocity field ($\mathbf{\Phi}_1$, $\mathbf{\Phi}_2$, $\mathbf{\Phi}_3$, and $\mathbf{\Phi}_4$) are then as depicted in Figures 5.2-5.5, with the contour maps representing the streamwise velocity component and the vectors representing the resultant of the cross-streamwise velocity components. Red and blue in the contour maps indicate positive and negative values, respectively.

At the cross-section $x/D = 0.3$, the first four modes contribute 6.6% of the total energy (for the first, second, third, and fourth modes, $K = 2.1\%$, 2.0%, 1.3%, and 1.2%, respectively), and 50% of the total energy is recovered by 141 modes. The first two spatial modes $\mathbf{\Phi}_1$ and $\mathbf{\Phi}_2$ (see Figure 5.2) resemble each other with a phase shift and thus form the first pair of modes. Three pairs of alternate lobe-like structures appear in these two modes at the ISL (around $r/D = 0.7$). Here, a pair of alternate lobe-like structures refers to the alternate regions of positive (red contours) and negative (blue contours) streamwise components of the spatial mode of the velocity field. It can be observed that the positive streamwise component of the spatial mode of the velocity field is associated with the counterclockwise

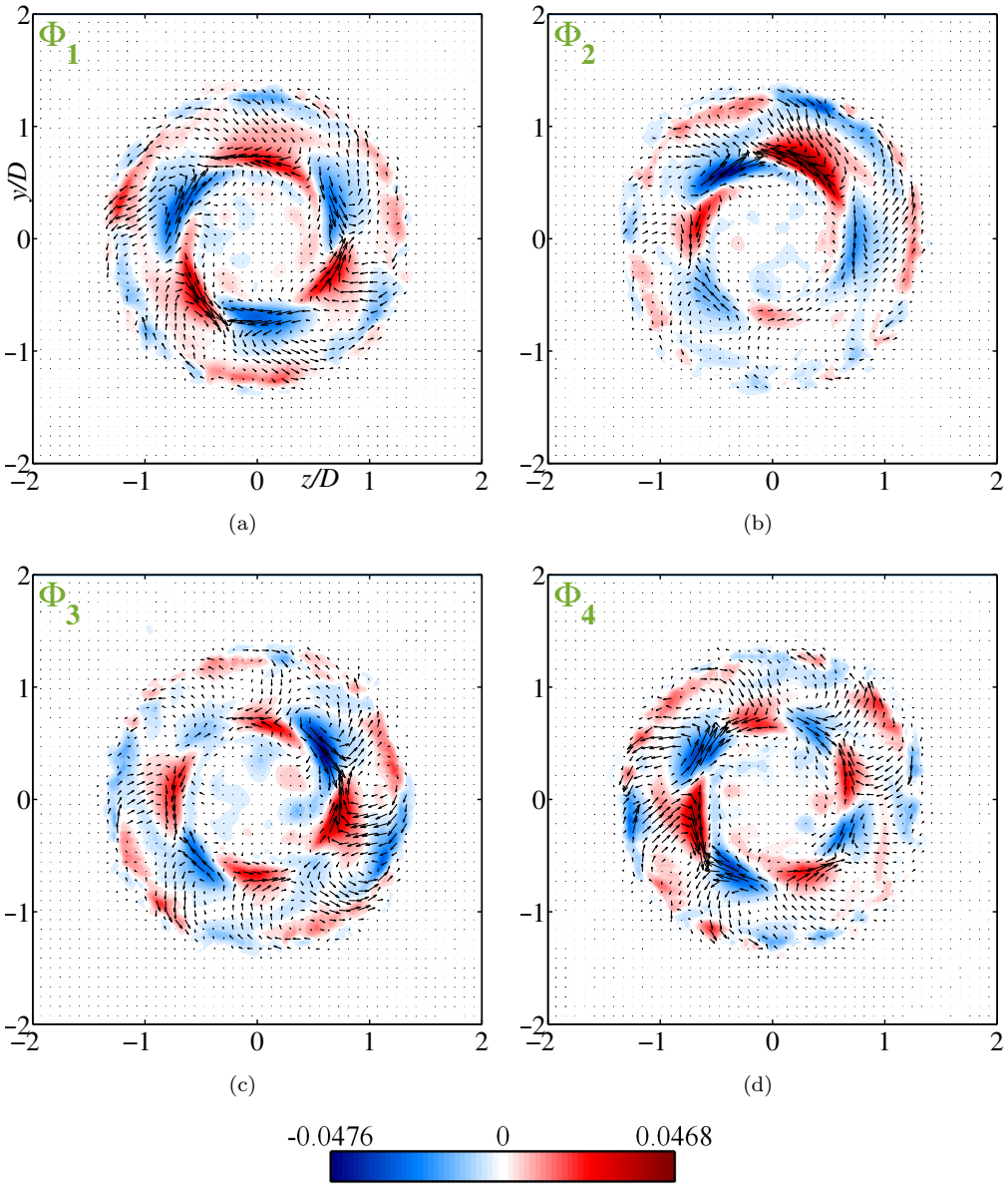

FIGURE 5.2: First four SPOD spatial modes of the velocity field in the y-z plane at the cross-sections $x/D = 0.3$. Contour maps represent the streamwise velocity component.

(swirling direction) vectors and the negative one with the clockwise (opposite to swirling direction) vectors. The next two modes $\mathbf{\Phi}_3$ and $\mathbf{\Phi}_4$ form the second pair of modes with a phase shift, and these modes contain four pairs of alternate lobe-like structures with similar characteristics to those in the preceding modes.

Further downstream at the cross-section $x/D = 1.0$, the contribution of the first four modes is slightly reduced compared with that at the upstream cross-section, to 6.3% of the total energy (for the first, second, third, and fourth modes, $K = 1.6\%$, 1.6%, 1.5%, and 1.5%, respectively). It can be seen that these four

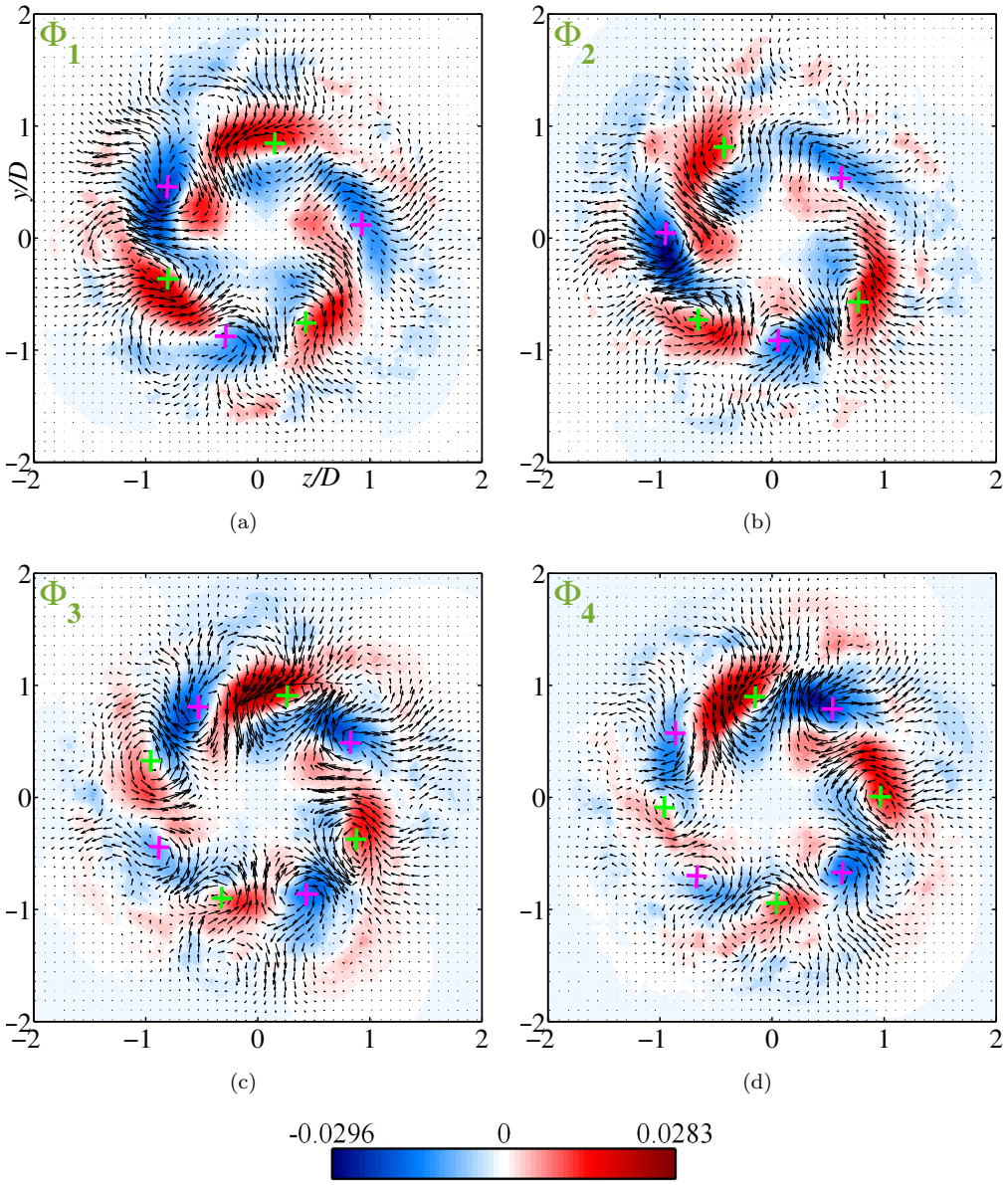

FIGURE 5.3: First four SPOD spatial modes of the velocity field in the y-z plane at the cross-sections $x/D = 1.0$. Contour maps represent the streamwise velocity component. Green colored + symbol is used for counter-clockwise vortices and pink colored + symbol is used for clockwise vortices.

modes represent approximately equal energy content, unlike that in the upstream cross-section, where the first pair of modes represents slightly higher energy content compared with the second pair. Fewer modes (130) are required to recover the 50% of total energy at this cross-section $x/D = 1.0$ compared with the upstream cross-section. The spatial modes of the velocity field at this downstream cross-section $x/D = 1.0$ (see Figure 5.3) show notable features. Apart from having three pairs of alternate lobe-like structures in modes $\mathbf{\Phi}_1$ and $\mathbf{\Phi}_2$ (the first pair of modes), and four pairs of alternate lobe-like structures in $\mathbf{\Phi}_3$ and $\mathbf{\Phi}_4$ (the second pair of

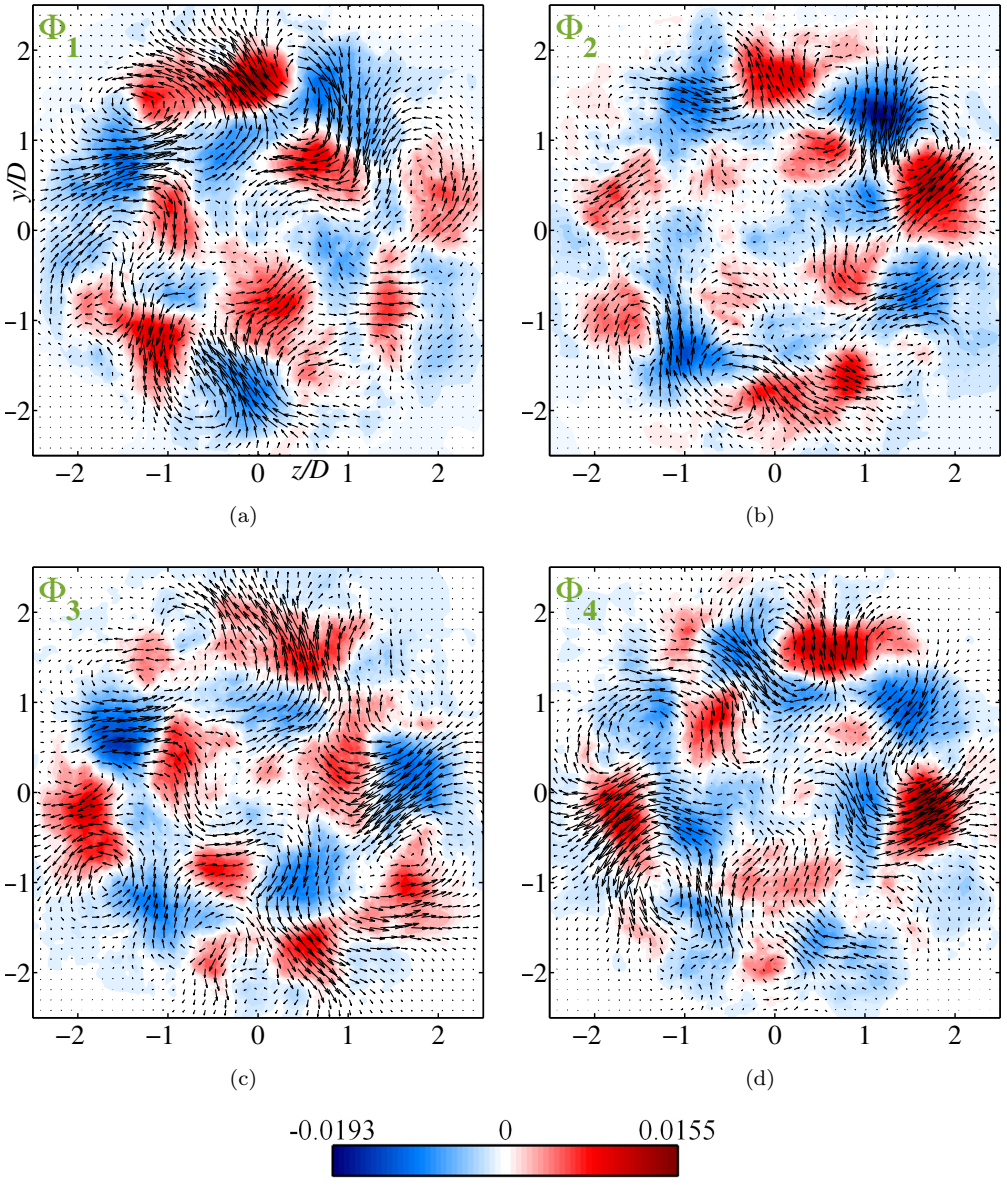

FIGURE 5.4: First four SPOD spatial modes of the velocity field in the y-z plane at the cross-sections $x/D = 2.5$. Contour maps represent the streamwise velocity component.

modes), three pairs of counter-rotating vortical structures appear in the first pair of modes, and four pairs of such structures appear in the second pair of modes. The centers of these vortical structures lie at approximately $r/D = 0.9$ (situated at the outer region of the ISL). Lobe-like structures have also been reported in other studies. Stöhr *et al.* (2011) reported a pair of similar lobe-like structures for the first two POD modes in their study on co-swirling flows. The configuration of coaxial jet with swirl in the OJ was studied by Rajamanickam & Basu (2018), who also reported the existence of similar three and four pairs of lobe-like structures

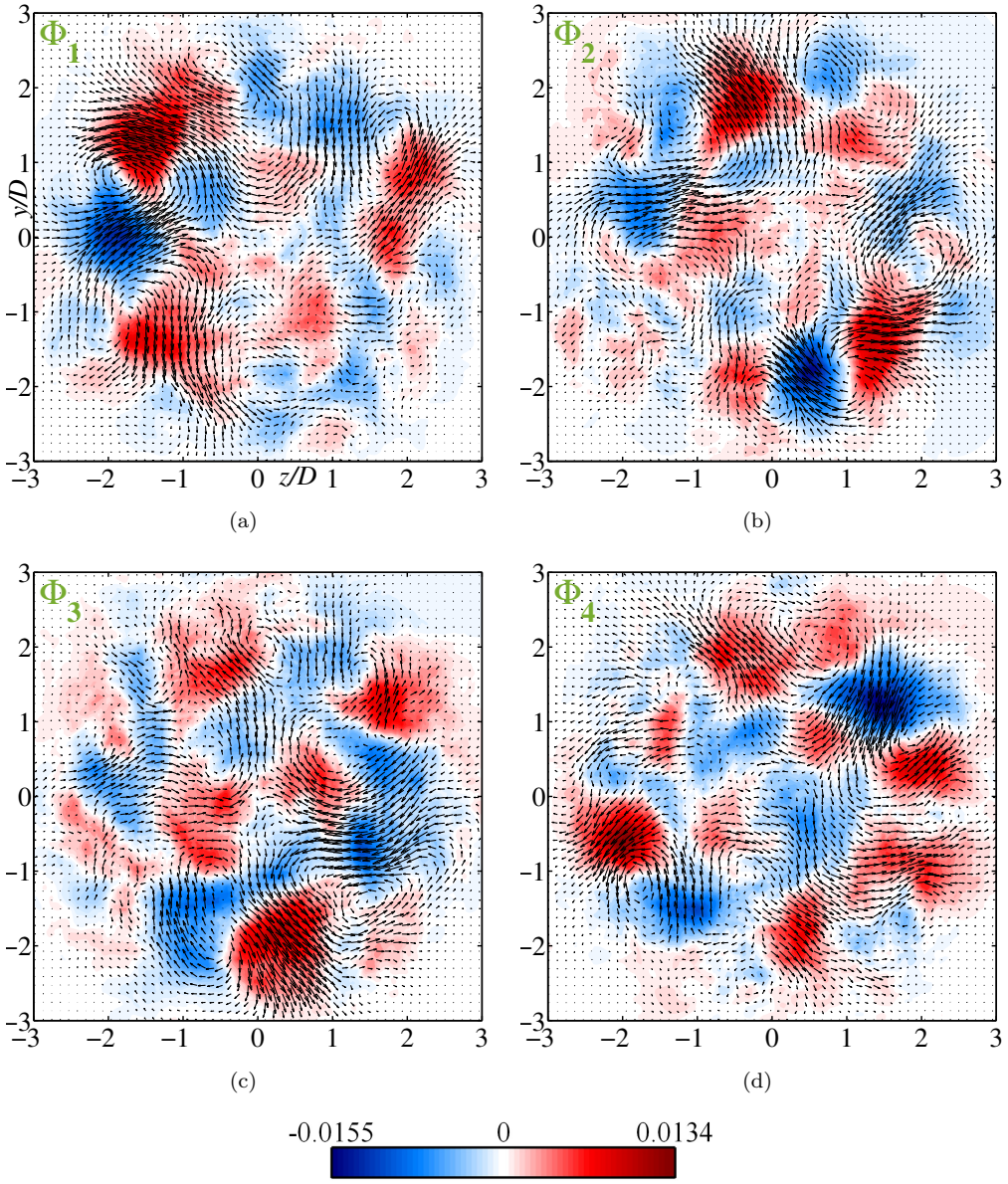

FIGURE 5.5: First four SPOD spatial modes of the velocity field in the y-z plane at the cross-sections $x/D = 3.5$. Contour maps represent the streamwise velocity component.

for the first and second pairs of POD modes, respectively, in their pre-vortex-breakdown case (which exhibits a separated recirculation zone surrounding the IJ flow).

At the downstream cross-section $x/D = 2.5$, there is a slightly higher energy contribution K from the first four modes compared with the upstream cross-section $x/D = 1.0$ (for the first, second, third, and fourth modes, $K = 1.8\%$, 1.7%, 1.6%, and 1.5%, respectively). However, the spatial modes of the velocity field (see

Figure 5.4) suggest that the organized lobe-like structures as well as counter-rotating vortical structures are disrupted. Furthermore, modes $\mathbf{\Phi}_1$ and $\mathbf{\Phi}_2$ and modes $\mathbf{\Phi}_3$ and $\mathbf{\Phi}_4$ are not paired, since they exhibit dissimilar structures. At the cross-section $x/D = 3.5$, the spatial modes of the velocity field (see Figure 5.5) are featureless, with no clear evidence of counter-rotating vortical structures.

The development of the spatial modes (the most energetic four modes) of the velocity field reveals that counter-rotating vortical structures form at the upstream region around the IRZ and eventually fade out in the downstream region. The effects of these structures on the passive scalar fields and turbulent quantities are discussed in §5.3.2 and §5.4, respectively. The cross-section $x/D = 3.5$ is not considered for further investigation, since it shows featureless structures.

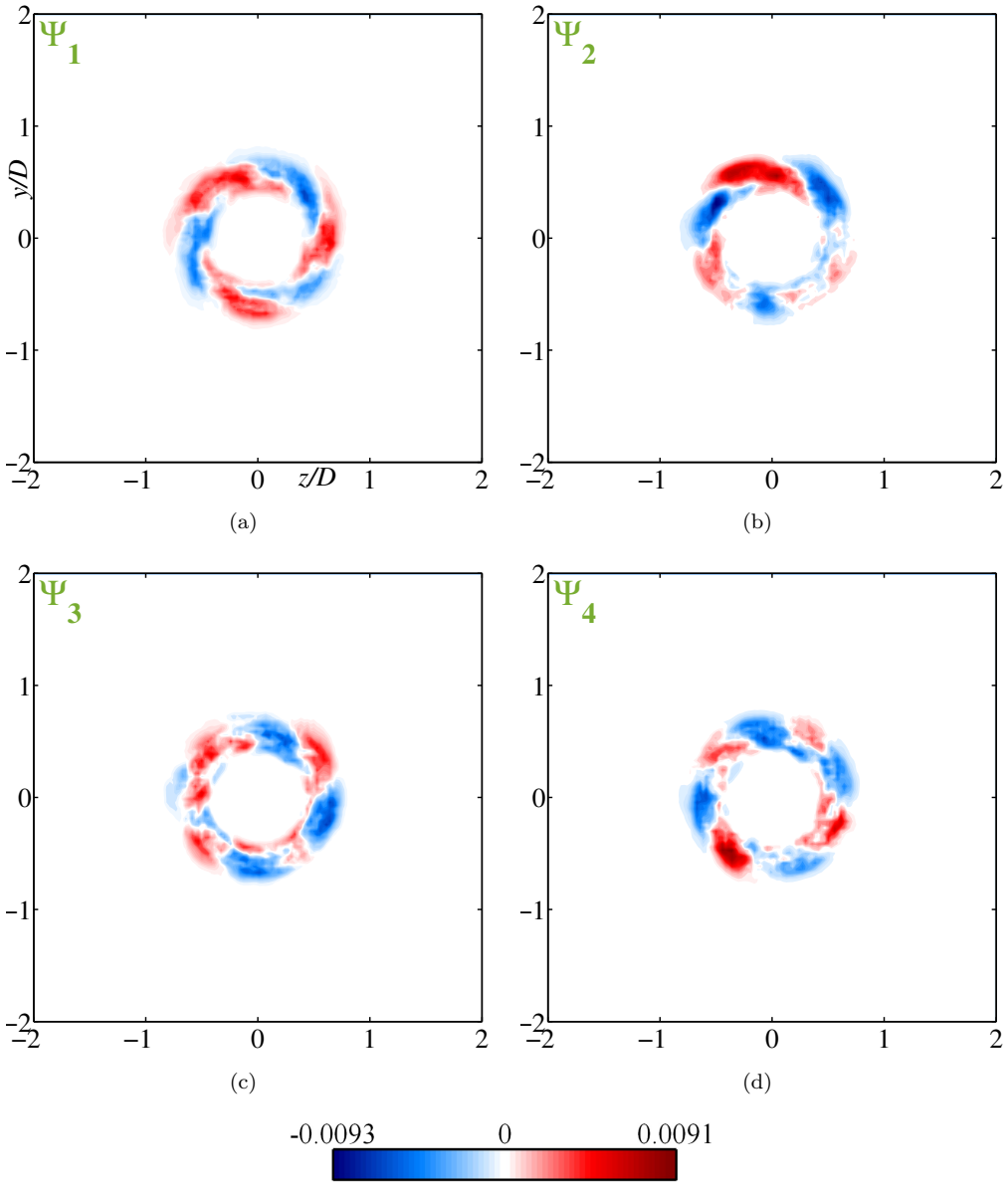

FIGURE 5.6: First four extended SPOD spatial modes of the IJ scalar (ϕ_1) field in the y-z plane at the cross-section $x/D = 0.3$.

5.3.2 Extended SPOD spatial modes of passive scalar fields

This section presents the first four (most energetic) extended SPOD spatial modes ($\Psi_i(\boldsymbol{x})$) of IJ and OJ scalar fields at cross-sections $x/D = 0.3$, 1.0, and 2.5.

At $x/D = 0.3$, the extended spatial modes of both scalar fields (see Figures 5.6 and 5.7) exhibit three and four pairs of alternate lobe-like structures (although not very clearly) in modes Ψ_1 and Ψ_2 (first pair of modes), and Ψ_3 and Ψ_4 (second pair of modes), respectively, at the ISL $0.4 \leq r/D \leq 0.7$. Note that the positive mode values of the IJ scalar coincide with the negative mode values of the OJ scalar

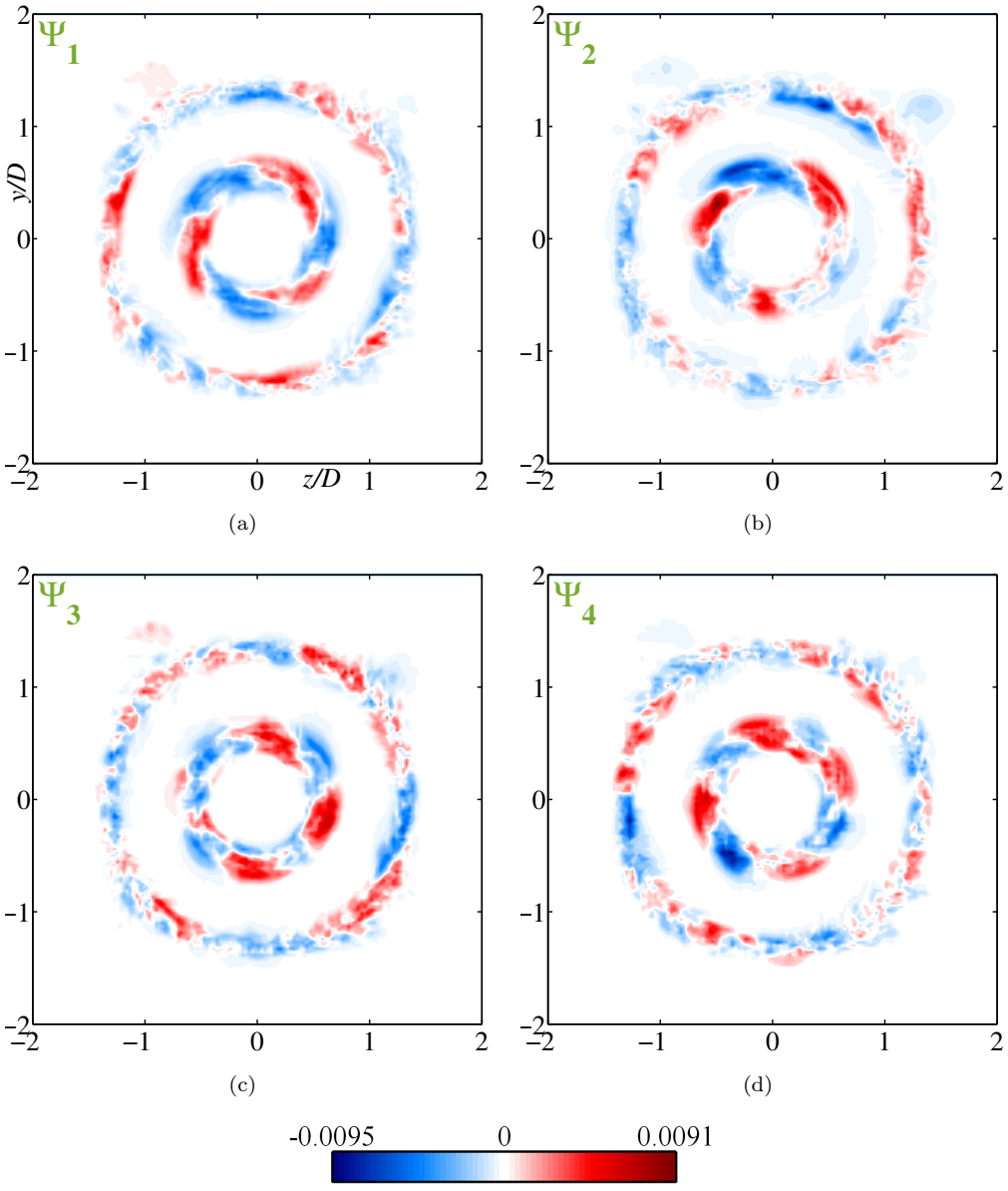

FIGURE 5.7: First four extended SPOD spatial modes of the OJ scalar (ϕ_2) field in the y-z plane at the cross-section $x/D = 0.3$.

in this region, which suggests a negative covariance between the two scalars. This is caused by the insufficiency of ambient fluid at this cross-section (as explained in §4.6.2). The spatial modes of the OJ scalar show featureless structures at the OSL ($r/D > 1.0$).

Noteworthy features in the extended spatial modes of both scalar fields are observed at the downstream location $x/D = 1.0$ (see Figures 5.8 and 5.9). To demonstrate the effect of counter-rotating vortical structures, the vector plots from spatial modes of velocity field are superimposed on the contour maps of first and third modes of scalar fields. Three and four pairs of lobe-like structures clearly

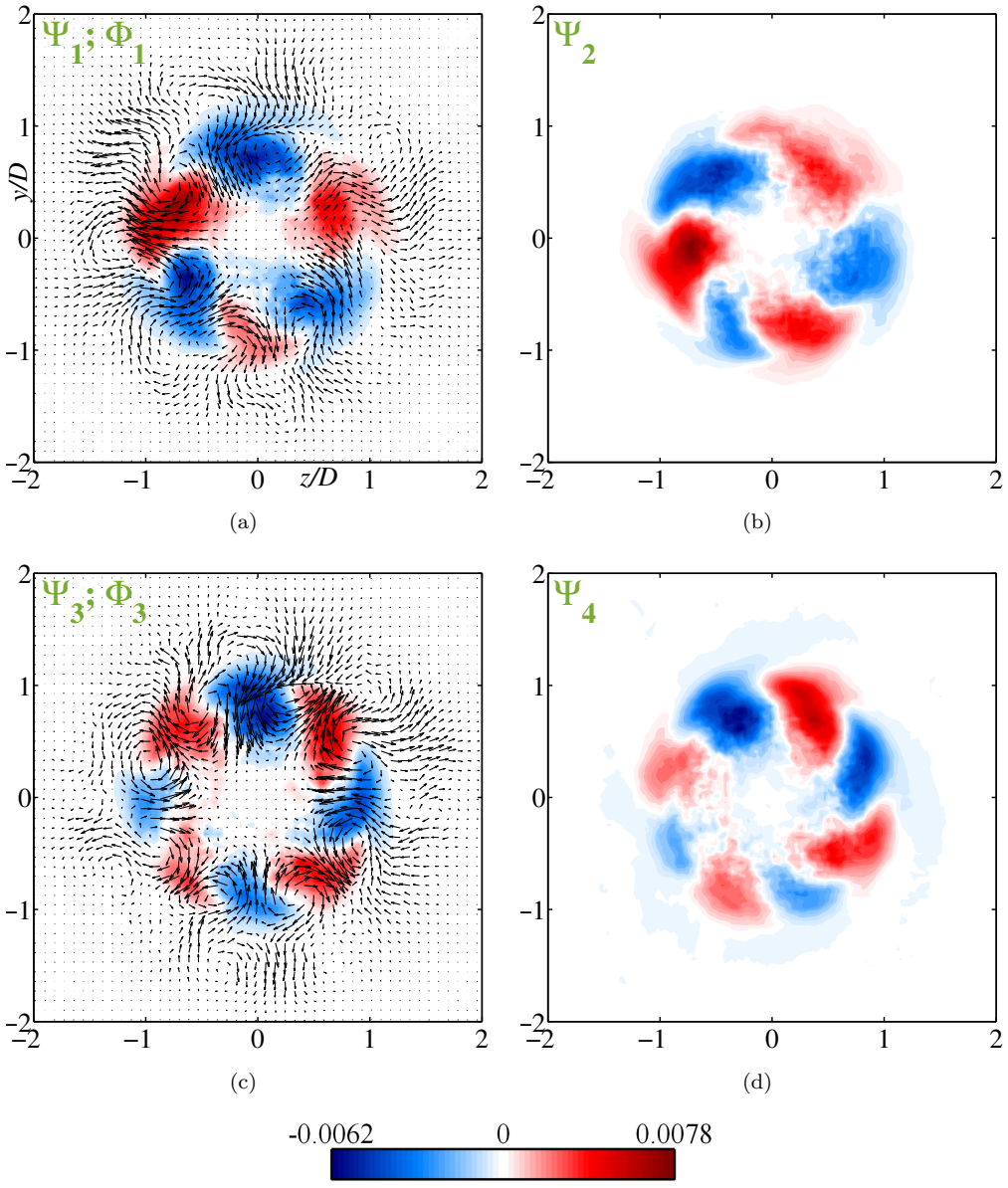

FIGURE 5.8: First four extended SPOD spatial modes of the IJ scalar (ϕ_1) field in the y-z plane at the cross-section $x/D = 1.0$. Vectors from spatial modes of velocity field are superimposed on first and third modes to demonstrate the effect of counter-rotating vortices.

appear in the first and second pairs of spatial modes, respectively, of the two scalars. Moreover, these structures for spatial modes of the IJ scalar are confined to the ISL $r/D \leq 1.2$, while the spatial modes of the OJ scalar exhibit distinct patterns in both the ISL $r/D \leq 1.2$ and OSL $r/D > 1.2$. It can be observed that positive values of the spatial modes of the IJ scalar are predominantly associated with outward (radially) vectors and negative values are associated with inward vectors. In the case of the spatial modes of the OJ scalar, the opposite behavior is seen in the ISL $r/D \leq 1.2$, since positive and negative values of spatial modes

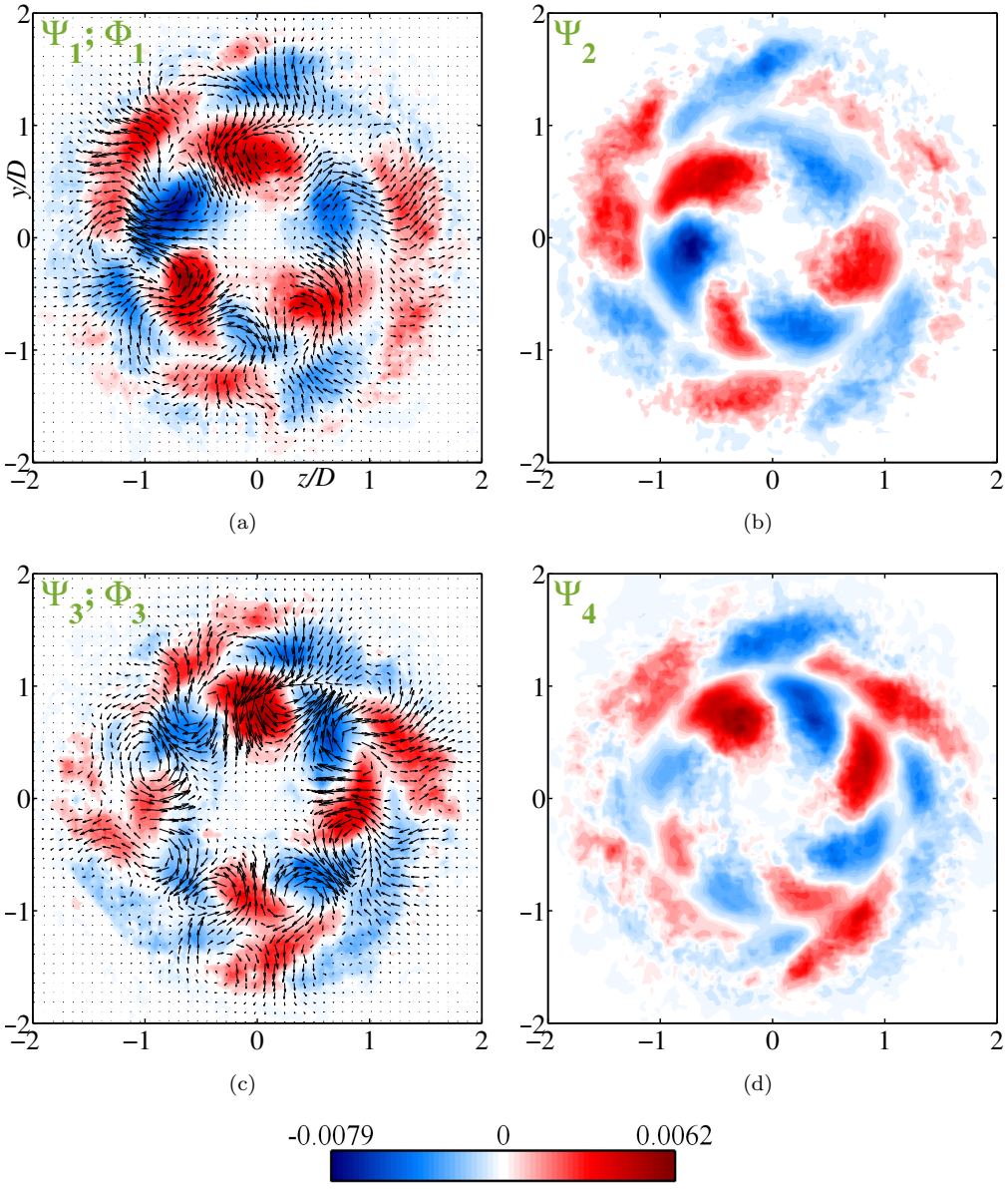

FIGURE 5.9: First four extended SPOD spatial modes of the OJ scalar (ϕ_2) field in the y-z plane at the cross-section $x/D = 1.0$. Vectors from spatial modes of velocity field are superimposed on first and third modes to demonstrate the effect of counter-rotating vortices.

are associated with inward and outward vectors, respectively. This reflects the fact that the counter-rotating vortices stimulate outward and inward radial fluxes of the IJ and OJ scalars, respectively, which is essential for mixing between the two scalars. However, the structures in the OSL $r/D > 1.2$ exhibit outward radial flux of the OJ scalar, since positive values of spatial modes are accompanied by outward vectors.

At the downstream cross-section $x/D = 2.5$ (see Figures 5.10 and 5.11),

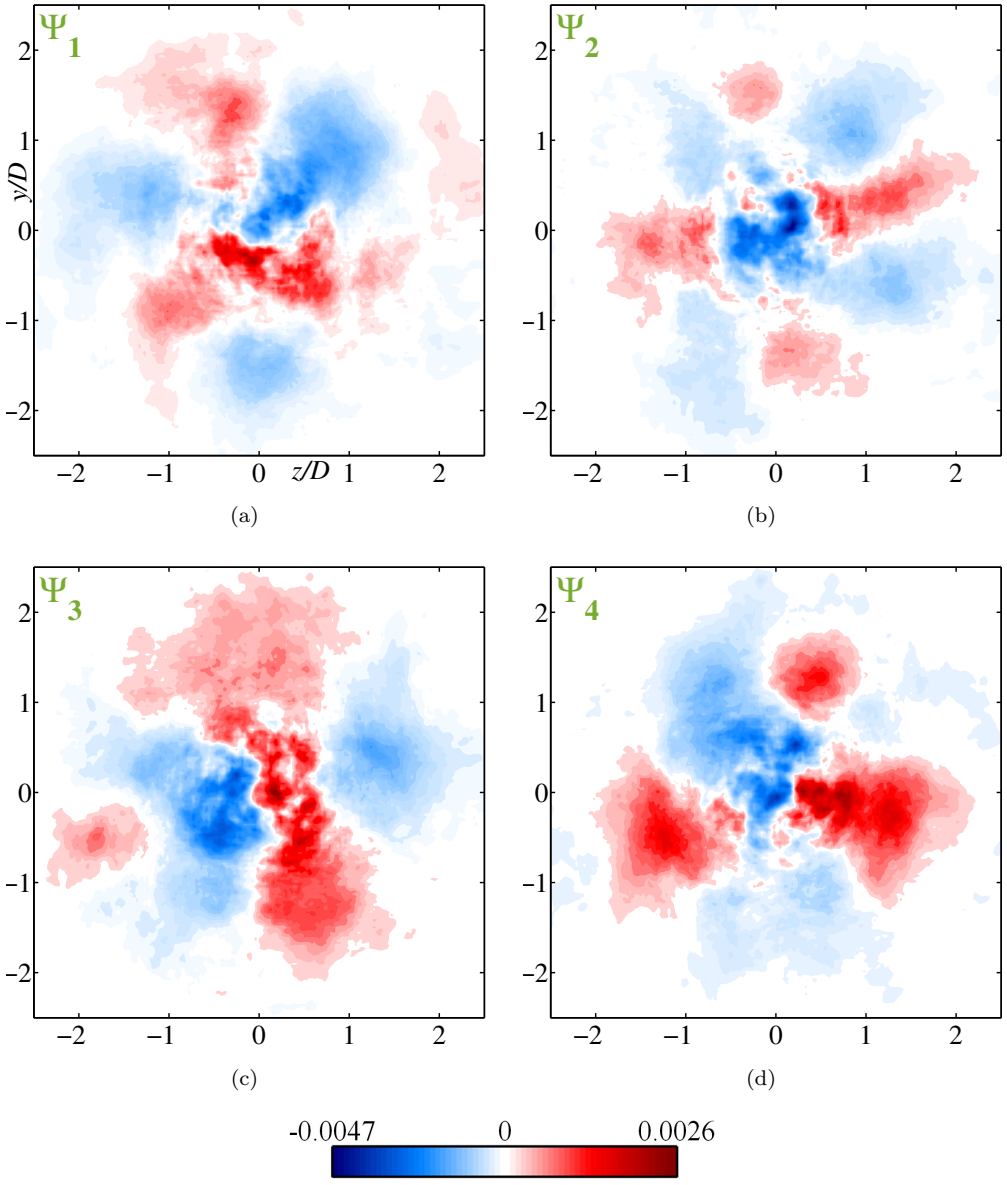

FIGURE 5.10: First four extended SPOD spatial modes of the IJ scalar (ϕ_1) field in the y-z plane at the cross-section $x/D = 2.5$.

the first four spatial modes of both scalars do not show organized structures like those in the upstream sections. Moreover, these spatial modes are not paired with each other.

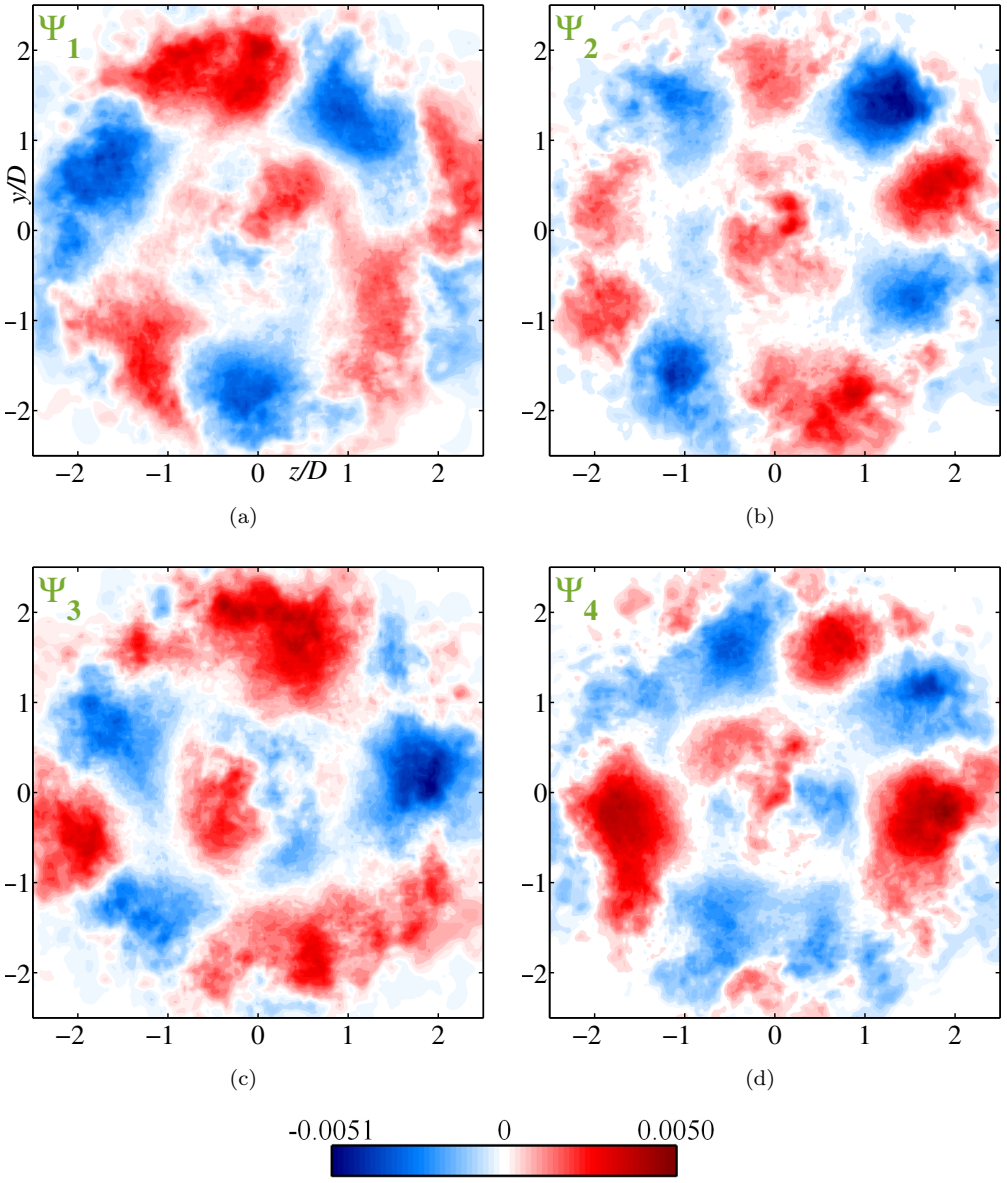

FIGURE 5.11: First four extended SPOD spatial modes of the OJ scalar (ϕ_2) field in the y-z plane at the cross-section $x/D = 2.5$.

5.4 Reconstruction of turbulent quantities

In this subsection, various turbulent quantities are reconstructed from the SPOD modes with m = 1, 2, 4, 8, 50, and 200 at the cross-section $x/D = 1.0$ to demonstrate the effect of the organized counter-rotating vortical structures present in the region. These reconstructed turbulent quantities are compared with the quantities evaluated from the original instantaneous total data (i.e., a total of 10,000 snapshots). Although the extracted data is processed in Cartesian coordinate system (not the cylindrical coordinate), the reconstructed turbulent quantities W_{rms}, V_{rms} and $\langle v'\phi'_k \rangle$ presented in this subsection are referred to the azimuthal RMS velocity, radial RMS velocity and radial fluxes of scalar since the turbulent quantities are reconstructed over the vertical line passing through the center $(0, 0)$ of cross-section.

5.4.1 RMS velocity fluctuations

Figure 5.12 presents the radial distributions of the streamwise (U_{rms}), azimuthal (W_{rms}), and radial (V_{rms}) components of the RMS velocity reconstructed using m = 1, 2, 4, 8, 50, and 200, and compares them with the respective quantities determined using the original instantaneous data. For U_{rms}, the contribution of the first four modes ($m = 4$) is significantly higher for the upper inner peak at $y/D \approx 0.9$ (situated in the outer region of the ISL); however, it is lower for the lower inner peak at $y/D \approx -0.9$ (also situated in the outer region of the ISL). Note that the locations of the centers of the counter-rotating vortices also lie at $r/D \approx 0.9$. Thus, the greater contributions of the first four modes can be attributed to the presence of counter-rotating vortical structures. This inequality in contribution between the upper and lower regions is caused by the asymmetrical nature (in the axial direction) of the spatial modes (see Figure 5.3). The contribution of low-order modes ($m \leq 8$) is smaller for the outermost peaks at $y/D \approx \pm 1.4$ (situated in the OSL), which manifests the dominance of the high-order structures (or small-scale structures) in the OSL region. The modes $m = 200$ are observed to be insufficient to completely recover the profile obtained from total data in both the inner and OSL. Similar trends are also observed in the profiles of W_{rms} and V_{rms}. Although the contribution from the low-order modes ($m \leq 8$) for the outermost peaks at $y/D \approx \pm 1.4$ is observed to be considerably greater in the cases of W_{rms} and V_{rms} compared with U_{rms}, it is still lower compared with the respective inner peaks at $y/D \approx \pm 0.9$ in the cases of both W_{rms} and V_{rms}. The above discussion

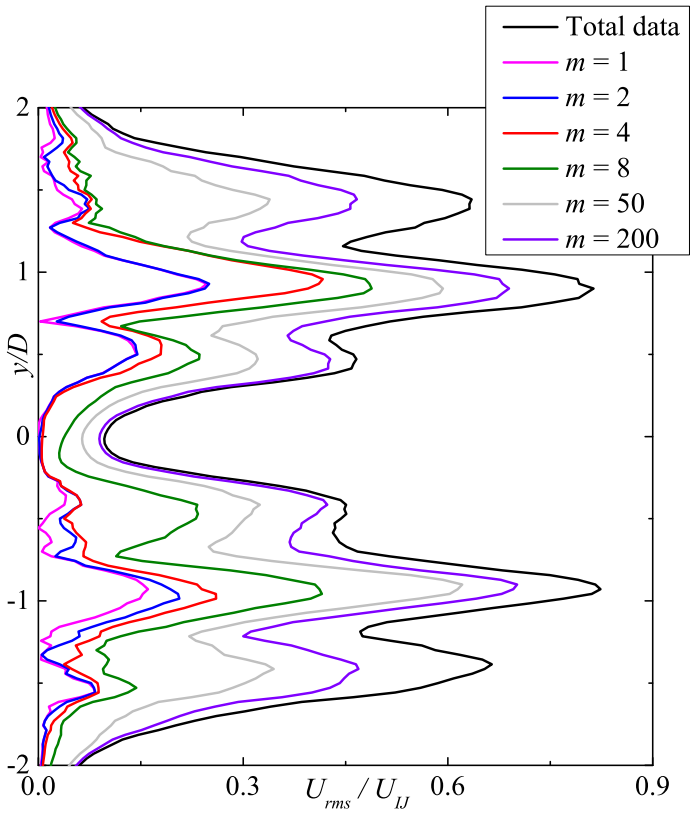
Total data
m = 1
m = 2
m = 4
m = 8
m = 50
m = 200
2
1
0
-1
-2
y/D
0.0
0.3
0.6
0.9
U_rms / U_IJ

(a)

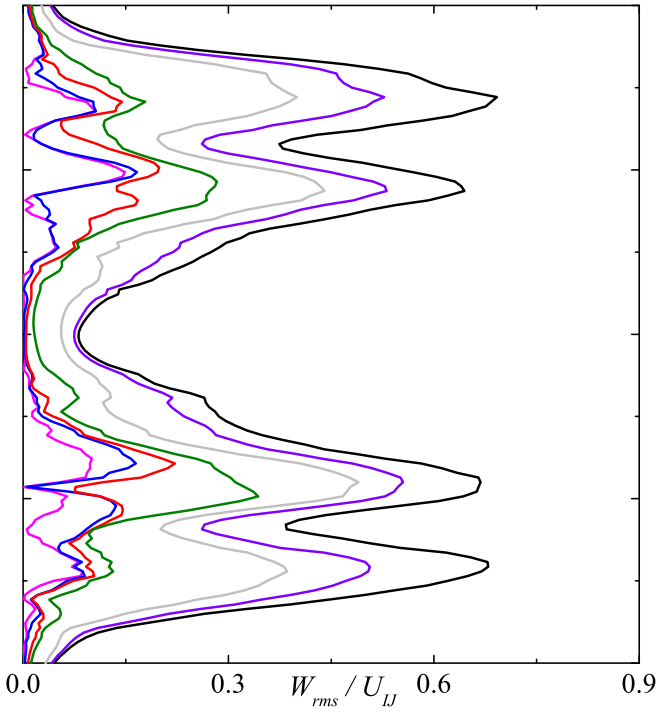
0.0
0.3
0.6
0.9
W_rms / U_IJ

(b)

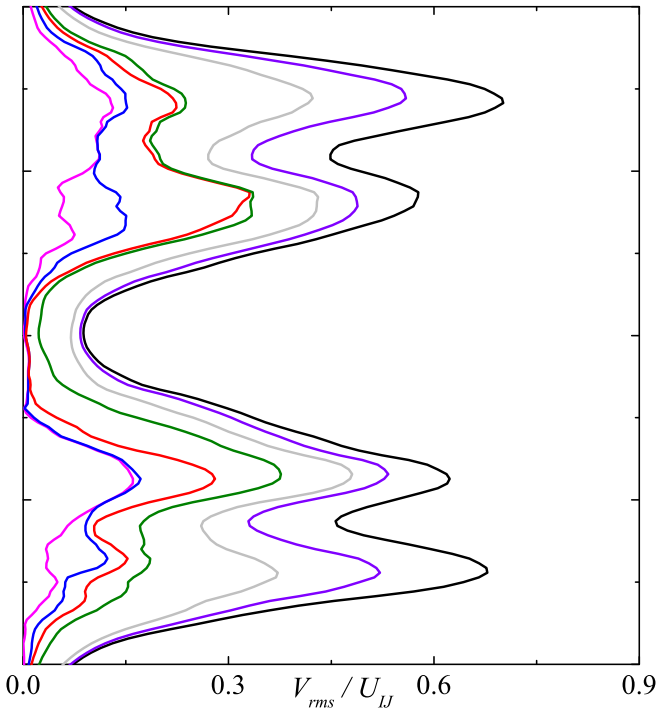

(c)

FIGURE 5.12: Reconstruction of RMS velocities using first m number of modes at the cross-section $x/D = 1.0$. (a) Streamwise RMS velocity. (b) Azimuthal RMS velocity. (c) Radial RMS velocity. "Total data" represents the quantity evaluated from the original instantaneous data.

demonstrates that the counter-rotating vortices are essentially contributing to the RMS velocity peaks in the ISL ($y/D \approx \pm 0.9$), whereas the high-order structures are the sources of the RMS velocity peaks in the OSL ($y/D \approx \pm 1.4$).

5.4.2 RMS scalar fluctuations, covariance between two scalars, and radial turbulent flux of scalars

Figure 5.13 shows the radial distributions of the RMS fluctuations of the IJ scalar (ϕ_{1_rms}) and OJ scalar (ϕ_{2_rms}), and Figure 5.14 shows the covariance between the two scalars ($\langle \phi_1' \phi_2' \rangle$) reconstructed using $m = 1$, 2, 4, 8, 50, and 200, and compares them with the respective quantities evaluated using the original instantaneous data. The first four modes ($m = 4$) contribute significantly to the ISL peak ($y/D \approx \pm 0.7$) of both ϕ_{1_rms} and ϕ_{2_rms}. However, the contribution is less in the lower region ($y/D < 0$) than the upper region ($y/D > 0$), which is

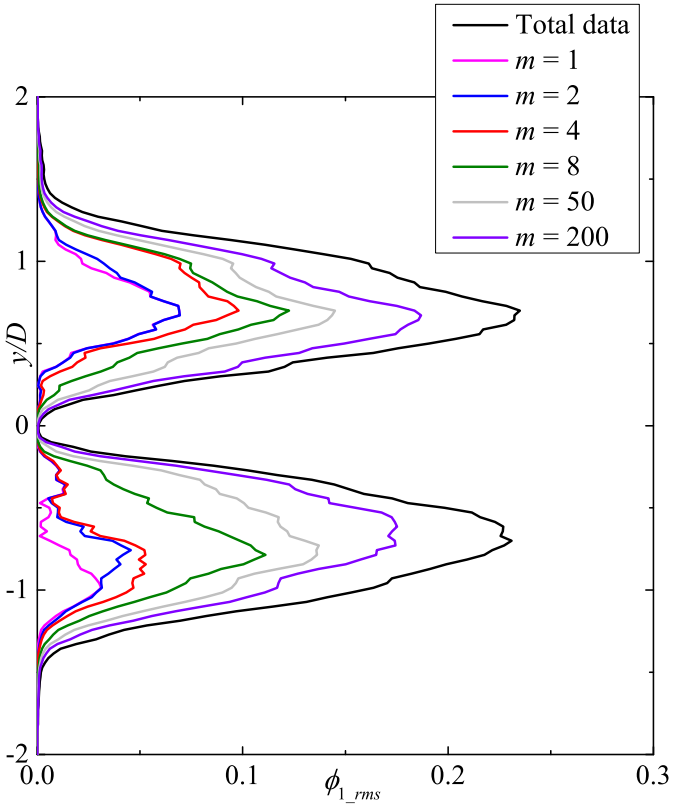

(a)

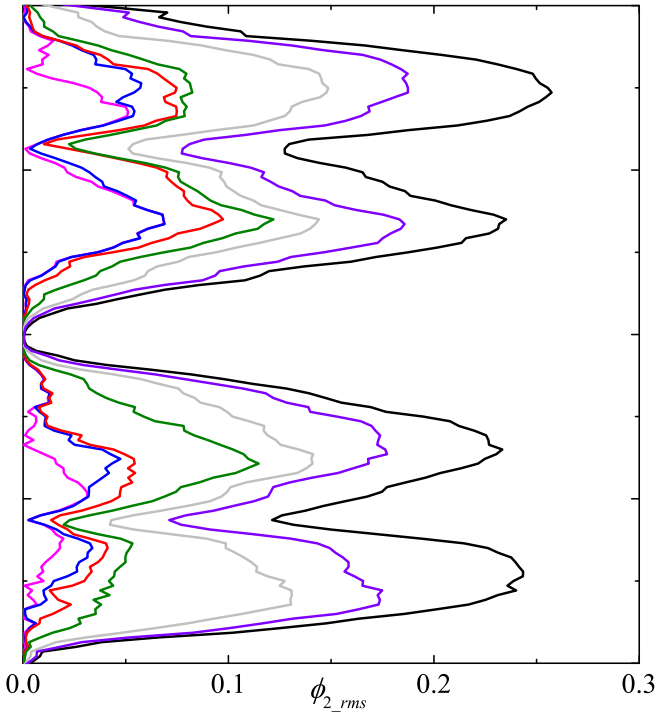

(b)

FIGURE 5.13: Reconstruction of RMS scalar fluctuations using first m number of modes at the cross-section $x/D = 1.0$. (a) The RMS fluctuations of IJ scalar. (b) The RMS fluctuations of OJ scalar.

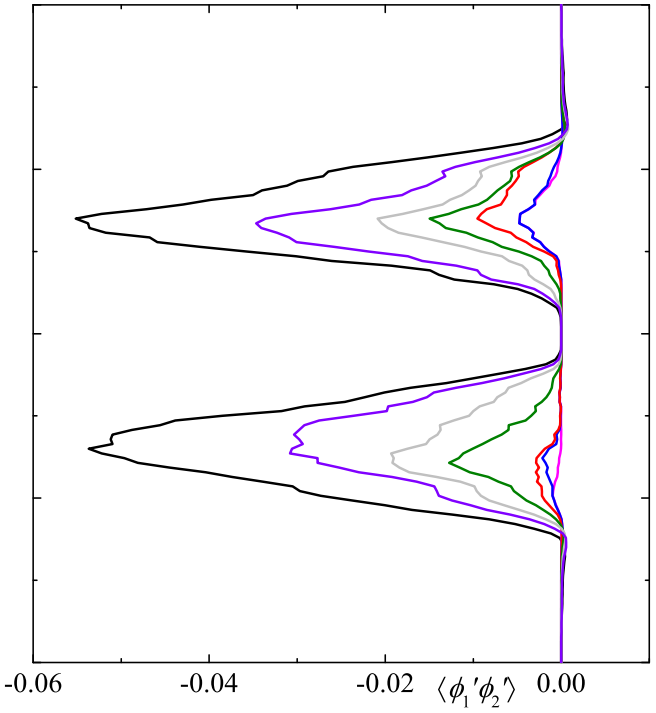

FIGURE 5.14: Reconstruction of covariance between two scalar fluctuations using first m number of modes at the cross-section $x/D = 1.0$.

also observed in the case of U_{rms}. A second radial peak is observed for ϕ_{2_rms} in the OSL region ($y/D \approx \pm 1.5$) and there is also a significant contribution from the first four modes. However, this contribution is lower than that at the ISL peak. Despite the significant contribution from the first few modes ($m \leq 8$) in both ϕ_{1_rms} and ϕ_{2_rms}, the high-order modes (which correspond to the high-order structures) are required to completely recover the profile obtained from the total data. As stated earlier in §4.6.2 and §5.3.2, a negative $\langle \phi_1' \phi_2' \rangle$ is observed at the cross-section $x/D = 1.0$ owing to insufficiency of the ambient fluid. In contrast to the RMS velocity fluctuations and the RMS fluctuations of the scalars, the only radial peak of $\langle \phi_1' \phi_2' \rangle$ (present in the ISL $y/D \approx \pm 0.7$) has a smaller contribution from the first four modes, and thus high-order modes are required to recover $\langle \phi_1' \phi_2' \rangle$ obtained from the total data.

Figure 5.15 presents the radial profiles of the radial turbulent fluxes of the IJ scalar ($\langle v' \phi_1' \rangle$) and OJ scalar ($\langle v' \phi_2' \rangle$) reconstructed using selected modes and compares them with the respective quantities determined using the original instantaneous data. Note that the radial flux here refers to the flux in the lateral (i.e., y) direction. An outward radial flux of the IJ scalar is observed in the ISL

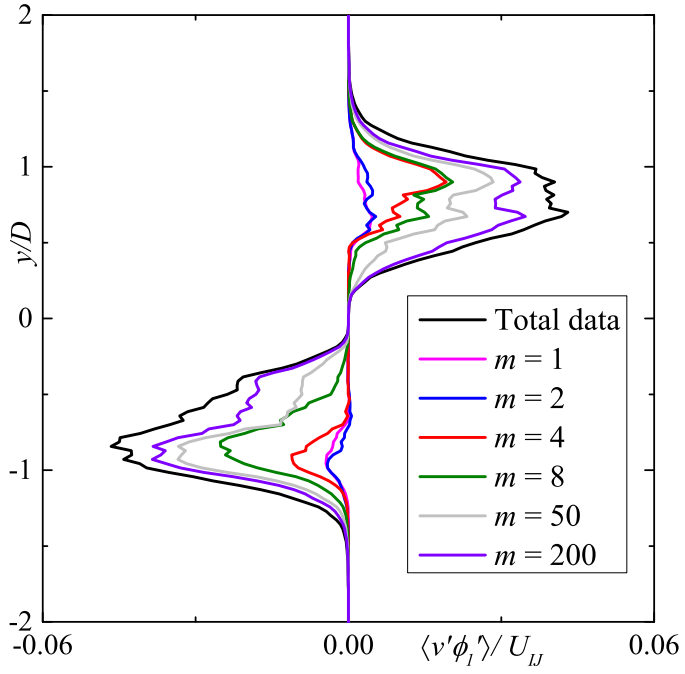

(a)

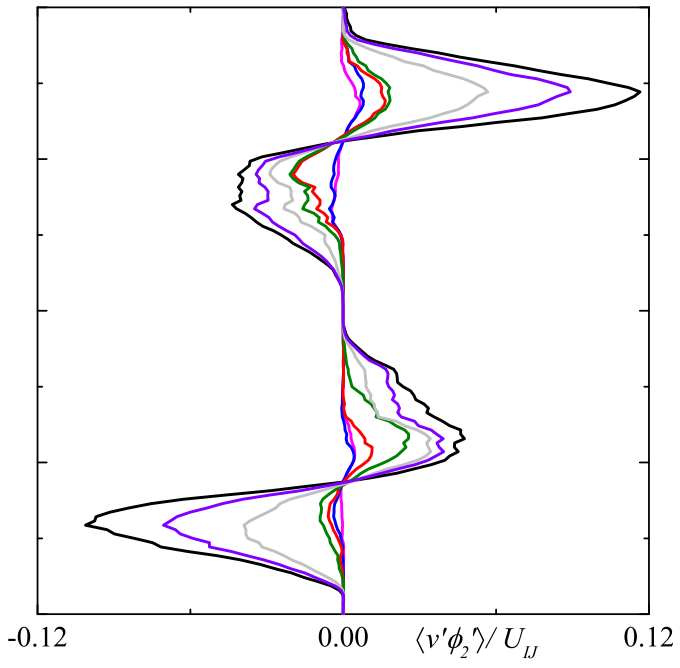

(b)

FIGURE 5.15: Reconstruction of radial turbulent flux of scalars using first 'm' number of modes at the cross-section $x/D = 1.0$. (a) Radial turbulent flux of IJ scalar. (b) Radial turbulent flux of OJ scalar.

$(r/D \leq 1.2)$, whereas an inward radial flux of the OJ scalar is observed in the same region. As mentioned earlier in §5.3.2, the counter-rotating vortical structures exhibit radial outward and inward fluxes of the IJ and OJ scalars, respectively, in

the ISL, and thus the contribution from the first four modes is higher for $\langle v'\phi_1' \rangle$ and $\langle v'\phi_2' \rangle$ in the upper region ($0 < y/D \leq 1.2$). However, this contribution is less in the lower region ($0 > y/D \geq -1.2$) owing to the asymmetry of the spatial modes around the jet axis (see Figures 5.8 and 5.9). Although the first four spatial modes of the OJ scalar exhibit an outward radial flux of the OJ scalar in the OSL ($r/D > 1.2$), its contribution to the total $\langle v'\phi_2' \rangle$ is not large. Therefore, high-order modes play a vital role in the flux $\langle v'\phi_2' \rangle$.

5.5 Conclusions

In this study, the spectral proper orthogonal decomposition (SPOD) was employed to elucidate the physically important structures or modes in the strongly swirling coaxial jet flow (i.e., case Sw18). The analysis was extended to the transport of two separate passive scalars that were simultaneously injected through each jet.

At the cross-stream section present in the region upstream of the central stagnation point ($x/D = 1.0$), the first two (most energetic) spatial modes of the velocity field revealed three pairs of counter-rotating vortical structures, while the two succeeding modes revealed four pairs of such structures. The centers of these vortical structures were found to lie in the ISL present between the two jets. Spatial modes (extended) of scalars also exhibited three and four pairs of alternate positive–negative organized lobe-like structures in this region for the first two and succeeding two modes, respectively. The vortical structures were observed to result in a radial outward flux of the IJ scalar and a radial inward flux of the OJ scalar in the ISL, which is crucial for mixing between the two jets. However, distinct structures appeared in the spatial modes of the OJ scalars in the OSL. These organized structures were subsequently disrupted in the downstream region.

The significance of these pairs of counter-rotating vortical structures was demonstrated by reconstructing various turbulence statistics, namely, the RMS velocities, the RMS scalar fluctuations, the covariance between the two scalars, and the radial turbulent fluxes of the scalars. The results showed that the first four modes make a greater contribution to these statistics except for the covariance between the two scalars, particularly in the ISL. However, this contribution was asymmetric about the axis.

Chapter 6

Conclusions and future prospects

6.1 Conclusions

In this thesis, DNS was used to study the single-phase, unconfined coaxial jet under the influence of swirl introduced in OJ. Two cases with coaxial jet with varying swirling strengths ($Sw = 0.5$ and 1.8) were investigated and compared to a non-swirling case ($Sw = 0$). In order to better the inlet boundary condition, which was crucial in case of swirl jet, the separate simulations were performed for the nozzles, and the data of instantaneous velocity components at the nozzle exit was mapped onto the DNS computational grid. The numerical results were also verified with the experimental measurements and seemed to be satisfactory.

In Chapter 3, the results of momentum transport were presented and the following conclusions were drawn.

- The findings of Ben-Yeoshua (1993) was confirmed in which IRZ was resulted for the case Sw18 and is not observed for the case Sw05.
- The coaxial swirling jet can lead to a contrasting acceleration, as observed in the intermediate swirling case (i.e., case Sw05) at the upstream region due to the negative pressure gradient. However, the downstream region exhibited a centerline decay and radial spread of streamwise velocity.
- As a result of swirl, the Reynolds stresses and TKE were observed to be intensified. Analysis of budgets of TKE and Reynolds normal stresses was carried out for cases Sw0 and Sw18, and following key conclusions were made.

  - Turbulent diffusion term caused TKE level to increase in the central region of OJ of swirling case.
  - TKE in the region outside of IRZ was convected from highly energetic upstream region ($x = 0.3D, 1.0D$) to the downstream region ($x = 3.0D$) in the swirling case. However, the positive contribution by the convection term in non-swirling case seemed to be smaller.
  - The pressure-strain correlation term distinctively acted as an energy sink at $x = 1.0D$ for radial component of Reynolds normal stress at OSL in the swirling case contrary to the non-swirling case.
  - Production of Reynolds normal stresses was enhanced due to the swirl as the terms having streamwise gradient of mean velocity also contributed to the production in addition to the terms with the radial gradient of mean velocity.

In Chapter 4, the separate passive scalars were injected simultaneously through each jet of coaxial jet to study the mixing between two jet fluids. The conclusions based on this study are summarized as follows.

- The intermediate swirling case exhibited a slower decay of the mean IJ scalar and slower inward growth of the mean OJ scalar due to the acceleration in the upstream central region compared to the non-swirling case. However, the downstream region exhibited a wider spread of scalars, which was confirmed by quantifying the diffusion of scalars based on entropy.
- Occurrence of an IRZ in strongly swirling case led to a dramatically improved spreading rate of mean scalars, which was also confirmed based on entropy evolution. This spreading was more prominent in this case than in the other two cases.
- Turbulent azimuthal flux was observed distinctively stronger in the swirling cases compared to the non-swirling case, in which this flux was negligible.
- Positive segregation parameter signifying better mixing characteristics was observed at far upstream in the strongly swirling case as compared to other two cases. Furthermore, the maximum negative magnitude of the segregation parameter, which represents the degree of "unmixedness", was lower in the strongly swirling case compared to the other two cases.

- The JPDF of the scalar fluctuations at the leading centerline stagnation point in the strongly swirling case contained two peaks, which indicates the flapping between IJ and OJ scalars caused by the oscillation of the stagnation point.

In Chapter 5, SPOD analysis and its extension to passive scalars were presented for the strongly swirling case. Following conclusions were made from the findings.

- At the cross-stream section present in upstream region of central stagnation point, first two and succeeding two spatial modes of velocity field revealed three and four pairs of counter-rotating vortical structures, respectively, and these vortical structures were centered at the ISL.
- In the same upstream region of central stagnation point, spatial modes of scalars also exhibited three and four pairs of the alternate positive-negative organized lobe-like structures in ISL for the first two and succeeding two modes, respectively. However, different structures were appeared in the spatial modes of OJ scalars in the OSL.
- The first four modes were appeared to have higher contribution in the RMS velocities, RMS scalar fluctuations and radial turbulent fluxes of scalars. However, this contribution was asymmetric about the axis.

The results of this work can be useful for understanding and designing practical combustors, which often have swirling flows. Based on the observation in the intermediate swirling case that the flow was accelerated in the upstream region, it can be said that the swirling coaxial jet does not always ensure the decay of jet and hence the spread, and this observation needs to be considered while designing the combustors. Another significance of this study is that the budget analysis of TKE and Reynolds normal stresses may provide an useful basis for turbulence modeling work.

6.2 Future prospects

As the coaxial swirling jet is widely used in combustors, it can be of special interest to investigate the reaction occurring between two jet species. This can be

achieved by using the conserved scalar theory (Bilger *et al.* (1991); Watanabe *et al.* (2014)). It investigates the isothermal one-step irreversible reaction, i.e., species A (here it can be IJ species) reacts with species B (here it can be OJ and ambient species) to form product P irreversibly. In the future work, this method can be used to determine the region where the production rate of product P is higher and the transport of product P. The case of strongly swirling case is of special interest as it exhibits IRZ. Furthermore, SPOD analysis can reveal the influence of vortical structures on the species transport.

Acknowledgements

I would like to express my sincere gratitude to my advisor Prof. Yasuhiko Sakai whose continuous support and motivation helped me to succeed in my work. It is his friendly nature which made my academic life smoother. None of this would have been possible without him. I would like to thank my co-advisor Dr. Yasumasa Ito whose valuable guidance and initial thrust during my research really helped me to understand the basics. Without his experience and advice this work could not have been accomplished. I also thank Dr. Koji Iwano whose worthy scientific comments helped me to think deeply.

I also express my heartfelt thanks to Prof. Tomomi Uchiyama and Prof. Koji Nagata for their careful review and valuable comments with regard to this thesis. Those comments were very helpful for revising and improving this thesis, as well as the important guiding significance to my researches.

I would like to acknowledge Mr. Masatoshi Sugino for providing the experimental data. I am grateful to Dr. Kotaro Takamure, Dr. Mamoru Takahashi and all other members of Statistical Fluid Engineering Laboratory for their fruitful scientific discussions as well as social support throughout my study.

I would like to acknowledge the fellowship assistance provided by Japan International Cooperation Agency (JICA). I would like to thank JICA India staffs Ms. Miki Matsuo and Mr. R.S. Sreekanth for their initial support during the admission process. I would also like to thank JICA Chubu staff, especially Ms. Chihiro Takenaga, Ms. Ryoko Tomioka and Mr. Hideki Ito, for their permanent availability to assist me on various occasions.

The good wishes and blessings from my parents, my brother, my wife and my relatives have always been a support. I owe a great deal of appreciation to them. Finally, I would like to thank all my friends who helped me on many occasions.

Appendices

Appendix A

Effects of ambient fluid on the statistics of scalars

The entrained ambient fluid plays a crucial role in the development of the statistics of scalars injected through both jets. The first effect is deviation between the σ_1 and σ_2 profiles and the second effect is the determination of the sign of $\overline{\phi_1'\phi_2'}$. These effects are mathematically explored in this appendix.

We begin with the law of the conservation of mass for the instantaneous and mean flows (which is valid at any given location in the domain) as follows:

$$\phi_1 + \phi_2 + \phi_A = 1, \tag{A.1a}$$

$$\overline{\phi_1} + \overline{\phi_2} + \overline{\phi_A} = 1. \tag{A.1b}$$

These equations will be used frequently in the following formulations. The correlation term $\overline{\phi_1'\phi_2'}$ can be calculated by expanding and rearranging the equations above as

$$\overline{\phi_1'\phi_2'} = \overline{\phi_1\phi_2} - \overline{\phi_1}\ \overline{\phi_2}, \tag{A.2a}$$

$$= \overline{(1-\phi_2-\phi_A)\phi_2} - (1-\overline{\phi_2}-\overline{\phi_A})\ \overline{\phi_2}, \tag{A.2b}$$

$$= -\left(\overline{{\phi_2}^2} - \overline{\phi_2}^2\right) - \overline{\phi_2\phi_A} + \overline{\phi_2}\ \overline{\phi_A}, \tag{A.2c}$$

$$= -{\sigma_2}^2 - \overline{\phi_2\phi_A} + \overline{\phi_2}\ \overline{\phi_A}. \tag{A.2d}$$

If there is no ambient fluid (i.e., $\phi_A = 0$ and $\overline{\phi_A} = 0$), then the correlation $\overline{\phi_1'\phi_2'}$ will be equal to $-{\sigma_2}^2$, which is always negative. This also suggests that positive correlation $\overline{\phi_1'\phi_2'}$ can only be achieved with ${\sigma_2}^2 + \overline{\phi_2\phi_A} < \overline{\phi_2}\ \overline{\phi_A}$, which proves the

second effect of ambient fluid. For the sake of completeness, the counter-equation to Equation A.2d can be derived as follows:

$$\overline{\phi_1'\phi_2'} = -{\sigma_1}^2 - \overline{\phi_1\phi_A} + \overline{\phi_1}\ \overline{\phi_A}. \tag{A.3}$$

From Equations A.2d and A.3, we obtain,

$$\begin{aligned} {\sigma_1}^2 &= {\sigma_2}^2 + \overline{\phi_2\phi_A} - \overline{\phi_2}\ \overline{\phi_A} - \overline{\phi_1\phi_A} + \overline{\phi_1}\ \overline{\phi_A}, && \text{(A.4a)} \\ &= {\sigma_2}^2 + \overline{\phi_2'\phi_A'} - \overline{\phi_1'\phi_A'}. && \text{(A.4b)} \end{aligned}$$

This indicates that $\sigma_1 = \sigma_2$ is ensured by the absence of ambient fluid. However, the occurrence of $\overline{\phi_2'\phi_A'} = \overline{\phi_1'\phi_A'}$ also results in equality of the RMS fluctuations of scalars.

Appendix B

Criterion for the occurrence of vortex breakdown

As discussed in Chapter 1, the researchers (Ben-Yeoshua (1993); Champagne & Kromat (2000); Santhosh *et al.* (2013)) have used the swirl number and experimentally or numerically investigated its threshold value for the occurrence of VB in the swirling jets. However, a criterion based on the theoretical considerations has been proposed by Billant *et al.* (1998) and is explained in this appendix.

Consider a strongly swirling jet injected in an open environment resulting in a conical VB (see Figure B.1). At an streamwise distance x_1, a stagnation point is shown on the axis along with the conical stagnation zone in the downstream region which demonstrates a typical conical VB. Here, the streamwise, azimuthal, and radial velocities are represented by V_x, V_θ, and V_r. The static pressure is represented by P with P_0 being static pressure at a location x_0 far upstream of stagnation point, P_1 being the static pressure at the stagnation point on the axis (i.e., at location x_1), and P_∞ being the ambient pressure. Applying Bernoulli's principal (which states that the total head in the flow should be constant) along the axis, we get

$$\frac{P_0}{\rho} + \frac{V_x^2(0, x_0)}{2} = \frac{P_1}{\rho}. \tag{B.1}$$

where, $V_x(0, x_0)$ is the streamwise velocity on the axis (i.e., at $r = 0$) at x_0. The approximation of equation for mean radial momentum gives,

$$\frac{\partial P}{\partial r} = \frac{\rho V_\theta^2}{r}. \tag{B.2}$$

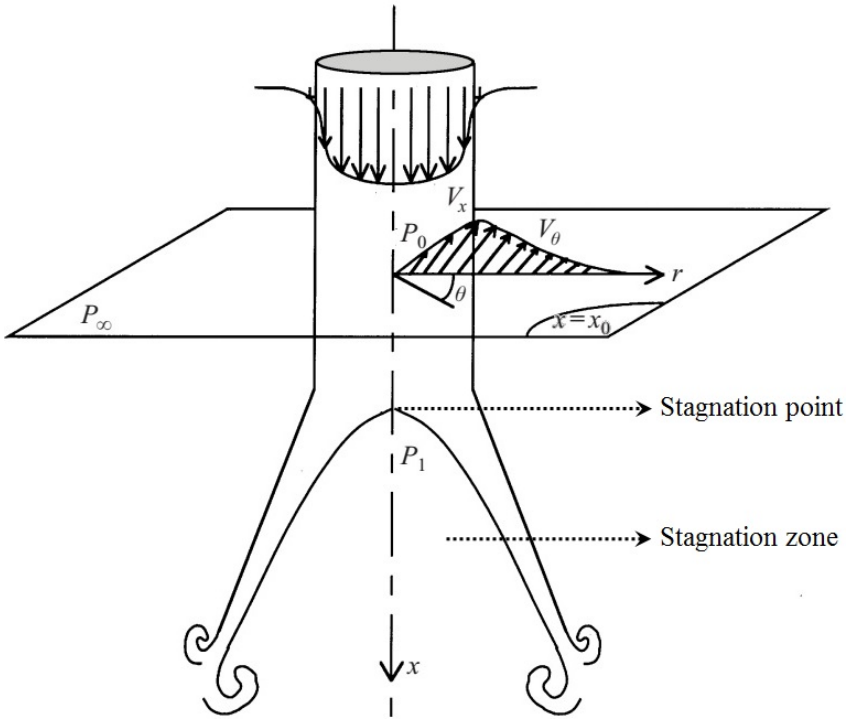

FIGURE B.1: Schematic of conical VB. Adapted from Billant *et al.* (1998).

Integrating with respect to r,

$$P_0 = P_\infty - \int_0^\infty \frac{\rho V_\theta^2(r, x_0)}{r}\, dr. \tag{B.3}$$

Substituting in Equation B.1 and rearranging,

$$P_\infty - \int_0^\infty \frac{\rho V_\theta^2(r, x_0)}{r}\, dr + \frac{\rho V_x^2(0, x_0)}{2} = P_1. \tag{B.4}$$

It is assumed that the velocity inside the stagnation zone is negligibly small (also observed by Escudier & Keller (1983); Escudier (1988)). Moreover, the ambient fluid is stationary and the stagnation zone is open to the ambient fluid. This indicates that the pressure in the stagnation zone is equal to the ambient pressure and thus, $P_1 = P_\infty$. After substituting this identity in Equation B.4 and rearranging, we get,

$$\frac{\displaystyle\int_0^\infty \frac{V_\theta^2(r, x_0)}{r}\, dr}{V_x^2(0, x_0)} = \frac{1}{2}. \tag{B.5}$$

This forms the necessary condition for the occurrence of VB. Billant *et al.* (1998) have demonstrated the usefulness of this criterion with the help of experimental investigations. However, the above criterion may not hold true for the bubble

type VB or VBB as the stationary ambient fluid and the stagnation zone are not directly connected, and the pressure deficit is generated in VBB as a result of Equation B.3. Thus, the identity $P_1 = P_\infty$ does not hold true and needs to be replaced by $P_1 < P_\infty$ (also observed in Figure 3.5(c) and by Ben-Yeoshua (1993); Champagne & Kromat (2000)). This modifies the above criterion as follows,

$$\frac{\int_0^\infty \frac{V_\theta^2(r, x_0)}{r}\, dr}{V_x^2(0, x_0)} > \frac{1}{2}. \tag{B.6}$$

This forms a weak criterion necessary for the occurrence of VB. Moreover, the turbulence and the configuration of coaxial swirling jet complicate the above criterion. In the present thesis, the left-hand side of above criterion is equal to 0.74 and 2.67 for the cases Sw05 and Sw18, respectively. This demonstrates the weaker nature of above criterion and the obstacle in proposing a criterion based on theoretical consideration. Hence the researchers widely use swirl number and rely on experimentally or numerically investigated threshold value of swirl number for the occurrence of VB.

Appendix C

Types of vortex breakdown

In past researches, several types of VB have been observed in the swirling flows and are summarized in this appendix.

(a) Bubble:

Sarpkaya (1971*a*) imparted a single swirling jet in a slightly diverging tube and the structure of VB was visualized by injecting the dye into the flow field. For a set of Reynolds number and swirling strength, an axisymmetric bubble was appeared at the central region with a downstream tail (see Figure C.1). The bubble was characterized by low velocity recirculating fluid. The bubble type of VB or VBB is commonly found by many researchers in both the single swirling jet (Faler & Leibovich (1977); Billant *et al.* (1998); Moise & Mathew (2019)) as well as the coaxial swirling jet (Dinesh & Kirkpatrick (2009); Santhosh *et al.* (2013)). Note that Santhosh *et al.* (2013) reported two separate types of VBB (see Figure 1.3): VBB penetrated by central jet (also found in the present study, see Figure 3.4(c)) and CTRZ in which the penetrated part was absent.

(b) Spiral:

Prior to VBB with a slow increment in the swirling strength, Sarpkaya (1971*a*) observed that the dyed filament decelerated and subsequently spiraled in the downstream region after an abrupt kink (see Figure C.2). Spiral VB was also observed to be evolved into the VBB. Faler & Leibovich (1977) also reported the similar type of VB. As per our knowledge, such type of VB is not found in the coaxial swirling jet as no past research results could be found for the same.

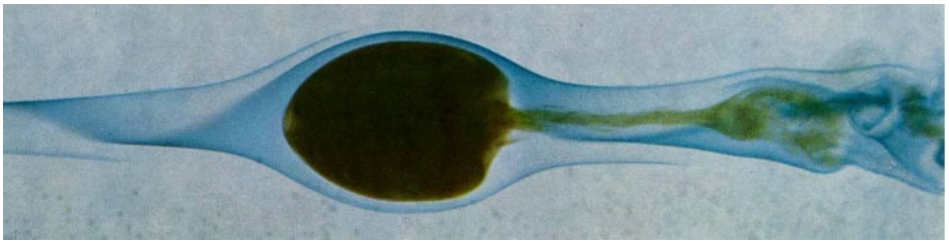

FIGURE C.1: Bubble type of VB. Adapted from Sarpkaya (1971*a*).

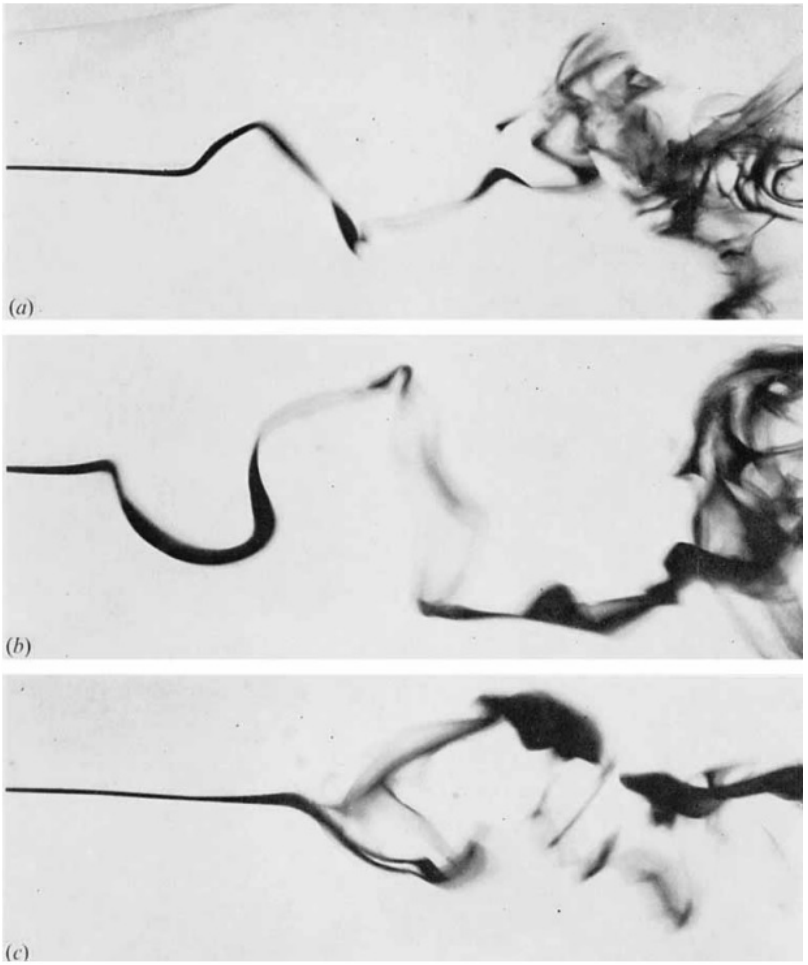

FIGURE C.2: Evolution of spiral type of VB presented by Sarpkaya (1971*a*) based on the increment in the angle of swirl generating vanes.

(c) Double helix:

With a very slow increment in the swirling strength, Sarpkaya (1971*a*) exhibited that the spiral VB evolved into a double helix type of VB (see Figure C.3) before ultimately evolving into the VBB. Double helix VB was characterized by the expansion of dyed filament into a slightly curved triangular sheet. Each half of the sheet wrapped around the other half to form a double helix. This type of

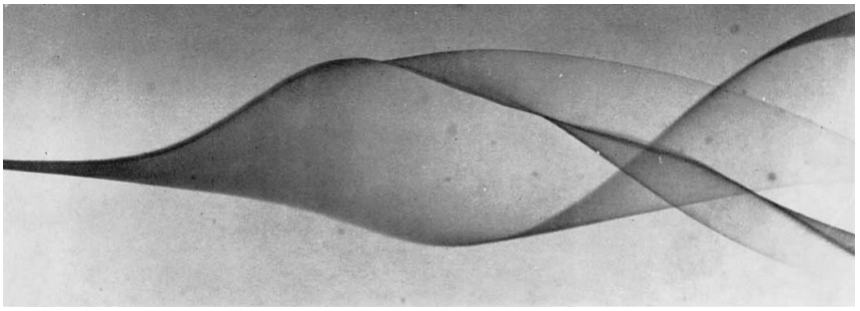

FIGURE C.3: Double helix type of VB. Adapted from Sarpkaya (1971*a*).

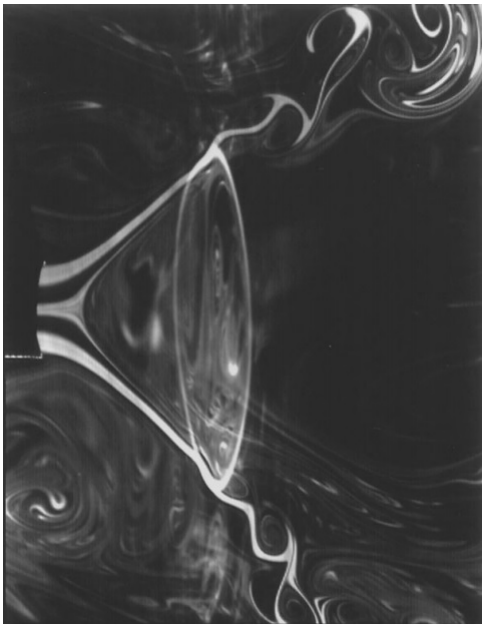

FIGURE C.4: Conical type of VB. Adapted from Billant *et al.* (1998).

VB was also reported by Faler & Leibovich (1977). Similar to spiral VB, double helix VB is not found in the coaxial swirling jet.

(d) Conical:

Billant *et al.* (1998) reported the conical type of VB for their experimental study of a single swirling jet (see Figure C.4). It exhibited the expansion of the vortex at the stagnation point which was followed by the diversion of conical sheet. This sheet was not reattached in the downstream region. The similar structure of VB was also observed by Moise & Mathew (2019) for a single swirling jet whereas Santhosh *et al.* (2014) observed it for their study of the coaxial swirling jet.

Sarpkaya (1971*a*,*b*) has also presented the conditions for the occurrence of first three types of VB (i.e., bubble, spiral, and double helix) based on the numerous experimental measurements for the single swirling jet configuration. It was reported that for the Reynolds number Re just greater than 2000, the spiral VB occurred for even a low circulation number Ω ($\Omega = \Gamma/UD$, where U and D are mean velocity and diameter of jet at the nozzle exit, and Γ circulation imparted to flow $= 2\pi R_i V_i \sin\beta$. R_i and β are the radial distance to the tip of a vane and the vane angle, respectively, and V_i is the mean velocity of flow between two vanes. $V_i \sin\beta$ is the mean azimuthal velocity at the tip of vane. Refer Figure 2 in Sarpkaya (1971*a*) for the vane configuration. Note that Ω can be said to be directly proportional to Sw.). However, with the increase in Ω, the occurrence of spiral VB was also noticed for smaller Re. Spiral VB was observed to lead to two types of VB with the increment in Ω, i.e., either into double helix VB or into VBB. However, the double helix occurred only for $Re < 2000$ and $\Omega > 2.3$, and the double helix VB ultimately transformed to VBB for $\Omega > 2.5$. For $Re > 2000$ and $\Omega > 2.3$, the spiral VB directly transformed into VBB.

In the configuration of coaxial swirling jet, Santhosh *et al.* (2014) observed VBB for $Ro_m = 1.12$ and $S = 0.75$ (here, $Ro_m = |\Delta U|/V_{\theta,avg}$ and $S = (\int_0^{R_o} \rho\overline{U}\,\overline{V_\theta}\, r^2\, dr)/(R_o \int_0^{R_o} \rho\overline{U}^2\, r\, dr)$). However, for the slight increase in S with approximately constant Ro_m resulted in conical VB before returning to VBB at $S \approx 0.92$. This was observed for all $Ro_m \leq 1.12$, however, the minimum S required for the occurrence of VBB increases slightly with the decrease in Ro_m (refer Figure 4 in Santhosh *et al.* (2014)).

In summary, although the above various types of VB have been reported, a universal criterion or parameter governing the type of VB has not been introduced clearly. Thus, this forms a scope for future researchers to investigate the parameters governing the different types of VB.

Bibliography

Abboud, A. W. & Smith, S. T. 2014 Large eddy simulation of a coaxial jet with a synthetic turbulent inlet. *Int. J. Heat Fluid Flow* **50**, 240–253.

Antoranz, A., Ianiro, A., Flores, O. & García-Villalba, M. 2018 Extended proper orthogonal decomposition of non-homogeneous thermal fields in a turbulent pipe flow. *Int. J. Heat Mass Transf.* **118**, 1264–1275.

Ben-Yeoshua, M. 1993 Coaxial jets with swirl. M.S. Thesis, The University of Arizona.

Bilger, R. W., Saetran, L. R. & Krishnamoorthy, L. V. 1991 Reaction in a scalar mixing layer. *J. Fluid Mech.* **233**, 211–242.

Billant, P., Chomaz, J. M. & Huerre, P. 1998 Experimental study of vortex breakdown in swirling jets. *J. Fluid Mech.* **376**, 183–219.

Borée, J. 2003 Extended proper orthogonal decomposition: a tool to analyse correlated events in turbulent flows. *Exp. Fluids* **35** (2), 188–192.

Buresti, G., Petagna, P. & Talamelli, A. 1998 Experimental investigation on the turbulent near-field of coaxial jets. *Exp. Therm. Fluid Sci.* **17** (1-2), 18–26.

Cai, J., Dinger, M. J., Li, W., Carter, C. D., Ryan, M. D. & Tong, C. 2011 Experimental study of three-scalar mixing in a turbulent coaxial jet. *J. Fluid Mech.* **685**, 495–531.

Cassidy, J. J. & Falvey, H. T. 1970 Observations of unsteady flow arising after vortex breakdown. *J. Fluid Mech.* **41** (4), 727–736.

Champagne, F. H. & Kromat, S. 2000 Experiments on the formation of a recirculation zone in swirling coaxial jets. *Exp. Fluids* **29** (5), 494–504.

Champagne, F. H. & Wygnanski, I. J. 1971 An experimental investigation of coaxial turbulent jets. *Int. J. Heat Mass Transf.* **14** (9), 1445–1464.

Clees, S., Lewalle, J., Frederick, M. & O'Connor, J. 2018 Vortex core dynamics in a swirling jet near vortex breakdown. In *2018 AIAA Aerospace Sciences Meeting*.

Dai, Y., Kobayashi, T. & Taniguchi, N. 1994 Large eddy simulation of plane turbulent jet flow using a new outflow velocity boundary condition. *JSME Int. J. B-Fluid. T.* **37** (2), 242–253.

Danckwerts, P. V. 1952 The definition and measurement of some characteristics of mixtures. *Appl. Sci. Res.* **3** (4), 279–296.

Dembinski, H. W. R. & Angstrom, H.-E. 2012 Optical study of swirl during combustion in a ci engine with different injection pressures and swirl ratios compared with calculations. *Tech. Rep.* 2012-01-0682. SAE Technical Paper.

Dinesh, K. R. & Kirkpatrick, M. P. 2009 Study of jet precession, recirculation and vortex breakdown in turbulent swirling jets using les. *Comput. Fluids* **38** (6), 1232–1242.

Dinesh, K. R., Kirkpatrick, M. P. & Jenkins, K. W. 2010 Investigation of the influence of swirl on a confined coannular swirl jet. *Comput. Fluids* **39** (5), 756–767.

Eiamsa-ard, P., Piriyarungroj, N., Thianpong, C. & Eiamsa-ard, S. 2014 A case study on thermal performance assessment of a heat exchanger tube equipped with regularly-spaced twisted tapes as swirl generators. *Case Stud. Therm. Eng.* **3**, 86–102.

Escudier, M. 1988 Vortex breakdown: observations and explanations. *Prog. Aerosp. Sci.* **25** (2), 189–229.

Escudier, M. P. & Keller, J. J. 1983 Vortex breakdown: a two-stage transition. *Tech. Rep.* AGARD CP-342.

Everson, R., Manin, D., Sirovich, L. & Winter, M. 1998 Quantification of mixing and mixing rate from experimental observations. *AIAA J.* **36** (2), 121–127.

Faler, J. H. & Leibovich, S. 1977 Disrupted states of vortex flow and vortex breakdown. *Phys. Fluids* **20** (9), 1385–1400.

Gallaire, F., Rott, S. & Chomaz, J. M. 2004 Experimental study of a free and forced swirling jet. *Phys. Fluids* **16** (8), 2907–2917.

Greenshields, C. J. 2015 OpenFOAM user guide. *OpenFOAM Foundation Ltd* **2** (4).

Harvey, J. K. 1962 Some observations of the vortex breakdown phenomenon. *J. Fluid Mech.* **14** (4), 585–592.

Huang, R. F. & Tsai, F. C. 2001 Flow field characteristics of swirling double concentric jets. *Exp. Therm. Fluid Sci.* **25** (3-4), 151–161.

Ito, Y., Miura, K., Sakai, Y. & Iwano, K. 2018 Enhancement and suppression of mixing and diffusion in an axisymmetric jet by half delta-wing tabs. *Int. J. Heat Mass Transf.* **118**, 1218–1230.

Kadu, P. A., Sakai, Y., Ito, Y., Iwano, K., Sugino, M., Katagiri, T., Hayase, T. & Nagata, K. 2019*a* Budgets of turbulent kinetic energy and reynolds normal stresses in coaxial jets with and without swirl: a numerical study. *Journal of Energy and Environmental Sustainability (in press)* .

Kadu, P. A., Sakai, Y., Ito, Y., Iwano, K., Sugino, M., Katagiri, T. & Nagata, K. 2019*b* Numerical investigation of passive scalar transport and mixing in a turbulent unconfined coaxial swirling jet. *Int. J. Heat Mass Transf.* **142**, 118461.

Kim, J. & Moin, P. 1985 Application of a fractional-step method to incompressible Navier-Stokes equations. *J. Comput. Phys.* **59** (2), 308–323.

Komori, S., Hunt, J. C. R., Kanzaki, T. & Murakami, Y. 1991 The effects of turbulent mixing on the correlation between two species and on concentration fluctuations in non-premixed reacting flows. *J. Fluid Mech.* **228**, 629–659.

Komori, S. & Ueda, H. 1985 Turbulent flow structure in the near field of a swirling round free jet. *Phys. Fluids* **28** (7), 2075–2082.

Kurtbaş, İ., Durmuş, A., Eren, H. & Turgut, E. 2007 Effect of propeller type swirl generators on the entropy generation and efficiency of heat exchangers. *Int. J. Therm. Sci.* **46** (3), 300–307.

Leschziner, M. A. & Rodi, W. 1984 Computation of strongly swirling axisymmetric free jets. *AIAA J.* **22** (12), 1742–1747.

Li, W., Yuan, M., Carter, C. D. & Tong, C. 2017 Experimental investigation of the effects of mean shear and scalar initial length scale on three-scalar mixing in turbulent coaxial jets. *J. Fluid Mech.* **817**, 183–216.

Lu, X., Wang, S., Sung, H. G., Hsieh, S. Y. & Yang, V. 2005 Large-eddy simulations of turbulent swirling flows injected into a dump chamber. *J. Fluid Mech.* **527**, 171–195.

Lucca-Negro, O. & O'doherty, T. 2001 Vortex breakdown: a review. *Prog. Energ. Combust.* **27** (4), 431–481.

Lumley, J. L. 1967 The structure of inhomogeneous turbulent flows. *Atmospheric Turbulence and Radio Wave Propagation* .

Markovich, D. M., Abdurakipov, S. S., Chikishev, L. M., Dulin, V. M. & Hanjalić, K. 2014 Comparative analysis of low-and high-swirl confined flames and jets by proper orthogonal and dynamic mode decompositions. *Phys. Fluids* **26** (6), 065109.

Mehta, R. D., Wood, D. H. & Clausen, P. D. 1991 Some effects of swirl on turbulent mixing layer development. *Phys. Fluid A-Fluid* **3** (11), 2716–2724.

Moise, P. & Mathew, J. 2019 Bubble and conical forms of vortex breakdown in swirling jets. *J. Fluid Mech.* **873**, 322–357.

Morinishi, Y., Lund, T. S., Vasilyev, O. V. & Moin, P. 1998 Fully conservative higher order finite difference schemes for incompressible flow. *J. Comput. Phys.* **143** (1), 90–124.

Moser, R. D. & Moin, P. 1984 Direct numerical simulation of curved turbulent channel flow. *Tech. Rep.* TM-85974. NASA.

Narain, J. P. 1977 Numerical prediction of confined swirling jets. *Comput. Fluids* **5** (3), 115–125.

Nocedal, J. & Wright, S. J. 2006 Conjugate gradient methods. *Numerical Optimization* pp. 101–134.

Oberleithner, K., Sieber, M., Nayeri, C. N., Paschereit, C. O., Petz, C., Hege, H. C., Noack, B. R. & Wygnanski, I. 2011 Three-dimensional coherent structures in a swirling jet undergoing vortex breakdown: stability analysis and empirical mode construction. *J. Fluid Mech.* **679**, 383–414.

Örlü, R. & Alfredsson, P. H. 2008 An experimental study of the near-field mixing characteristics of a swirling jet. *Flow, Turbul. Combust.* **80** (3), 323–350.

Park, S. H. & Shin, H. D. 1993 Measurements of entrainment characteristics of swirling jets. *Int. J. Heat Mass Transf.* **36** (16), 4009–4018.

Rajamanickam, K. & Basu, S. 2018 Insights into the dynamics of conical breakdown modes in coaxial swirling flow field. *J. Fluid Mech.* **853**, 72–110.

Rajaratnam, N. 1976 *Turbulent jets*, , vol. 5, pp. 130–133. Elsevier.

Rehab, H., Villermaux, E. & Hopfinger, E. J. 1997 Flow regimes of large-velocity-ratio coaxial jets. *J. Fluid Mech.* **345**, 357–381.

Ribeiro, M. M. & Whitelaw, J. H. 1980 Coaxial jets with and without swirl. *J. Fluid Mech.* **96** (4), 769–795.

Roback, R. & Johnson, B. V. 1983 Mass and momentum turbulent transport experiments with confined swirling coaxial jets. *Tech. Rep.* CR-168252. NASA.

Santhosh, R., Miglani, A. & Basu, S. 2013 Transition and acoustic response of recirculation structures in an unconfined co-axial isothermal swirling flow. *Phys. Fluids* **25** (8), 083603.

Santhosh, R., Miglani, A. & Basu, S. 2014 Transition in vortex breakdown modes in a coaxial isothermal unconfined swirling jet. *Phys. Fluids* **26** (4), 043601.

Sarpkaya, T. 1971*a* On stationary and travelling vortex breakdowns. *J. Fluid Mech.* **45** (3), 545–559.

Sarpkaya, T. 1971*b* Vortex breakdown in swirling conical flows. *AIAA J.* **9** (9), 1792–1799.

Schmid, PJ 2010 Dynamic mode decomposition of numerical and experimental data. *J. Fluid Mech.* **656**, 5–28.

Shiri, A. 2010 Turbulence measurements in a natural convection boundary layer and a swirling jet. Ph.D. Dissertation, Chalmers University of Technology.

Sieber, M., Paschereit, C. O. & Oberleithner, K. 2016 Spectral proper orthogonal decomposition. *J. Fluid Mech.* **792**, 798–828.

Sieber, M., Paschereit, C. O. & Oberleithner, K. 2017 Advanced identification of coherent structures in swirl-stabilized combustors. *J. Eng. Gas Turb. Power* **139** (2), 021503.

Sirovich, L. 1987 Turbulence and the dynamics of coherent structures, Part I: Coherent structures. *Q. Appl. Math.* **45** (3), 561–571.

Stöhr, M., Sadanandan, R. & Meier, W. 2011 Phase-resolved characterization of vortex–flame interaction in a turbulent swirl flame. *Exp. Fluids* **51** (4), 1153–1167.

Stopper, U., Aigner, M., Ax, H., Meier, W., Sadanandan, R., Stöhr, M. & Bonaldo, A. 2010 PIV, 2D-LIF and 1D-Raman measurements of flow field, composition and temperature in premixed gas turbine flames. *Exp. Therm. Fluid Sci.* **34** (3), 396–403.

Tabor, G. R. & Baba-Ahmadi, M. H. 2010 Inlet conditions for large eddy simulation: a review. *Comput. Fluids* **39** (4), 553–567.

Tong, C. & Warhaft, Z. 1995 Passive scalar dispersion and mixing in a turbulent jet. *J. Fluid Mech.* **292**, 1–38.

Tsujimoto, K., Ao, K., Shakouchi, T. & Ando, T. 2011 Numerical investigation on flow structures and mixing performances of vector-controlled free jet using DNS. *J. Fluid Sci. Tech.* **6** (4), 401–411.

Wan, Z.-H., Zhou, L., Wang, B.-F. & Sun, D.-J. 2015 Dynamic mode decomposition of forced spatially developed transitional jets. *Eur. J. Mech. B-Fluid* **51**, 16–26.

Watanabe, T., Sakai, Y., Nagata, K., Ito, Y. & Hayase, T. 2014 Reactive scalar field near the turbulent/non-turbulent interface in a planar jet with a second-order chemical reaction. *Phys. Fluids* **26** (10), 105111.

Wei, S., Wang, F., Leng, X., Liu, X. & Ji, K. 2013 Numerical analysis on the effect of swirl ratios on swirl chamber combustion system of DI diesel engines. *Energ. Convers. Manage.* **75**, 184–190.

Xia, J. L., Smith, B. L., Benim, A. C., Schmidli, J. & Yadigaroglu, G. 1997 Effect of inlet and outlet boundary conditions on swirling flows. *Comput. Fluids* **26** (8), 811–823.